Delft University of Technology

Document Version
Final published version

Citation (APA)
Shangguan, H. (2026). *High-Resolution Large-Depth-Range Digital holography for 3D Optical Metrology*. [Dissertation (TU Delft), Delft University of Technology]. https://doi.org/10.4233/uuid:004db856-c497-4618-b083-5a728d09a906

Important note
To cite this publication, please use the final published version (if applicable).
Please check the document version above.

Copyright
In case the licence states "Dutch Copyright Act (Article 25fa)", this publication was made available Green Open Access via the TU Delft Institutional Repository pursuant to Dutch Copyright Act (Article 25fa, the Taverne amendment). This provision does not affect copyright ownership.
Unless copyright is transferred by contract or statute, it remains with the copyright holder.

Sharing and reuse
Other than for strictly personal use, it is not permitted to download, forward or distribute the text or part of it, without the consent of the author(s) and/or copyright holder(s), unless the work is under an open content license such as Creative Commons.

Takedown policy
Please contact us and provide details if you believe this document breaches copyrights.
We will remove access to the work immediately and investigate your claim.

This work is downloaded from Delft University of Technology.

High-Resolution Large-Depth-Range Digital holography for 3D Optical Metrology

Huangcheng Shangguan

Propositions

accompanying the dissertation

High-Resolution Large-Depth-Range Digital holography for 3D Optical Metrology

by

Huangcheng SHANGGUAN

1. A good calibration target is essential to both safeguard phase accuracy and implement accurate data processing in digital holography. (This thesis)
2. In digital holography, diversifying wavelength sampling gives better height precision than increasing repetitions of the same wavelength set. (This thesis)
3. Multi-wavelength digital holography in industrial applications is hindered more by the wavelength reproducibility than by the wavelength tuning range. (This thesis)
4. In contrast to conventional imaging, digital holography decouples lateral resolution from depth range. (This thesis)
5. Progress in a PhD stalls when one aims for perfect experiments; it advances by accepting that the system is not perfect and working with the data available.
6. A decision made without some unease suggests that the issue has not been explored thoroughly enough.
7. In an age of information overload, delayed response distinguishes the signal from the noise.
8. Whereof one cannot yet speak with understanding, thereof one should be silent until after proper inquiry and practicing. (Inspired by Tractatus Logico-Philosophicus by Ludwig Wittgenstein)
9. Love life more than the meaning of life. Love individuals more than humanity as a whole. (After The Brothers Karamazov by Fyodor Dostoevsky)
10. Dutch weather owes its poor reputation not to abundant rainfall, but to vivid memories of rainy commutes.

These propositions are regarded as opposable and defendable, and have been approved as such by the promotors dr. J. Kalkman and Em. prof. dr. H. P. Urbach.

High-Resolution Large-Depth-Range Digital holography for 3D Optical Metrology

High-Resolution Large-Depth-Range Digital holography for 3D Optical Metrology

Dissertation

for the purpose of obtaining the degree of doctor
at Delft University of Technology
by the authority of the Rector Magnificus, Prof. dr. ir. H. Bijl,
chair of the Board for Doctorates
to be defended publicly on
Thursday, 09 July 2026 at 17:30

by

Huangcheng SHANGGUAN

This dissertation has been approved by the promotors.

Composition of the doctoral committee:

Rector Magnificus,	chairperson
Em. prof. dr. H. P. Urbach,	Delft University of Technology, *promotor*
Dr. J. Kalkman,	Delft University of Technology, *promotor*
Independent members:	
Prof. dr. J. F. de Boer	Vrije Universiteit Amsterdam
Dr. T. Cromwijk	ARCNL/ASML Holding N.V.
Prof. dr. M. Trusiak,	Warsaw University of Technology
Prof. dr. S. M. Witte,	Delft University of Technology
Prof. dr. S. Stallinga,	Delft University of Technology, reserve member

Keywords: Digital holography; 3D optical metrology; Multi-wavelength interferometry; Quantitative phase imaging; Semiconductor metrology

Printed by: Ridderprint

Cover by: Huangcheng Shangguan & ChatGPT

Copyright © 2026 by H. Shangguan

ISBN 978-94-6518-376-3

An electronic copy of this dissertation is available at
https://repository.tudelft.nl/.

CONTENTS

Summary vii

Samenvatting ix

1 Introduction 1
- 1.1 Inspection and Metrology in Semiconductor Manufacturing 2
- 1.2 3D optical imaging techniques for industrial inspection 4
- 1.3 Digital holography for high-speed full-field optical metrology 6
  - 1.3.1 Basic principles of digital holography 7
  - 1.3.2 Fourier domain description of off-axis digital holography . . . 10
  - 1.3.3 Key features and parameters of digital holography for metrology 12
- 1.4 Challenges for industrial metrology with DH 15
  - 1.4.1 Limited measurement depth range 16
  - 1.4.2 Resolution limitations due to pixel size and spectral overlap . 17
  - 1.4.3 Difficulty in imaging multi-interface structures 19
- 1.5 Outline of this dissertation 19
- References 21

2 Lensless single-shot DWDH for industrial metrology 27
- 2.1 Introduction 28
- 2.2 Methods 29
  - 2.2.1 Lensless digital holography setup 29
  - 2.2.2 Object field reconstruction 31
  - 2.2.3 Theoretical accuracy of DWDH phase estimation 33
- 2.3 Results 34
  - 2.3.1 Lateral resolution and field of view 34
  - 2.3.2 Phase accuracy 36
  - 2.3.3 Application to industrial inspection 36
- 2.4 Discussion 41
- 2.5 Conclusion 42
- References 43

3 Sub-pixel resolution and cm-depth-range Lensless DWDH 47
- 3.1 Introduction 48
- 3.2 Methods 49
  - 3.2.1 Expanding wave illumination dual-wavelength digital holography setup 49
  - 3.2.2 PWI- and EWI- DWDH resolution 51

3.2.3 Quantitative phase reconstruction in EWI-DWDH 52
3.2.4 Laser calibration and tunability 54
3.3 Lateral resolution enhancement results 56
3.4 Large height measurements results 58
3.5 Instantaneous and temporal precision 60
3.6 Discussion 64
3.7 Conclusion 65
3.8 Appendix A: The equivalent propagation distance 66
3.9 Appendix B: Validation of centimeter-scale depth measurement . . . 67
References 69

4 Improving depth range and resolution with MWDH 73
4.1 Introduction 74
4.2 Theory 75
4.2.1 Multi-wavelength digital holography 75
4.2.2 Multi-wavelength DH depth resolution enhancement 77
4.3 Results 79
4.3.1 Experimental setup 79
4.3.2 Beat phase and synthetic wavelength calculation 79
4.3.3 Distance Estimation 82
4.4 Discussion 84
4.5 Conclusion 85
References 87

5 Conclusions and outlook 89
5.1 Conclusions 89
5.2 Towards digital holographic tomography 91
5.2.1 Modeling the field from multilayered objects 91
5.2.2 Holographic imaging of multilayer object 93
5.3 Measuring speckle-dominant objects 95
5.3.1 Speckle decorrelation noise 95
5.3.2 Total phase noise and height precision 96
5.4 Multi-step phase unwrapping depth precision enhancement 98
References 101

Acknowledgements 103

Curriculum Vitæ 105

List of Publications 107

SUMMARY

Digital holography (DH) is a full-field, three-dimensional optical imaging technique for high-speed industrial inspection. By retrieving the complex optical field, DH provides quantitative phase information that enables three-dimensional measurement of surface topography. This thesis is motivated by the demands of advanced semiconductor manufacturing and assembly, where centimeter-scale depth ranges and large field-of-views must be achieved at high throughput. A lensless configuration is used to keep the optical system compact and integration-friendly, while numerical propagation enables refocusing. Within this framework, three key challenges of DH-based metrology are addressed: limited unambiguous depth range due to phase wrapping, pixel-size-limited lateral resolution in lensless DH configurations, and the trade-off between depth range and depth precision.

Industrial samples often exhibit large and abrupt height variations. In single-wavelength DH, the unambiguous depth range of half a wavelength is insufficient to unambiguously determine the height of micrometer to millimeter-scale structures. Chapter 2 describes the development of a dual-wavelength off-axis lensless DH configuration with spatial-frequency multiplexing to enable single-shot acquisition at two discrete wavelengths. By leveraging the beat frequency of the two wavelengths, the system generates a synthetic wavelength, which extends the unambiguous depth range to half the synthetic wavelength. A model for shot-noise-limited phase-precision is derived and experimentally validated. Measurements on calibrated targets and representative industrial samples demonstrate reliable three-dimensional reconstruction over extended depth ranges, confirming the suitability of single-shot dual-wavelength DH for high-speed metrology.

When DH is implemented in a lensless configurations, the lateral resolution is constrained by sensor pixel size, which limits the maximum spatial frequencies and thus restricts the detection of fine features such as micro-defects. To overcome this limitation, Chapter 3 introduces an expanding wavefront illumination scheme that increases the available angular spectrum of the object field while maintaining system compactness. A background aberration compensation algorithm is developed to correct global aberrations using locally sampled regions, thereby retaining single-shot operation. By incorporating a tunable external-cavity diode laser, the system achieves a centimeter-scale depth range in combination with micrometer-scale lateral resolution.

Besides a large depth range, industrial metrology also demands high depth precision over the accessible depth span. In conventional dual-wavelength DH, increasing the synthetic wavelength enlarges the unambiguous range but proportionally amplifies phase noise when converted to height, which leads to degraded precision. Chapter 4 addresses this trade-off by developing a multi-wavelength DH technique

based on discrete wavelength sampling. In multi-wavelength DH, the surface height is retrieved via multi-point phase fitting in the wavenumber domain, thereby combining Fourier-based coarse depth localization with linear regression. The utilized self-calibration strategy, based on pairwise beat-phase analysis, removes the need for auxiliary high-precision wavelength-monitoring instruments. This approach mitigates noise amplification and improves depth precision over a large depth range, broadening the feasibility of DH for large-scale, high-precision industrial inspection.

In summary, this thesis demonstrates that coordinated advances in optical system design and computational reconstruction can alleviate key limitations of DH in industrial metrology. By extending the depth range, enhancing lateral resolution, and improving depth precision, the proposed methods broaden the applicability of DH while maintaining its intrinsic advantages of full-field imaging and quantitative phase retrieval.

SAMENVATTING

Digitale holografie (DH) is een contactloze, driedimensionale optische afbeeldingstechniek voor hogesnelheidsinspectie in industriële toepassingen. DH reconstrueert het complexe optische veld en geeft daarbij kwantitatieve fase-informatie die driedimensionale metingen van oppervlaktetopografie mogelijk maken. Dit proefschrift is ontstaan vanuit de vereisten diegeavanceerde halfgeleiderfabricage en -assemblage stellen aan beeldvormingstechnieken. In dit toepassingsgebied moet een groot meetbereik en gezichtsveld (op centimeterschaal) worden gecombineerd met een hoge doorvoer. Een lensloze configuratie wordt gebruikt om het optische systeem compact en makkelijk integreerbaar te maken terwijl numerieke propagatie focussering van het golfveld mogelijk maakt. Binnen dit kader worden drie cruciale uitdagingen van op DH gebaseerde metrologie aangepakt: het beperkte eenduidige dieptebereik als gevolg van faseomwikkeling, de door pixelgrootte beperkte laterale resolutie in lensloze DH-configuraties, en de afweging tussen dieptebereik en diepteprecisie.

Industriële monsters vertonen vaak grote en abrupte hoogteverschillen. Bij DH gebaseerd op een enkele golflengte is het eenduidige dieptebereik van een halve golflengte ontoereikend om de hoogte van structuren op micrometer- tot millimeterschaal eenduidig te bepalen. Hoofdstuk 2 beschrijft de ontwikkeling van een off-axis lensloze DH-configuratie met twee golflengten waarbij gebruik wordt gemaakt van spatiële frequentiemultiplexing om single-shot acquisitie op twee discrete golflengten mogelijk te maken. Door deze multiplexing wordt de hoge doorvoer, die vereist is voor productielijn inspectie, behouden. Door gebruik te maken van de zwevingsfrequentie van de twee golflengten kan een synthetische golflengte worden gemaakt, waardoor het eenduidige dieptebereik wordt uitgebreid tot de helft van deze synthetische golflengte. Er is een model voor de door hagelruis (shot noise) beperkte faseprecisie afgeleid en experimenteel gevalideerd. Metingen aan gekalibreerde objecten en representatieve industriële monsters demonstreren betrouwbare driedimensionale reconstructies over een groot dieptebereik wat de geschiktheid van single-shot duale-golflengte DH voor hogesnelheidsmetrologie bevestigt.

Wanneer DH wordt geïmplementeerd in lensloze configuraties, wordt de laterale resolutie beperkt door de pixelgrootte van de sensor. Dit beperkt de maximaal meetbare spatiële frequenties en belemmert de detectie van fijne details, zoals bijvoorbeeld microdefecten. Om deze beperking weg te nemen wordt in Hoofdstuk 3 een belichtingsschema geïntroduceerd met een expanderend golffront, dat het beschikbare hoekspectrum van het objectveld vergroot terwijl de compactheid van het systeem behouden blijft. Een algoritme voor de compensatie van achtergrondaberraties is ontwikkeld om globale aberraties te corrigeren met behulp van lokaal bemonsterde gebieden waardoor de single-shot werking behouden blijft. Door integratie van een afstembare external-cavity diodelaser bereikt het systeem een dieptebereik

op centimeterschaal in combinatie met een laterale resolutie op micrometerschaal.

Naast een groot dieptebereik vereist industriële metrologie ook een hoge diepteprecisie over het gehele toegankelijke dieptebereik. Bij conventionele tweegolflengten DH vergroot het verlengen van de synthetische golflengte weliswaar het eenduidige dieptebereik, maar dit versterkt proportioneel de faseruis bij de omzetting naar hoogte, wat leidt tot een verminderde precisie. Hoofdstuk 4 laat een oplossing voor dit probleem zien door een meervoudige-golflengte DH-techniek te ontwikkelen gebaseerd op discrete golflengtebemonstering. Bij meervoudige-golflengte DH wordt de oppervlaktehoogte verkregen via een fit aan de fase van meervoudige metingen in het golfgetal domein, waarbij op Fourier-transformatie gebaseerde grove dieptelokalisatie wordt gecombineerd met lineaire regressie voor fijne dieptelokalisatie. De toegepaste zelfkalibratiestrategie, gebaseerd op paarsgewijze analyse van de zwevingsfase, elimineert de noodzaak voor externe precisie-instrumenten voor golflengtemeting. Deze aanpak reduceert ruisversterking en verbetert de diepteprecisie over een groot bereik, waardoor de toepasbaarheid van DH voor grootschalige, hoog-precieze industriële inspectie wordt vergroot.

Samenvattend toont dit proefschrift aan dat vooruitgang in zowel het ontwerp van optische systemen als rekenkundige reconstructie de belangrijkste beperkingen van DH in de industriële metrologie systematisch kan verlichten. Door het dieptebereik uit te breiden en zowel de laterale resolutie als de diepteprecisie te verbeteren, vergroten de voorgestelde methoden de inzetbaarheid van DH, met behoud van de intrinsieke voordelen van volledig gezichtsveld beeldvorming en kwantitatieve fasereconstructie.

1

INTRODUCTION

The continuous growth of computing power has fundamentally reshaped modern society, enabling innovations ranging from smartphones and cloud computing to artificial intelligence and autonomous vehicles. This progress has been driven by the semiconductor industry's ability to shrink transistor dimensions, a trend commonly described by Moore's law [1]. Downscaling transistor dimensions allows more transistors to be integrated into the same chip area, thereby increasing performance, efficiency, and reducing cost per function. However, as device dimensions have scaled from the ∼20 µm channel length of the first MOSFET in 1959 to today's 3 nm process node [2–4], the manufacturing process has faced severe challenges. At the current scales, the tolerance for fabrication errors becomes extremely small: even a single speck of dust or a sub-nanometer size deviation can compromise device functionality, leading to significant yield loss. The application of metrology in the production process is critical to guaranteeing semiconductor device quality and optimizing production yield. Metrology can be implemented throughout the fabrication workflow – from lithography and etching to deposition, doping, and final device packaging – ensuring that critical dimensions are controlled and defects are detected in the earliest possible stage [5]. However, maintaining Moore's law requires increasingly advanced inspection and metrology approaches. The next section covers the semiconductor manufacturing and assembly process, highlights where metrology is applied, and introduces key metrology technologies.

1.1. INSPECTION AND METROLOGY IN SEMICONDUCTOR MANUFACTURING

Semiconductor manufacturing is one of the most complex engineering achievements in human history. A typical integrated circuit (IC) requires thousands of sequential processing steps performed in cleanroom environments to transform a blank silicon wafer into a packaged chip that typically contains billions of transistors. As summarized in Figure 1.1, the process is often divided into three main stages: 1. the front-end of line, where transistor structures are created on the silicon substrate using repeated cycles of lithography, deposition, etching, and implantation; 2. the middle-of-line, where individual devices are electrically connected through local interconnects; 3. the back-end of line, where multiple wiring layers are stacked to connect functional blocks, followed by packaging and assembly into usable devices.

In each processing stage, dimensional tolerances and defect requirements are extremely strict. Lithography of multiple layers demands overlay control well below a nanometer, material etching requires precise profile monitoring, and interconnect fabrication requires accurate positioning and connectivity. In these cases, metrology can provide quantitative measurements of dimensions, film thickness, material composition, and surface topography, while inspection focuses on detecting random defects and pattern anomalies. Together, they serve as the backbone of semiconductor manufacturing, providing feedback to maintain yield and performance.

A wide range of metrology and inspection techniques has been developed to

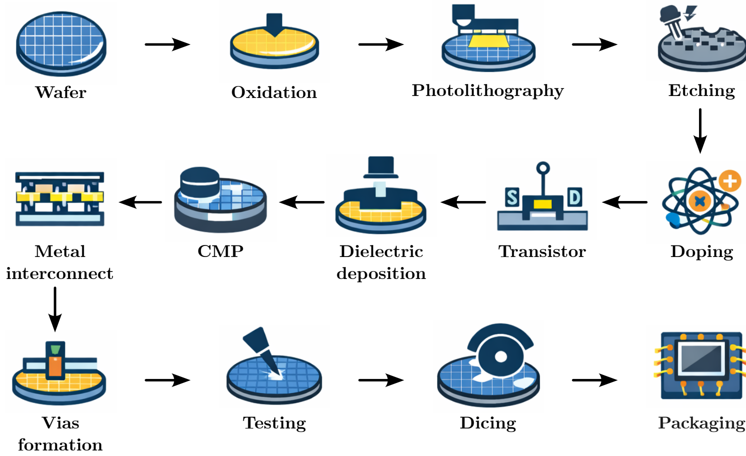

Figure 1.1: Schematic diagrams of the semiconductor manufacturing process.

address these needs. Electron- and probe-based techniques, such as critical dimension scanning electron microscopy (CD-SEM) [6–8] and atomic force microscopy (AFM) [9–11], remain the gold standard in terms of spatial resolution, capable of mapping features at the atomic scale. However, their destructive nature, limited field of view, and low throughput make them unsuitable for high-volume in-line control. X-ray [12–15] and acoustic methods [16–18], provide valuable access to buried structures and package reliability, yet their complexity, cost, or limited spatial resolution restrict their widespread adoption in production environments.

By comparison, optical techniques constitute the backbone of semiconductor metrology because of their non-destructive nature, high throughput, and wide applicability [19–23]. Automated optical inspection based on bright-field or dark-field imaging is essential for defect detection on production lines. Scatterometry [24, 25], another key optical method, infers critical chip dimensions by analyzing optical diffraction patterns. For example, it can be used to monitor lithography processes and ensure the overlay stays within tolerance [24]. Interferometric approaches, including holography, provide surface profiling with nanometer-scale axial precision. Although the lateral resolution of optical approaches is fundamentally limited by diffraction to about half the wavelength of light ($\sim$200 nm), their balance of speed, coverage, and versatility makes them indispensable for in-line monitoring.

As semiconductor manufacturing advances toward smaller dimensions and more sophisticated architectures, the requirements placed on inspection and metrology have expanded beyond speed and accuracy to include comprehensive 3D characterization [26–28]. New technologies therefore aim at obtaining higher throughput, improved accuracy, and the integration of multi-dimensional information. In particular, high-speed, full-field, and non-destructive 3D optical techniques are attracting strong interest because of their ability to unite efficiency with comprehensive in-line characterization. The following section reviews recent advances in 3D optical imaging for next-generation semiconductor metrology.

1

1.2. 3D OPTICAL IMAGING TECHNIQUES FOR INDUSTRIAL INSPECTION

Over the past decades, optical metrology has evolved from simple visual inspection and conventional microscopy to a suite of advanced, automated, and quantitative techniques that support process control across multiple stages of fabrication. Techniques such as white light interferometry (WLI), optical coherence tomography (OCT), and confocal laser scanning microscopy (CLSM) have been widely adopted, each offering distinct strengths and facing trade-offs between resolution, imaging depth, speed, and compatibility with complex structures. These methods reflect the ongoing shift from 2D inspection towards volumetric metrology, required to monitor buried features, overlay metrology, and 3D topography in advanced devices.

White light interferometry reconstructs the surface topography by analyzing interference fringes generated by a low-coherence broadband light source [19, 29–32]. The short coherence length confines the interference pattern to a narrow axial region (such as for a Gaussian spectrum, $l_c \approx 0.44\,\lambda_0^2/\Delta\lambda$, where λ_0 is the central wavelength and $\Delta\lambda$ is source bandwidth), providing axial sectioning, which is known as "coherence gating". In practice, coherence-scanning interferometry is used to acquire an axial stack (correlogram) and the coherence peak is localized by envelope detection with peak fitting [32]. Many WLI instruments then perform phase-based refinement at or near the envelope maximum and achieve sub-nanometer height precision [19]. These attributes make WLI well suited to step-height measurement and planarization control.

Despite its strengths, WLI has limitations, such as difficulty to penetrate deep in an object and discriminate between multiple reflections from multilayer objects, leading to ambiguous signals. Furthermore, the reliance on mechanical axial scanning limits imaging throughput and makes the technique sensitive to vibrations, posing a challenge for fully in-line manufacturing applications.

Optical coherence tomography is another low-coherence interferometric technique that recovers depth-resolved reflectivity and is widely used in ophthalmic applications [20, 33, 34]. Fourier-domain OCT measures the interferometric spectrum $I(k)$ versus wavenumber k. For spectral-domain OCT, the wavenumbers are measured in parallel with a spectrometer whereas for swept-source OCT they are measured sequentially in time. A discrete Fourier transform (DFT) of the acquired spectrum yields an axial reflectivity profile (A-scan), with axial resolution set by the source bandwidth (for a Gaussian spectrum, $\Delta z \approx 0.44\,\lambda_0^2/\Delta\lambda$). As shown in Figure 1.2, for a sample with three reflecting interfaces at z_1, z_2, z_3, the interferometric spectrum $I(k)$ contains distinct fringes with spatial frequencies determined by their respective optical path delays; the detector records their linear superposition (top-right of Figure 1.2). After k-linearization and DFT, three pronounced peaks appear in the depth domain, each corresponding to one interface; because $I(k)$ is real-valued, the peaks occur in symmetric pairs. By acquiring A-scans at each lateral position over an x–y grid, a volumetric dataset $r(x, y, z)$, also called a C-scan, is reconstructed. A B-scan is a cross-section $r(x, z)$ along a

lateral line, revealing stratification and interfaces.

In an industrial context, OCT can non-destructively probe through transparent or weakly scattering media and visualize buried interfaces, voids, and defects [35, 36]. Limitations include sensitivity roll-off in depth, scattering-induced signal decay (imaging depth typically up to a few millimeters), and remaining opto-mechanical demands for fast lateral scanning and stable integration.

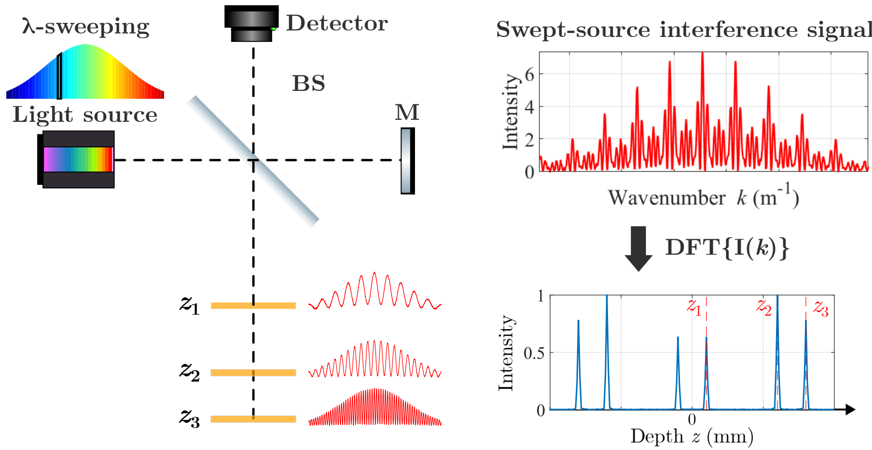

Figure 1.2: Schematic diagram of swept-source OCT. BS: beam splitter; M: mirror. DFT of the interference signal $I(k)$ yields the depth profile (A-scan). Peaks correspond to reflectors at z_1, z_2, z_3.

Confocal laser scanning microscopy employs point illumination and a pinhole in the detection path to reject out-of-focus light [37, 38], thereby achieving optical sectioning with a lateral resolution down to ∼200 nm and an axial resolution ∼500 nm. By stacking tens to hundreds of X-Y images at successive focal depths, CLSM can reconstruct detailed 3D volumes, making it well-suited to characterize surface topography and roughness [39, 40]. Its primary limitation remains low throughput. Although line-scan and spinning-disc confocal variants can improve imaging speed, this comes at the expense of more complex optics and calibration overhead.

Technique	Lateral Res.	Axial Res.	Limitations
WLI	∼1 µm	<1 nm	Slow, multilayer ambiguity
OCT	∼5 µm	1 µm to 10 µm	Signal decay, scattering
CLSM	∼200 nm	∼500 nm	Low throughput, high complexity

Table 1.1: Comparison of principal 3D optical metrology techniques in semiconductor inspection.

A concise comparison of these optical metrology techniques is presented in Table 1.1. Although each method has established itself in specific application

niches, none fully meets the industry's growing demand for high-speed, high-throughput, and robust 3D characterization. This is especially the case as devices have more and more layers and semiconductor architectures become more complex. This gap drives the search for next-generation imaging solutions capable of delivering both high throughput and accuracy, even in challenging industrial environments.

Digital holography (DH) has emerged as a promising candidate, providing quantitative phase imaging for the precise mapping of surface height or thickness variations. As a single-shot, full-field technique, it enables rapid and robust 3D characterization of semiconductor structures. In this thesis, DH is introduced and explored as a next-generation optical metrology approach. In the next section, a detailed discussion of the working principles, implementation, and industrial challenges of DH will follow.

1.3. DIGITAL HOLOGRAPHY FOR HIGH-SPEED FULL-FIELD OPTICAL METROLOGY

The concept of holography was first introduced by Dennis Gabor in 1948 [41], initially in the context of electron microscopy. With the advent of coherent light sources such as lasers, it was quickly extended into the optical domain and became a powerful tool for recording and reconstructing wavefronts. In conventional holography, interference patterns are recorded on a photographic plate and reproduced optically. In contrast, digital holography replaces the photographic plate with a digital image sensor and reconstructs the wavefront numerically. This transition from analog to digital has enabled flexible, real-time, and computationally robust optical field reconstructions, opening new opportunities in industrial inspection and scientific imaging.

Digital holography can be regarded as a computational optical imaging technique that combines interferometry with numerical signal processing. From the intensity interference pattern, it retrieves the full optical field, including both amplitude and phase, thereby enabling quantitative phase imaging. This capability allows precise mapping of surface topography, refractive index sensing, and measuring material thickness variations with nanometer-scale sensitivity, making digital holography particularly attractive for high-resolution, non-destructive 3D metrology.

In this context, lensless DH is particularly attractive because it shifts part of the image-formation task from physical optics to numerical reconstruction. By removing the objective lens, the optical system can be made more compact, less sensitive to lens aberrations, and easier to integrate into constrained industrial inspection environments. More importantly, placing the sample close to the image sensor enables a large field of view and avoids mechanical focusing. The trade-off is that the achievable lateral resolution becomes strongly linked to sensor sampling and the effective numerical aperture, which motivates the resolution analysis and system designs discussed in this thesis.

1.3.1. BASIC PRINCIPLES OF DIGITAL HOLOGRAPHY

A time-independent optical field can be expressed in complex notation as

$$O(x, y) = A(x, y) \exp\left[i\phi(x, y)\right] , \tag{1.1}$$

where $A(x, y)$ is the amplitude, related to the light intensity, and $\phi(x, y)$ is the phase, which carries information about the optical path length. However, image sensors measure only intensity, and phase information is completely lost during the detection process. Digital holography overcomes this challenge by superimposing the object wavefront with a well-defined reference beam. The resulting intensity pattern, referred to as a hologram, encodes the hidden phase information into measurable intensity modulations. The implementation of digital holography thus consists of two key steps: hologram recording, where the interference between object and reference fields is captured on a digital sensor, and numerical reconstruction, in which computational algorithms retrieve the full wavefield from the hologram.

In the recording step, the field emitted by a coherent light source (e.g., a laser) is split into two beams by a beam splitter: one beam illuminates the object, and the resulting transmitted or back-scattered optical field is called the object beam; the other beam propagates directly to the detector without interacting with the object, serving as the reference beam R. The interference pattern (hologram) formed by the superposition of these two beams is recorded using a digital sensor and can be expressed as

$$\begin{aligned} I(x, y) &= |O + R|^2 \\ &= |O|^2 + |R|^2 + OR^* + O^*R \,. \end{aligned} \tag{1.2}$$

The third term in the above equation OR^* or the fourth O^*R (conjugate term) contains the full information of the object wavefront. The core purpose of digital holography is to isolate and extract this information numerically. Depending on the geometry of the optical configuration, O and R may either be collinear (in-line holography) or intersect at an angle on the sensor plane (off-axis holography). Each configuration requires different reconstruction strategies, which will be discussed separately in later sections. Importantly, because the entire interference pattern is recorded in a single exposure, digital holography inherently provides full-field imaging, where the wavefront over the entire sensor is reconstructed simultaneously.

IN-LINE DIGITAL HOLOGRAPHY

In the in-line DH configuration, the reference and object beams are collinear, that is, they propagate along the same optical axis, resulting in overlap of the interference and autocorrelation terms. To extract the complex object field from this configuration, phase-shift techniques [42–44] are commonly employed.

A common approach is the four-step phase shift method, in which four holograms are recorded with a relative phase shift of $\pi/2$ introduced sequentially. This phase modulation can be implemented by precisely adjusting the optical path length using a piezoelectric translation stage. Let the recorded holograms be denoted as $I_0(x, y; 0)$, $I_1\left(x, y; \frac{\pi}{2}\right)$, $I_2(x, y; \pi)$, and $I_3\left(x, y; \frac{3\pi}{2}\right)$. The complex cross-term OR^*,

which contains the amplitude and phase information of the object wavefront, can then be reconstructed as:

$$OR^* = \frac{1}{4}\left[(I_0 - I_2) + i(I_1 - I_3)\right] . \tag{1.3}$$

Assuming that the reference phase is constant (a plane wave), or can be subtracted from the cross term based on prior knowledge, the phase distribution of the object is computed as:

$$\phi(x, y) = \tan^{-1}\left(\frac{I_1 - I_3}{I_0 - I_2}\right) . \tag{1.4}$$

Although an in-line DH setup provides higher imaging resolution, its requirement for separate phase shifted acquisitions limits its application to static or slowly varying objects.

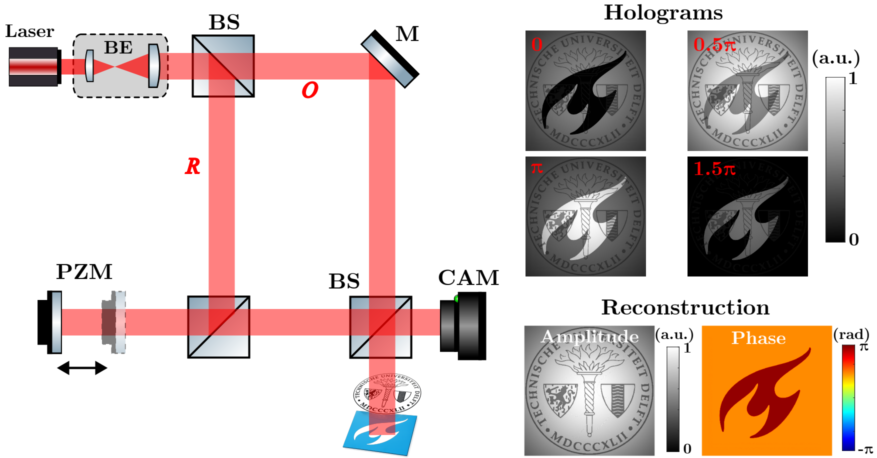

Figure 1.3: Schematic diagram of an in-line digital holography setup. BE: beam expander; BS: beam splitter; M: mirror; PZM: piezoelectric mirror; CAM: 2D monochrome camera.

OFF-AXIS DIGITAL HOLOGRAPHY

In the off-axis configuration, a small angle θ is introduced between the object beam O and reference beam R, such that their interference on the sensor plane has a spatial carrier frequency. A typical off-axis DH setup is illustrated in Figure 1.4, where the object beam reflects from the sample, while the reference beam is tilted with respect to the normal vector of the sensor plane. The reference beam is commonly modeled as a tilted plane wave:

$$R(x, y) = |R| \exp\left[i2\pi\left(f_{rx}x + f_{ry}y\right)\right] , \tag{1.5}$$

where $|R|$ is the complex amplitude and $f_{rx} = \sin(\theta_x)/\lambda\, , f_{ry} = \sin(\theta_y)/\lambda$ are the spatial carrier frequencies introduced by the off-axis tilt.

The resulting hologram intensity $I(x, y)$, as expressed by Eq. (1.2), has three components: 1. the zero-order term $|O|^2 + |R|^2$, 2. the cross-term OR^*, and 3. the complex conjugate O^*R. By applying a 2D Fourier transform to the hologram, these components become spatially separated in the frequency domain. As shown in the upper right corner of Figure 1.4, the cross-term OR^* is shifted away from the origin, enabling its isolation using a band-pass spectral filter $H(f_x, f_y)$ which is indicated by red dashed circle in the figure. The filtered spectrum is then transformed back to the spatial domain to reconstruct the complex object field OR^*:

$$OR^*(x, y) = \mathcal{F}^{-1}\left\{H(f_x, f_y) \cdot \mathcal{F}\left\{I(x, y)\right\}\right\} \, , \tag{1.6}$$

where $\mathcal{F}$ and $\mathcal{F}^{-1}$ denote Fourier and inverse Fourier transform, respectively. Similar to the in-line case, the above reconstruction yields the product OR^*, not O directly. However, if the reference beam R is a plane wave with constant amplitude and a known phase gradient, the object field O can be recovered (up to a constant phase term) by normalizing OR^* with the known reference field numerically. Subsequently, the phase distribution is obtained from the argument of the reconstructed field: $\phi(x, y) = \arg\left(O(x, y)\right)$.

Off-axis holography remains one of the most widely used configurations in digital holography, owing to its ability to perform full-field quantitative phase retrieval from a single camera exposure. This single-shot capability is particularly valuable in industrial and biomedical applications, where dynamic scenes or vibrations preclude multi-frame techniques such as required for the in-line approach. However, off-axis holography entails a trade-off in spatial resolution due to bandwidth constraints and requires careful off-axis angle alignment to avoid spectral overlap and aliasing artifacts.

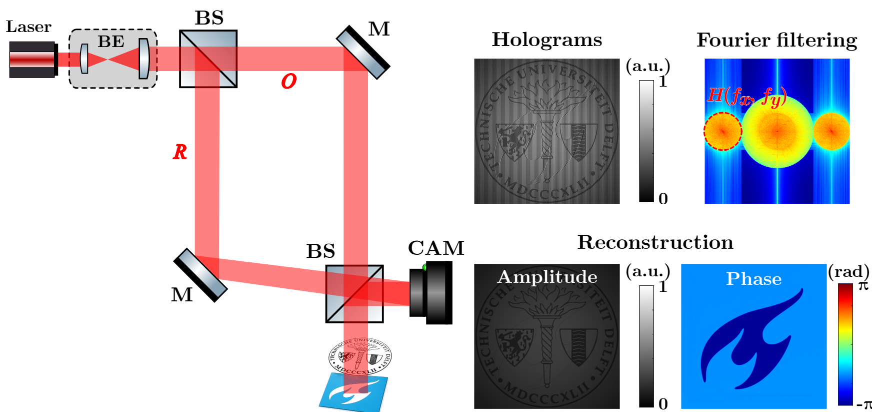

Figure 1.4: Schematic diagram of off-axis digital holography setup. BE: beam expander; BS: beam splitter; M: mirror; CAM: 2D monochrome camera.

Unlike scanning-based methods such as confocal microscopy or white-light interferometry, both in-line and off-axis DH captures the entire field of view in a single acquisition. The off-axis configurations further supports single-shot retrieval of the complex field, making DH advantageous for dynamic samples or environments sensitive to mechanical vibration.

1.3.2. FOURIER DOMAIN DESCRIPTION OF OFF-AXIS DIGITAL HOLOGRAPHY

The ability of off-axis digital holography to perform single-shot measurement hinges on effective separation of the cross-term from the zero-order terms in the frequency domain. This section examines how such separation is achieved and which practical factors must be considered.

Assume that the object field $O(x,y)$ has a 2D Fourier transform $\tilde{O}(f_x, f_y)$ with a bandwidth of $2B$, i.e., the full width of the spectrum in the spatial-frequency domain [45]. The reference beam introduces a carrier frequency determined by the off-axis angle θ (see Eq. (1.5)), which shifts the spectrum of the cross-term $OR^*(x,y)$ in the frequency domain. Specifically, $\mathcal{F}\{OR^*(x,y)\} = \tilde{O}(f_x+f_{rx}, f_y+f_{ry})$ indicates a spectral shift of (f_{rx}, f_{ry}) induced by the reference beam's spatial frequency. As illustrated in Figure 1.5, a typical off-axis hologram spectrum comprises three distinct circular regions: the smaller sidebands represent the spectra of the cross-term and its conjugate, each with a spectral width of $2B$, while the central circle corresponds to the spectrum of the zero-order autocorrelation term with a spectral width of $4B$. To prevent spectral overlap between the terms, the off-axis angle must be large enough. However, the pixel size of the image sensor, denoted as $\Delta x = \Delta y$, defines the the Nyquist frequency, which represents the maximum spatial frequency that can be well reconstructed. After discrete Fourier transform, this frequency defines the full width of the spatial spectrum, also called the "sensor bandwidth". This Nyquist frequency imposes an upper bound on the off-axis angle, if it is too large, spectral aliasing occurs.

Therefore, in practice, the selection of the off-axis angle needs to consider both the pixel size Δx and the bandwidth of the object field $2B$. In an imaging system, the spectral width of the object field is related to the cutoff frequency which is determined by the numerical aperture NA and the wavelength λ, i.e., $f_{c,obj} = \mathrm{NA}/\lambda$. On the imaging plane, the cutoff frequency of the image is further influenced by the system's imaging magnification M: $f_{c,img} = f_{c,obj}/M$. In addition, the cutoff frequency refers to the maximum radial spatial frequency, so the bandwidth equals the cutoff frequency, $B = f_{c,img}$. According to the above equations and the illustration in Figure 1.5, it is easy to obtain the following parameters: 1. the condition for fully separating the cross-term and the zero-order term without spectral overlap is $f_{r,x} \geq 2B + B = 3B$; 2. the condition to avoid spectral aliasing is $f_{r,x} + B \leq 1/(2\Delta x)$. By combining the above two equations,

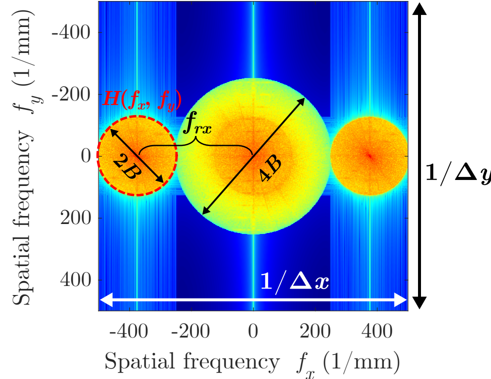

Figure 1.5: Schematic of the spectrum of an off-axis hologram, where the reference beam has $\theta_x \neq 0$ and $\theta_y = 0$. Sidebands correspond to the spectra of the cross and conjugate terms (each with a bandwidth of $2B$); the central lobe is the zero-order autocorrelation term with a spectral width of $4B$. The separation between the cross-term and the zero-order is f_{rx}. The overall spectral extent corresponds to the sensor sampling intervals Δx, Δy. Red dashed line indicates the filtering window $H(f_x, f_y)$.

the requirement for the off-axis angle θ is obtained as:

$$\begin{cases} \sin\theta \geq 3\dfrac{\mathrm{NA}}{M}, & \text{(No overlap)} \\ \sin\theta \leq \dfrac{\lambda}{2\Delta x} - \dfrac{\mathrm{NA}}{M}, & \text{(No aliasing)} \end{cases} \tag{1.7}$$

While $\theta_y = 0$ is assumed here for simplicity, the derivation remains valid for arbitrary angles provided the spatial frequency constraints are satisfied.

NUMERICAL APERTURE IN LENSLESS OFF-AXIS DIGITAL HOLOGRAPHY

Because in this dissertation lensless DH as a compact and integration-friendly architecture are used, it is important to clarify how the usual imaging parameters change when no objective lens is present. In conventional microscopy based on a $4f$ system, the numerical aperture (NA) is dictated by the objective lens. In a lensless configuration, the NA is usually defined by the acceptance angle subtended by the sensor relative to the sample. Assuming z is the sample-to-sensor distance and $W = N \cdot \Delta x$ the sensor width (with N pixels along $x-$direction), then the maximum collection angle is $\alpha_{\max} \approx \tan^{-1}(W/2z)$, yielding

$$\mathrm{NA} = \sin(\alpha_{\max}) \, . \tag{1.8}$$

The pixel size of the image sensor is generally in the micrometer range. To show the careful system configuration, we take, as an example, a $10\times$ magnification and $\mathrm{NA} = 0.25$ objective lens, with a high quality image sensor ($\Delta x = \Delta y = 3.45\,\mu\mathrm{m}$).

Substituting these values into Eq. (1.7), it can be calculated that to prevent the cross-term from overlapping with the zero-order term, the off-axis angle θ must satisfy $\geq 4.3°$; to prevent aliasing caused by the cross-term's spectrum exceeding the sensor bandwidth, the off-axis angle needs to be $\theta \leq 3.8°$. Therefore, to meet both conditions simultaneously places high demands on the sensor's pixel size (using smaller pixel sizes is more advantageous). Alternatively, balanced detection, numerical correction, and other techniques can be employed to suppress the zero-order component and improve the effective use of the Fourier domain.

Thus, the lateral resolution of digital holography depends on both the wavelength and NA, but also on the camera pixel size. In the absence of aliasing and spectral overlap, the lateral resolution is diffraction-limited, as described by the Abbe criterion:

$$r_a = \frac{\lambda}{2\mathrm{NA}} \, . \tag{1.9}$$

However, when spectral aliasing or significant spectral overlap occurs, some frequency information will inevitably be lost during the step of Fourier filtering. Therefore, the best achievable resolution in this case is two times the pixel size ($2\Delta x$). Although increasing NA improves resolution, the spatial resolution is ultimately limited by the pixel pitch because of the discrete spatial sampling of the sensor.

1.3.3. KEY FEATURES AND PARAMETERS OF DIGITAL HOLOGRAPHY FOR METROLOGY

Digital holography (DH) integrates quantitative phase sensitivity with full-field imaging and potentially single-shot measurement, making it well suited for high-throughput inspection workflows in semiconductor manufacturing. This section outlines the core characteristics that establish DH as a versatile and robust 3D optical metrology technique, with an emphasis on quantitative phase imaging and digital refocusing. The former enables the extraction of surface topography or refractive-index variations directly from the recorded interference pattern, while the latter allows numerical adjustment of the focal plane after acquisition, eliminating the need for mechanical scanning. These features are particularly valuable in industrial contexts where speed, precision, and non-contact operation are critical.

QUANTITATIVE PHASE IMAGING AND MEASUREMENT DEPTH RANGE

A fundamental strength of digital holography (DH) is its ability to reconstruct the complex optical field, both amplitude and phase, from the recorded intensity pattern. The retrieved phase distribution $\phi(x, y)$ encodes the optical path difference between the object and reference waves, which can consequently be directly related to the surface profile or refractive-index variations of the sample.

In reflection-mode configurations, a height variation $h(x, y)$ on the sample surface introduces an varying optical path lengths, which are governed by the refractive index of the medium n, and the angle of incidence θ_i with respect to the normal of

the sample, as illustrated in Figure 1.6. The corresponding phase shift $\Delta\phi(x, y)$ is

$$\Delta\phi(x,y) = 2knh(x,y)\cos\theta_i = \frac{4\pi nh(x,y)}{\lambda}\cos\theta_i\,, \tag{1.10}$$

where λ is the illumination wavelength and n is the refractive index of the surrounding medium (typically air, $n = 1$). In the case where the reference beam is a plane wave, $\Delta\phi(x, y)$ differs from $\phi(x, y)$ up to a constant phase, which does not affect the mapping of height variations about the object surface. Solving for $h(x, y)$ in the case of normal incidence $\theta_i = 0$ and $n = 1$, Eq. (1.10) reduces to the familiar expression

$$h(x,y) = \frac{\Delta\phi(x,y)}{4\pi}\lambda\,. \tag{1.11}$$

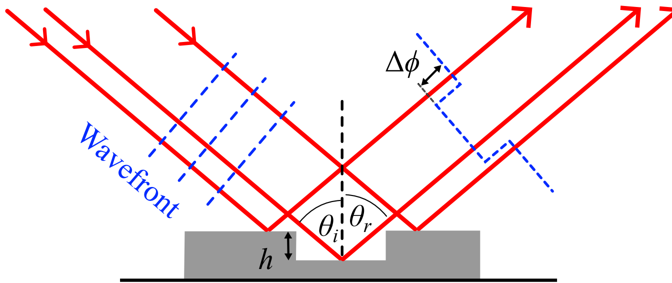

Figure 1.6: Illustration of phase difference and path difference

The relationship given in Eq. (1.11) demonstrates that digital holography enables nanometer-scale axial sensitivity, provided that the phase retrieval and unwrapping processes are performed with high precision. At the same time, this equation also reveals a fundamental limitation: the measurable depth range is directly linked to the phase variation $\Delta\phi(x, y)$, which is inherently confined to a 2π range due to the periodic nature of the optical phase, leading to wrapped phase measurements, which can be expressed as:

$$\phi_{\text{wrapped}} = \Delta\phi(x,y) \bmod 2\pi\,. \tag{1.12}$$

This phenomenon is known as the "2π ambiguity", as the wrapping introduces ambiguity when interpreting phase values in terms of optical path differences exceeding a single wavelength. In reflection-mode configurations, the optical path difference induced by surface height variation is $2h$, due to the round-trip of the wave. Consequently, the maximum unambiguous height difference that can be recovered without additional post-processing is $\lambda/2$. Beyond this limit, discontinuities or artificial jumps may appear in the reconstructed height map.

It is important to distinguish the concept of depth range—that is, the maximum surface height variation without phase ambiguity—from the depth of field (DOF), a parameter commonly used in conventional microscopy. The DOF defines the

axial extent over which objects appear acceptably sharp in a recorded image and is primarily determined by the NA of system, according to [46]:

$$\mathrm{DOF} \approx \frac{2n\lambda}{\mathrm{NA}^2}\,. \tag{1.13}$$

Although this relationship also holds for holographic imaging, digital holography fundamentally differs in that it is not constrained by a fixed focal plane. Once the complex optical field is reconstructed, the wavefront can be numerically propagated to any axial position. This process, known as digital refocusing or numerical propagation, allows one to retrieve in-focus images at arbitrary depths post-acquisition, effectively decoupling image sharpness from the physical focal plane [47].

NUMERICAL REFOCUSING AND LENSLESS IMAGING

Numerical refocusing in DH is based on scalar diffraction theory and is implemented by propagating the complex wavefront retrieved at the sensor plane to other axial positions. Let $U_{z=0}(x,y)$ denote the complex field at the sensor plane ($z=0$). The field at a distance d along the optical axis, $U_{z=d}(x,y)$, can be calculated using the angular spectrum method with

$$U_{z=d}(x,y) = \mathcal{F}^{-1}\left\{\exp\left(i2\pi d\sqrt{\frac{1}{\lambda^2} - f_x^2 - f_y^2}\right)\cdot\mathcal{F}\left\{U_{z=0}(x,y)\right\}\right\}, \tag{1.14}$$

where f_x and f_y are the spatial frequency components in the x and y directions, and $\mathcal{F}$ and $\mathcal{F}^{-1}$ denote the forward and inverse Fourier transforms. This computational approach allows axial scanning with arbitrary resolution and without the mechanical inaccuracies associated with stage motion.

This capability enables lensless imaging, wherein the object is placed directly in front of the sensor without any intervening optics. Because the phase and amplitude of the wavefront are recovered numerically, image formation no longer depends on physical lenses, which simplifies the system design and eliminates lens-induced aberrations. For instance, in a lensless DH configuration with an object-to-sensor distance of 60 mm, digital refocusing can be used to computationally back-propagate the recorded field to the object plane. Figure 1.7 illustrates this process. For each distance, the left and right panels represent the reconstructed amplitude and phase maps, respectively. As the propagation distance approaches 60 mm, the sharpness of the object images increases.

Beyond eliminating the need for mechanical focusing, numerical refocusing also supports volumetric imaging by reconstructing multiple axial slices from a single hologram [48, 49]. This is particularly advantageous for samples with distributed 3D structures or layered components, as it enables depth-resolved analysis without repeated acquisition or complex scanning mechanisms.

The effectiveness of digital holography relies not only on its computational flexibility, but also on the physical coherence properties of the light source. Both

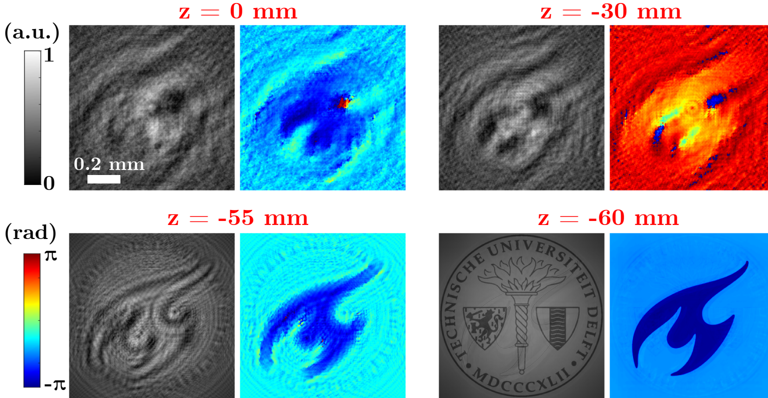

Figure 1.7: Demonstration of numerical refocusing and reconstruction results at indicated axial positions. Each pair consists of an amplitude image (left) and its phase map (right). The sample is located 60 mm from the sensor plane ($z = 0$); both maps become progressively sharper as the propagation distance approaches this position.

temporal and spatial coherence are essential for producing stable interference fringes. Specifically, the temporal coherence length must exceed the optical path difference between the object and reference beams, as well as any axial variation introduced by the sample topography. Spatial coherence, in turn, governs the fringe visibility across the field of view. While highly coherent laser sources satisfy these requirements, they are also susceptible to parasitic interference and speckle noise arising from internal reflections and coherent scattering by non-smooth surfaces of the optics. These noise sources can degrade image quality and measurement precision. Mitigation strategies include polarization control, optical isolation, angular diversity, and post-processing techniques such as background subtraction and speckle filtering.

In short, DH offers a unique platform for high-throughput, non-contact optical metrology. Its ability to recover phase information with nanometer axial sensitivity, combined with digital refocusing and lensless imaging capabilities, enables a wide range of industrial applications. In semiconductor manufacturing, DH and related coherent optical metrology methods have been explored for full-field surface inspection [50], process monitoring [26, 27], and thickness mapping of dielectric and multilayer film stacks [51]. These strengths make DH a compelling candidate for next-generation in-line 3D metrology systems.

1.4. CHALLENGES FOR INDUSTRIAL METROLOGY WITH DH

Despite its broad applicability and unique advantages, digital holography (DH) still faces several key challenges when deployed in demanding industrial metrology tasks. These limitations stem both from the fundamental physics of

phase-based imaging and from practical constraints inherent in current DH system designs. For clarity, the major challenges are categorized into three primary areas: (1) limited unambiguous measurement depth range, (2) resolution limitations due to sensor pixel size, and (3) difficulty in resolving multi-interface structures.

1.4.1. LIMITED MEASUREMENT DEPTH RANGE

As discussed in the previous section, single-wavelength DH suffers from a fundamental limitation in axial measurement range due to the 2π phase ambiguity. Since the phase retrieved from interference is inherently wrapped modulo 2π, the unambiguous height range is confined to $\lambda/2$ in reflection-mode configurations. Extending this depth range is a central topic in phase imaging research, with solutions falling broadly into two categories: algorithmic phase unwrapping and physics-based approaches.

When the surface gradient is sufficiently small and the phase variation is spatially smooth, 2D phase unwrapping algorithms [52–54] can be applied to reconstruct the continuous phase by adding integer multiples of 2π. However, these algorithms can be computationally demanding and rely on spatial continuity of the phase and are highly sensitive to sharp discontinuities, noise, or spatial undersampling, which are common in semiconductor samples with steps, trenches, or defects.

In such cases, physics-based approaches offer a more robust alternative. Among them, dual-wavelength digital holography (DWDH) introduces a second laser with a different wavelength to generate a synthetic wavelength that is significantly longer than either of the original wavelengths. Figure 1.8(a) illustrates the variation of the real components of the optical fields at two wavelengths λ_1 and λ_2 as a function of height. The two signals are slightly out of phase, arising from the inherent difference in their wavelengths. Figure 1.8(b) shows the phase of the signals ϕ_1 and ϕ_2 and the 2π phase ambiguity.

By acquiring two phase maps, ϕ_1 and ϕ_2, corresponding to wavelengths λ_1 and λ_2, a synthetic phase (also referred to as the beat phase) Φ is constructed as

$$\Phi = \arg\left(\frac{\exp(i\phi_1)}{\exp(i\phi_2)}\right) = \arg\left(\frac{\exp\left(i\frac{4\pi}{\lambda_1}h\right)}{\exp\left(i\frac{4\pi}{\lambda_2}h\right)}\right) = \arg\left(\exp\left(i4\pi\frac{h}{\Lambda}\right)\right), \tag{1.15}$$

with an effective synthetic wavelength Λ defined as:

$$\Lambda = \frac{\lambda_1\lambda_2}{|\lambda_1 - \lambda_2|}, \tag{1.16}$$

The corresponding beat signal is periodic over a range defined by the synthetic wavelength Λ. Hence, the beat phase reconstruction has a phase wrapped over a much longer distance, since $\Lambda \gg \lambda_{1,2}$, and the unambiguous depth range is extended to $\Lambda/2$, enabling the measurement of structures with larger height variations without relying on unwrapping algorithms. This approach is particularly valuable for characterizing high-aspect-ratio features such as deep trenches, vias, and step heights in semiconductor wafers.

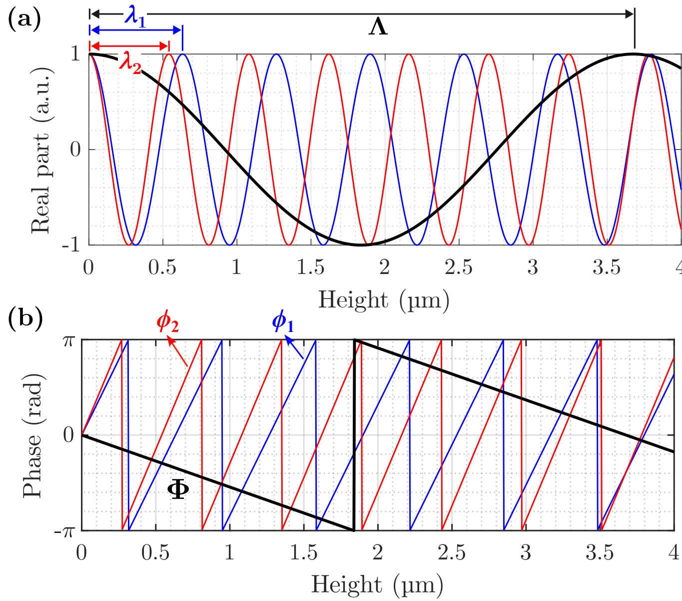

Figure 1.8: Illustration of the 2π ambiguity and its mitigation via a dual-wavelength scheme. (a) The real part of the optical field varies periodically with surface height, with the period proportional to wavelength. (b) Phase of the optical signal retrieved as a function of surface height at different wavelengths. Because of 2π ambiguity, a single phase can correspond to multiple height values. The synthesized signal in the dual-wavelength scheme show a longer effective period, extending the unambiguous range.

1.4.2. RESOLUTION LIMITATIONS DUE TO PIXEL SIZE AND SPECTRAL OVERLAP

As discussed in Section 1.3.2 and illustrated in Figure 1.5, the pixel size Δx of the image sensor imposes a fundamental limit on the measurable spatial frequencies. Thus, in digital holography, the lateral resolution is determined both by the numerical aperture (NA) of the system and the sensor pixel size. According to the Nyquist sampling theorem, the maximum spatial frequency is $f_{\max} = 1/(2\Delta x)$, which imposes a sampling cutoff independent of the optical NA. When the spatial bandwidth of the object exceeds this limit, spectral aliasing becomes unavoidable. Moreover, in off-axis holography, the cross-term OR^* must be isolated in the Fourier domain via bandpass filtering to remove the twin-image and zero-order artifacts. This filtering step further reduces the effective spatial bandwidth of the reconstruction.

When we define the filter window $H(f_x, f_y)$ with spectral cutoff radius of f_c, as depicted in Figure 1.9(a), the resulting filtered complex field defines the upper bound of the spatial-frequency content preserved in the reconstructed image. The

corresponding intensity image – formed via autocorrelation – therefore would have a spatial-frequency cutoff of $2f_c$. For a periodic line/space target, this cutoff corresponds to a half-pitch of $1/(4f_c)$ in the spatial domain. According to the Abbe criterion, the spatial resolution is given by:

$$r_{x,y} = 2\frac{1}{4f_c} = \frac{1}{2f_c}\,. \tag{1.17}$$

Hence, for an off-axis DH system in which the zero-order has been suppressed, the spectrum can be optimally arranged as illustrated in Figure 1.9(b) (considering only an off-axis angle in the x-direction for simplicity). In this configuration, the carrier spatial frequency is $f_{rx} = 1/(4\Delta x)$, and the cutoff radius of the filter window can be increased to $f_c = 1/(4\Delta x)$ accordingly. Therefore, the achievable optimal resolution is approximately $2\Delta x$, i.e., two pixels.

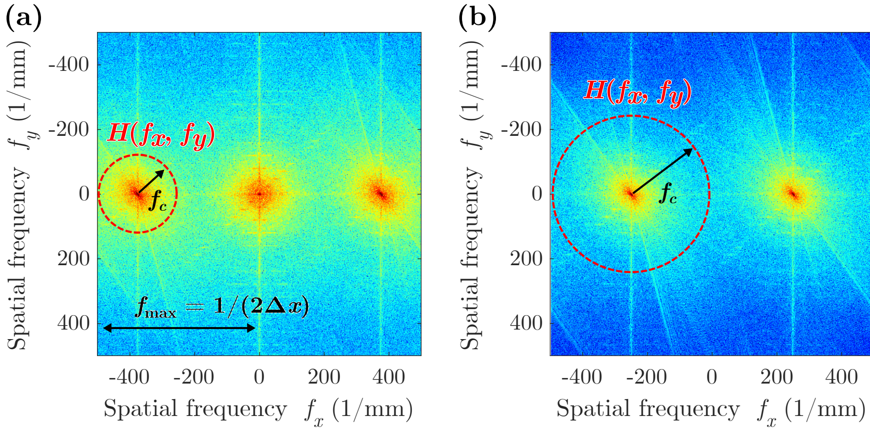

Figure 1.9: Spectrum and resolution limit in off-axis DH. (a) In the presence of the zero-order, the size of the filter window $H(f_x, f_y)$ is limited due to the need to avoid spectral overlap and aliasing. (b) Optimized spectral distribution after zero-order suppression, where the filter cutoff $f_c = 1/(4\Delta x)$.

This pixel-size bottleneck poses a critical challenge for industrial inspection tasks, where detecting microscale defects is essential for process control and yield optimization. Increasing magnification while imaging with the same NA can reduce the object spectrum bandwidth and thereby address this problem. Other advanced techniques such as synthetic aperture, and ptychography have been proposed to overcome this limitation by effectively increasing the system's spatial frequency coverage [55, 56]. However, these methods typically require multi-frame acquisition, or precise motion control, which complicate system design and undermine throughput. As a result, improving spatial resolution while maintaining single-shot advantage remains a key technical challenge for DH in high-throughput industrial environments.

1.4.3. Difficulty in imaging multi-interface structures

Many real-world samples, particularly in semiconductor and materials research, exhibit multiple partially reflective interfaces within a single field of view—such as transparent layered stacks, oxide films, or biological samples. When the sample is illuminated by coherent light, these multiple reflections generate overlapping optical fields, leading to superimposed phase contributions in the captured hologram:

$$U(x, y) = \sum_{m=1}^{M} A_m(x, y) \exp\left[i\phi_m(x, y)\right] , \tag{1.18}$$

where each term corresponds to a distinct reflective interface at depth z_m. Although digital refocusing can numerically propagate the complex field to different axial planes, it cannot disentangle the contributions of overlapping wavefronts when their optical paths fall within the coherence length of the source. This leads to phase mixing and image artifacts, particularly when the inter-layer spacing is comparable to the coherence length or when multiple interfaces lie within the same coherence volume. Internal reflections and secondary interference terms further complicate the reconstruction, degrading the interpretability of phase maps and hindering accurate surface localization.

Addressing this challenge requires a comprehensive theoretical model of light-object interaction, as well as a combination of multi-wavelength acquisition and advanced reconstruction algorithms capable of separating multi-depth interference signals. Such approaches are under active investigation but currently remain a major hurdle for applying DH to transparent or layered materials with industrial relevance.

1.5. Outline of this dissertation

Building upon the technical characteristics and limitations discussed in the previous section, this dissertation aims to advance digital holography (DH) as a high-speed, robust, and high-resolution imaging modality for inspection and metrology in the semiconductor industry. To this end, we address several critical challenges that currently limit the broader deployment of DH in industrial environments, including the restricted measurement depth range, resolution constraints imposed by sensor pixel size, and difficulties in imaging multi-interface structures. A series of innovations in optical design and reconstruction algorithms are introduced to overcome these limitations while maintaining the advantages of DH.

Chapter 2 addresses the limited unambiguous depth range in conventional DH by introducing a lensless dual-wavelength system designed for compactness and ease of integration. The system operates in single-shot acquisition, which is achieved through spatial frequency multiplexing. The phase precision is theoretically analyzed under shot-noise-limited conditions and experimentally validated with the proposed model. Applications for quantitative chip tilt measurements and calibrated step-height targets are demonstrated experimentally.

Chapter 3 addresses the resolution bottleneck caused by the finite size of the sensor pixels. We present an expanding wavefront illumination scheme that broadens the angular spectrum captured by the sensor, thereby improving lateral resolution without requiring multiple acquisitions in lensless digital holography. This approach effectively overcomes pixel-size-limited resolution without sacrificing the single-shot nature of off-axis DH. Furthermore, in this chapter, we investigate the use of tunable external cavity diode laser (ECDL) and achieve centimeter-level depth range, advancing the application of DH for metrology at macroscopic scales.

Chapter 4 focuses on the challenges of the depth–precision limitation of conventional dual-wavelength DH, where increasing the synthetic wavelength to extend the unambiguous range proportionally degrades height precision. To overcome this trade-off, a multi-wavelength DH framework based on discrete wavelength sampling is developed, enabling depth retrieval through multi-point phase fitting by integrating Fourier-based coarse localization with linear phase regression. This approach decouples the depth range from depth precision, extending the applicability of DH to large-variation scenarios. Furthermore, it offers a potential solution for resolving axial reflections from multiple surfaces at varying depths.

Finally, Chapter 5 concludes the dissertation by summarizing the key contributions described in this thesis, evaluating the limitations of the proposed methods, and outlining directions for future work for next-generation industrial inspection platforms.

REFERENCES

[1] G. E. Moore. *Cramming More Components onto Integrated Circuits*. Electronics **38**, 114–117 (1965).

[2] K. Dawon. *Electric Field Controlled Semiconductor Device*. U.S. pat. 3102230A. Bell Telephone Laboratories Inc. 1963.

[3] Samsung Electronics. *Samsung Begins Chip Production Using 3nm Process Technology With GAA Architecture*. 2022.

[4] TSMC. *TSMC Holds 3 nm Volume Production and Capacity Expansion Ceremony, Marking a Key Milestone for Advanced Manufacturing*. 2022.

[5] Y. Su, J. Shi, Y.-M. Hsu, D.-Y. Ji, A. D. Suer and J. Lee. *Volumetric Nondestructive Metrology for 3D Semiconductor Packaging: A Review*. Measurement **225**, 114065 (2024).

[6] E. Solecky, A. Rasafar, J. Cantone, B. Bunday, A. Vaid, O. Patterson, A. Stamper, K. Wu, R. Buengener, W. Weng and X. Dai. *In-Line E-beam Metrology and Defect Inspection: Industry Reflections, Hybrid E-beam Opportunities, Recommendations and Predictions*. Metrology, Inspection, and Process Control for Microlithography XXXI **10145**, 241–258 (2017).

[7] B. Bunday, A. F. Bello, E. Solecky and A. Vaid. *7/5 nm Logic Manufacturing Capabilities and Requirements of Metrology*. Metrology, Inspection, and Process Control for Microlithography XXXII **10585**, 81–124 (2018).

[8] B. Bunday, A. Cepler, A. Cordes and A. Arceo. *CD-SEM Metrology for Sub-10 nm Width Features*. Metrology, Inspection, and Process Control for Microlithography XXVIII **9050**, 238–257 (2014).

[9] G. Dai, L. Koenders, J. Fluegge and M. Hemmleb. *Fast and Accurate: High-Speed Metrological Large-Range AFM for Surface and Nanometrology*. Measurement Science and Technology **29**, 054012 (2018).

[10] M. P. Murrell, M. E. Welland, S. J. O'Shea, T. M. H. Wong, J. R. Barnes, A. W. McKinnon, M. Heyns and S. Verhaverbeke. *Spatially Resolved Electrical Measurements of SiO_2 Gate Oxides Using Atomic Force Microscopy*. Applied Physics Letters **62**, 786–788 (1993).

[11] D. Hussain, K. Ahmad, J. Song and H. Xie. *Advances in the Atomic Force Microscopy for Critical Dimension Metrology*. Measurement Science and Technology **28**, 012001 (2016).

[12] D. F. Sunday, J. Ren, C. D. Liman, L. D. Williamson, R. Gronheid, P. F. Nealey and R. J. Kline. *Characterizing Patterned Block Copolymer Thin Films with Soft X-rays.* ACS Applied Materials & Interfaces **9**, 31325–31334 (2017).

[13] B. R. Pauw. *Everything SAXS: Small-Angle Scattering Pattern Collection and Correction.* Journal of Physics: Condensed Matter **25**, 383201 (2013).

[14] R. L. Jones, T. Hu, E. K. Lin, W.-L. Wu, R. Kolb, D. M. Casa, P. J. Bolton and G. G. Barclay. *Small Angle X-Ray Scattering for Sub-100 Nm Pattern Characterization.* Applied Physics Letters **83**, 4059–4061 (2003).

[15] P. Gin, M. Wormington, Y. Amasay, I. Grinberg, A. Brady, I. Reichental, K. Matney, J. Zhang and O. Sorkhabi. *Inline Metrology of High Aspect Ratio Hole Tilt and Center Line Shift Using Small-Angle X-Ray Scattering.* Journal of Micro/Nanopatterning, Materials, and Metrology **22**, 031205 (2023).

[16] S. Brand, A. Lapadatu, T. Djuric, P. Czurratis, J. Schischka and M. Petzold. *Scanning Acoustic Gigahertz Microscopy for Metrology Applications in Three-Dimensional Integration Technologies.* Journal of Micro-Nanolithography Mems and Moems **13**, 011207 (2014).

[17] H. Yu. *Scanning Acoustic Microscopy for Material Evaluation.* Applied Microscopy **50**, 25 (2020).

[18] K. Wang, T. Leng, J. Mao and G. Lian. *Design and Optimization of Transmitting Circuit System of Scanning Acoustic Microscope.* Sensors and Actuators A: Physical **334**, 113335 (2022).

[19] P. de Groot. *Principles of Interference Microscopy for the Measurement of Surface Topography.* Advances in Optics and Photonics **7**, 1–65 (2015).

[20] M.-Y. Fu, Z.-H. Yin, X.-Y. Yao, J. Xu, Y. Liu, Y. Dong and Y.-C. Shen. *The Progress of Optical Coherence Tomography in Industry Applications.* Advanced Devices & Instrumentation **5**, 0053 (2024).

[21] J. Xu and S. Zhang. *Status, Challenges, and Future Perspectives of Fringe Projection Profilometry.* Optics and Lasers in Engineering **135**, 106193 (2020).

[22] Y. Shimizu, L.-C. Chen, D. W. Kim, X. Chen, X. Li and H. Matsukuma. *An Insight into Optical Metrology in Manufacturing.* Measurement Science and Technology **32**, 042003 (2021).

[23] R. Leach. *Optical Measurement of Surface Topography.* Springer Berlin Heidelberg, 2011.

[24] C. Messinis, T. T. M. van Schaijk, N. Pandey, V. T. Tenner, S. Witte, J. F. de Boer and A. den Boef. *Diffraction-Based Overlay Metrology Using Angular-Multiplexed Acquisition of Dark-Field Digital Holograms.* Optics Express **28**, 37419–37435 (2020).

[25] X. Chen, H. Gu, H. Jiang, C. Zhang and S. Liu. *Robust Overlay Metrology with Differential Mueller Matrix Calculus.* Optics Express **25**, 8491–8510 (2017).

[26] N. G. Orji, M. Badaroglu, B. M. Barnes, C. Beitia, B. D. Bunday, U. Celano, R. J. Kline, M. Neisser, Y. Obeng and A. E. Vladar. *Metrology for the next Generation of Semiconductor Devices*. Nature Electronics **1**, 532–547 (2018).

[27] R. B. Bergmann, M. Kalms and C. Falldorf. *Optical In-Process Measurement: Concepts for Precise, Fast and Robust Optical Metrology for Complex Measurement Situations*. Applied Sciences **11**, 10533 (2021).

[28] S. Catalucci, A. Thompson, S. Piano, D. T. Branson and R. Leach. *Optical Metrology for Digital Manufacturing: A Review*. The International Journal of Advanced Manufacturing Technology **120**, 4271–4290 (2022).

[29] P. de Groot and X. C. de Lega. *Signal Modeling for Low-Coherence Height-Scanning Interference Microscopy*. Applied Optics **43**, 4821–4830 (2004).

[30] L. Deck and P. de Groot. *High-Speed Noncontact Profiler Based on Scanning White-Light Interferometry*. Applied Optics **33**, 7334–7338 (1994).

[31] J. Schmit and A. Pakuła. 'White Light Interferometry'. *Handbook of Advanced Nondestructive Evaluation*. Springer, Cham, 2019, pp. 421–467.

[32] G. Gianto, F. Salzenstein and P. Montgomery. *Comparison of Envelope Detection Techniques in Coherence Scanning Interferometry*. Applied Optics **55**, 6763–6774 (2016).

[33] D. Huang, E. A. Swanson, C. P. Lin, J. S. Schuman, W. G. Stinson, W. Chang, M. R. Hee, T. Flotte, K. Gregory, C. A. Puliafito and J. G. Fujimoto. *Optical Coherence Tomography*. Science **254**, 1178–1181 (1991).

[34] N. M. Israelsen, C. R. Petersen, A. Barh, D. Jain, M. Jensen, G. Hannesschläger, P. Tidemand-Lichtenberg, C. Pedersen, A. Podoleanu and O. Bang. *Real-Time High-Resolution Mid-Infrared Optical Coherence Tomography*. Light: Science & Applications **8**, 11 (2019).

[35] S.-H. Kim, J.-H. Kim and S.-W. Kang. *Nondestructive Defect Inspection for LCDs Using Optical Coherence Tomography*. Displays **32**, 325–329 (2011).

[36] P. Ekberg, R. Su, E. W. Chang, S. H. Yun and L. Mattsson. *Fast and Accurate Metrology of Multi-Layered Ceramic Materials by an Automated Boundary Detection Algorithm Developed for Optical Coherence Tomography Data*. JOSA A **31**, 217–226 (2014).

[37] S. Yu, Z. Wang, W. Zhao and L. Qiu. *High-Speed and Large-Range Laser Differential Confocal Microscopy Based on Galvanometer and Displacement Stage*. Optics & Laser Technology **186**, 112632 (2025).

[38] H.-R. Chen and L.-C. Chen. *Full-Field Chromatic Confocal Microscopy for Surface Profilometry with Sub-Micrometer Accuracy*. Optics and Lasers in Engineering **161**, 107384 (2023).

[39] J. Li, R. Ma and J. Bai. *High-Precision Chromatic Confocal Technologies: A Review*. Micromachines **15**, 1224 (2024).

1

[40] A. A. Baluev, D. S. Ukolov, A. A. Pechenkin and R. K. Mozhaev. *Application of Confocal Microscopy Methods for Research and Non-destructive Examination of Semiconductor Structures and Integrated Circuits*. 2021 IEEE 32nd International Conference on Microelectronics (MIEL), 135–138 (2021).

[41] D. Gabor. *A New Microscopic Principle*. Nature **161**, 777–778 (1948).

[42] J. H. Bruning, D. R. Herriott, J. E. Gallagher, D. P. Rosenfeld, A. D. White and D. J. Brangaccio. *Digital Wavefront Measuring Interferometer for Testing Optical Surfaces and Lenses*. Applied Optics **13**, 2693–2703 (1974).

[43] I. Yamaguchi and T. Zhang. *Phase-Shifting Digital Holography*. Optics Letters **22**, 1268–1270 (1997).

[44] L. Z. Cai, Q. Liu and X. L. Yang. *Generalized Phase-Shifting Interferometry with Arbitrary Unknown Phase Steps for Diffraction Objects*. Optics Letters **29**, 183–185 (2004).

[45] J. Goodman. *Introduction to Fourier Optics*. McGraw-Hill Physical and Quantum Electronics Series. W. H. Freeman, 2005.

[46] T. Latychevskaia. *Lateral and Axial Resolution Criteria in Incoherent and Coherent Optics and Holography, near- and Far-Field Regimes*. Applied Optics **58**, 3597–3603 (2019).

[47] J. van Rooij and J. Kalkman. *Sub-Millimeter Depth-Resolved Digital Holography*. Applied Optics **56**, 7286–7293 (2017).

[48] M. Matrecano, M. Paturzo and P. Ferraro. *Extended Focus Imaging in Digital Holographic Microscopy: A Review*. Optical Engineering **53**, 112317 (2014).

[49] G. Nehmetallah and P. P. Banerjee. *Applications of Digital and Analog Holography in Three-Dimensional Imaging*. Advances in Optics and Photonics **4**, 472–553 (2012).

[50] M. Fratz, T. Seyler, A. Bertz and D. Carl. *Digital Holography in Production: An Overview*. Light: Advanced Manufacturing **2**, 283–295 (2021).

[51] K. Wu, C.-C. Lee, N. J. Brock and B. Kimbrough. *Multilayer Thin-Film Inspection through Measurements of Reflection Coefficients*. Optics Letters **36**, 3269–3271 (2011).

[52] M. A. Herráez, D. R. Burton, M. J. Lalor and M. A. Gdeisat. *Fast Two-Dimensional Phase-Unwrapping Algorithm Based on Sorting by Reliability Following a Noncontinuous Path*. Applied Optics **41**, 7437–7444 (2002).

[53] Z. Zhao, H. Zhang, Z. Xiao, H. Du, Y. Zhuang, C. Fan and H. Zhao. *Robust 2D Phase Unwrapping Algorithm Based on the Transport of Intensity Equation*. Measurement Science and Technology **30**, 015201 (2018).

[54] S. Park, Y. Kim and I. Moon. *Automated Phase Unwrapping in Digital Holography with Deep Learning*. Biomedical Optics Express **12**, 7064–7081 (2021).

[55] M. Sun, K. Wang, Y. N. Mishra, S. Qiu and W. Heidrich. *Space-Time Fourier Ptychography for in Vivo Quantitative Phase Imaging*. Optica **11**, 1250–1260 (2024).

[56] A. Pelekanidis, K. S. E. Eikema and S. Witte. *Far-Field Optical Propagators with User-Defined Object-Plane Pixel Size for Ptychography*. Optics Continuum **4**, 804–825 (2025).

2

LENSLESS SINGLE-SHOT DUAL-WAVELENGTH DIGITAL HOLOGRAPHY FOR INDUSTRIAL METROLOGY

We demonstrate lensless single-shot dual-wavelength digital holography for high-speed 3D imaging in industrial inspection. Single-shot measurement is realized by combining off-axis digital holography and spatial frequency multiplexing of the two wavelengths on the detector. The system has 9.1 µm lateral resolution and a 50 µm unambiguous depth range. We determine the theoretical accuracy of off-axis dual-wavelength phase reconstruction for the case of shot-noise limited detection. Experimental results show good agreement with the proposed model. The system is applied to industrial metrology of calibrated test samples and chip manufacturing.

This chapter has been published in Applied Optics **63**, 4427-4434 (2024) [1].

2.1. Introduction

Industrial inspection of manufactured components is critical in ensuring product quality and performance. In the measurement of component structure, e.g., analysis of surface defects, assessment of dimensional accuracy and assembly quality, optical inspection plays a vital role [2–4]. Challenges in this field are obtaining high spatial resolution, large field of view, rapid measurement, and 3D imaging capability. 3D imaging extracts depth information thereby enabling the detection of defects that may be overlooked when relying solely on 2D images. Common optical 3D imaging methods include stereo vision, fringe projection profilometry, and optical coherence tomography. Yet their limitation lies in their limited resolution, need for scanning in time or the need for multiple cameras. In mass production industries, such as semiconductor production and assembly, high-speed imaging is important for real-time monitoring of product quality, which is challenging with current imaging modalities. Digital holography [5–8] is a technique that enables full-field depth-resolved single-shot measurement with a field of view and resolution comparable to classical microscopes, thereby meeting the demands of many industrial inspections.

Digital holography (DH) can simultaneously retrieve the amplitude and phase of the optical field and reconstruct the 3D shape of the object from it [9–11]. In industrial applications DH primarily operates in reflection mode where the phase change of non-transparent objects is caused by the height variation of the surface. Many studies [12–14] have shown the efficacy of DH in reconstructing various industrial components, including those that are reflective or matte, or have steep edges, demonstrating its robustness and wide applicability. Another notable advantage of DH is its ability of wavefront reconstruction, enabling numerical propagation for refocusing to any plane of interest. Unlike classical microscopes, DH does not rely on lenses for ”imaging” [15], thereby avoiding lens aberrations, but also making the setup compact and circumventing cumbersome mechanical focusing operations.

A major limitation of the classical DH is that it cannot retrieve an unambiguous depth when the optical path difference is larger than the illumination wavelength due to the ”2π ambiguity”. This can be solved using phase unwrapping algorithms. However, this works well only for a gradual and continuous changing sample surface [16–19]. Dual-wavelength DH (DWDH) [20–22] alleviates the phase wrapping problem by employing measurements at two wavelengths and subtracting the phases of their fields to get the beat phase corresponding to the synthetic wavelength. The synthetic wavelength is larger than the illumination wavelength and defines the ”new” unambiguous measurement range. The closer the wavelengths of the two lasers are, the larger the synthetic wavelength will be. For example, Abeywickrema et al. [23] achieved a centimeter-scale measurement range with an acousto-optic modulator by sequentially measuring holograms at two wavelengths. For high speed acquisition the holograms at the two wavelengths also can be measured in a single-shot measurement, by using spectral multiplexing with a Bayer mosaic color camera [24–26] or by combining an off-axis configuration with spatial frequency multiplexing [27], the latter of which is widely adopted due to

better image resolution and more economical monochrome cameras. For instance, Fratz et al. [28, 29] designed a multi-wavelength DH system with a synthetic wavelength ranging up to 1 mm that was successfully applied for detection in a precision turning plant. Piniard et al. [30] reported a dual-wavelength system for in situ real-time investigation of the melt pool morphology. Many papers [31–34] have also reported improvements to off-axis-based DWDH to develop applications in different fields. However, all the aforementioned papers use lenses for imaging, and thus, the lensless imaging capability of DH, as well as the advantages it brings in making systems more compact, have not been fully exploited.

Even though the wavelength separation between the two wavelengths determines the unambiguous measurement range, the accuracy in determining the surface height depends on the accuracy of the phase estimation at the synthetic wavelength [35–37]. The phase estimation is influenced by noise from environmental vibrations, laser power fluctuations, and shot noise. Additionally, for rough surfaces, the diffuse scattering introduces additional phase noise and decoherence of the optical fields, further impacting phase estimation. Piniard et al. [38] investigated the impact of noise in DWDH, however their study focused on the effect of surface roughness on phase measurements, in which case the scattering decorrelation noise was the dominant factor. A few studies [39–41] indicate that, after excluding environmental and sample factors, shot noise is the ultimate factor affecting phase accuracy in DH, and its impact on the phase measurement has been extensively examined, albeit limited to the single-wavelength scenario.

Realizing the large and steep height variations on object surfaces during industrial inspections and the need for fast, accurate, and large-depth range 3D imaging for integrated circuits (IC) process control, we propose a high phase accuracy, single-shot DWDH system. The adoption of a lensless configuration makes the setup compact and easy to integrate into existing industrial equipment. We analyse the imaging field of view and spatial resolution in the lensless configuration and their limit factors. Additionally, we extend the single-wavelength DH shot-noise model proposed by Chen [40] to the DWDH scenario. Based on a theoretical analysis of our extended noise model and comparison with experimental results, we demonstrate the feasibility of our model and show that the shot-noise limited phase sensitivity is approached. We show the successful application of single-shot large depth range imaging of IC micro-structures and chip tilt detection.

2.2. METHODS

2.2.1. LENSLESS DIGITAL HOLOGRAPHY SETUP

The setup of the lensless single-shot DWDH is illustrated in Figure 2.1(a). A He-Ne laser (HRS015B, Thorlabs) with wavelength $\lambda_1 = 633$ nm and a laser diode (CPS650F, Thorlabs) with wavelength $\lambda_2 = 637$ nm are used as light sources and yield a synthetic wavelength $\Lambda = \lambda_1\lambda_2/|\lambda_1 - \lambda_2| \approx 100$ µm. Both beams first pass through a beam expander to increase the beam size to cover the entire sample. The beam expander for λ_1 is composed of two positive lenses (LA1805-A and LA1509-A, Thorlabs) and a pinhole (P30K, Thorlabs) and for λ_2 is composed of

two lenses (LA1131-A and LA1509-A, Thorlabs) and a pinhole (P25K, Thorlabs). The purpose of the pinhole is to filter out high spatial frequency noise from the laser output, producing a clean Gaussian-shaped illumination. The expanded beam for λ_i, with $i = 1, 2$ is then split into two fields with a cube beam splitter (BS013, Thorlabs). In one arm, the field illuminates the object, and its reflected field is redirected by a pellicle beam splitter (BP250, Thorlabs) and captured by the camera, this is the object field O_i. The object field has an amplitude $|O_i|$ and phase φ_i. In the reference arm, the field R_i, reaches the camera after reflection by a mirror and transmission through the pellicle beam splitter. The interference of these two fields produces an interference pattern (hologram). The reference beam R_i is an inclined plane wave, with spatial frequencies $f_{x,i}$ and $f_{y,i}$ along the x and y direction, respectively. The subscript $i = 1, 2$ indicates the two wavelengths.

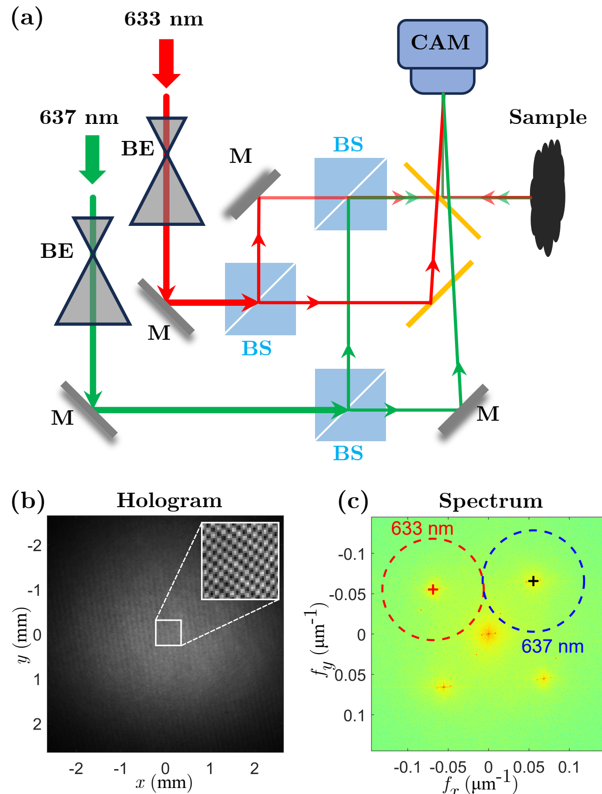

Figure 2.1: (a) Schematic overview of the lensless single-shot DWDH setup. BE, beam expander; M, mirror; BS, beam splitter, CAM, camera. (b) An acquired dual-wavelength hologram. (c) The power spectrum of the hologram of (b).

In our setup, the two illumination fields propagate coaxially to the sample along the direction of the optical axis while the two reference beams approach the camera

at different angles giving rise to different spatial frequencies. Through variation of the incident angle, the interference fringes for λ_1 and λ_2 are orientated along the two diagonals of the sensor, leading to their spectra (Fourier transform of the hologram) to appear at a frequency axis orthogonal to the direction of their fringes. Positioned at an approximate distance of 70 mm from the sample holder, a monochrome 8-bits camera (MC124MG-SY-UB, XIMEA) with dimensions of 4112 × 3008 pixels and a pixel size $\Delta x = \Delta y = 3.45$ µm is employed. The numerical aperture (NA) for a lensless system is equal to the half open angle from the sample to the sensor, i.e., $\mathrm{NA} = \mathrm{W_{cam}}/2d$, where $\mathrm{W_{cam}}$ is the width of the camera sensor, and d is the distance between the object and camera. To accommodate the beam size, only 1536 × 1536 pixels of the sensor area (5.3 × 5.3 mm^2) were used in our measurements, resulting in an NA = 0.035 and a field of view (FOV) of 28.09 mm^2. The exposure time for the hologram in our measurements was around 60 µs and varied depending on the samples to be measured. Because the two fields from the two wavelengths are not coherent with each other, the intensity of the dual-wavelength hologram I_{DW} captured by the camera is the sum of the two single wavelength holograms [31]:

$$
\begin{aligned}
I_{DW} &= |O_1|^2 + |R_1|^2 + O_1 R_1^* + O_1^* R_1 \\
&\quad + |O_2|^2 + |R_2|^2 + O_2 R_2^* + O_2^* R_2 \\
&= |O_1|^2 + |R_1|^2 + |O_2|^2 + |R_2|^2 \\
&\quad + 2|O_1||R_1| \cos(\varphi_1 - f_{x,1}x - f_{y,1}y) \\
&\quad + 2|O_2||R_2| \cos(\varphi_2 - f_{x,2}x - f_{y,2}y)\,,
\end{aligned}
\tag{2.1}
$$

where all fields are functions of spatial coordinates x and y. Figure 2.1(b) and (c) show an example of an acquired hologram and its corresponding spectrum. The inset in Figure 2.1(b) illustrates a chessboard-like interference pattern caused by the cross-overlapping of the two interference fringes. In contrast, Figure 2.1(c) presents well-separated spectra, thanks to the different spatial frequencies carried by the two reference beams. The cross marker indicates the center position of the sideband $(O_i R_i^*)$. According to Fourier optics, the cut-off frequency of the sideband is $f_{c,i} = \mathrm{NA}/\lambda_i = \mathrm{W_{cam}}/(2\lambda_i d)$. The circles indicate the spectral range that will be truncated during the subsequent reconstruction and is set to be slightly broader than the bandwidth of the sideband $f_{c,i}$.

2.2.2. Object field reconstruction

The Fourier transform-based filtering algorithm is an efficient and straightforward reconstruction method for off-axis DH and can also be applied to DWDH. First, the hologram is Fourier transformed to determine its power spectrum, as depicted in Figure 2.1(c), where the spectra of the real/virtual image terms for the two wavelengths are cross-diagonally distributed due to off-axis illumination. Second, two band-pass masks are created to selectively filter the spectra of the two fields $(O_i R_i^*)$. The location of the mask center is determined by the coordinates of the maximum value of the sideband. The selection of the mask radius, as described

in the previous section, needs to be larger than the cut-off frequency $f_{c,i}$. The cut-off frequency $f_{c,i}$ can only be approximated at first, by reasonably estimating the distance between sample and camera d. After obtaining the precise distance by refocusing, $f_{c,i}$ can be updated once again. We further multiply the estimated mask radius $f_{c,i}$ by 1.1 to avoid loss of spatial resolution. Third, the filtered spectrum undergoes an inverse Fourier transform, followed by compensation for the phase slope of the reference field through multiplication with a digitally generated reference beam R_i^{dig} based on the centroid of the off-axis term [30] to determine the spatial frequency of R_i^{dig}. Finally, we perform a linear phase fitting and subtraction to reduce the phase residue. At this point, the object field, which is the field diffracted from the object onto the detector, is obtained. The undiffracted field in the sample plane is obtained through back propagation using the angular spectrum method [42]. The propagation distance to the sample is determined by searching for the distance at which the image edges are sharpest [12]. It is worth pointing out that imperfection in laser alignment or inaccuracy in slope phase compensation may result in a slightly offset between the two on-focus images. In such cases, image registration is recommended. Finally, the phase map φ_i is retrieved by extracting the imaginary and real parts of the resulting complex field and then calculating the arctangent of the ratio. The process for phase retrieval at the two wavelengths in off-axis dual-wavelength digital holography can be summarized as [31]

$$\varphi_i = \text{angle}\left(\mathcal{F}^{-1}\{\mathcal{F}\{I_{DW}\} \cdot \text{Mask}_i\} \cdot R_i^{\text{dig}}\right) . \tag{2.2}$$

Note that both phase maps φ_i are wrapped which prevents extracting the height map of the sample correctly from the each individual phase map. This issue can be resolved by calculating the so-called beat phase Φ in dual-wavelength digital holography as [31]

$$\Phi = \varphi_1 - \varphi_2 = 2\pi\text{OPL}\left(\frac{1}{\lambda_1} - \frac{1}{\lambda_2}\right) = 2\pi\frac{\text{OPL}}{\Lambda} , \tag{2.3}$$

where OPL denotes the optical path length, which is twice the height map of the sample due to the setup working in reflection mode. Examination of Eq. (2.3) reveals that the phase Φ is wrapped only when OPL$>\Lambda$. In contrast, for single-wavelength DH, the phase φ_i becomes wrapped once OPL$>\lambda_i$, which explains why DWDH can unambiguously measure objects with substantial height differences without the need for phase unwrapping algorithms. The data processing time for the whole process of beat phase estimation is around 1.2 seconds for a 1536×1536 pixel hologram (using an Intel(R) Xeon(R) W-2223 CPU @ 3.60GHz). Obviously, the closer the two wavelengths, the larger the synthetic wavelength Λ, allowing for larger height difference measurement. However, as the two wavelengths draw closer, the impact of laser source bandwidth and wavelength drift becomes more significant. Since the height accuracy scales with Λ in Eq. (2.3), a larger synthetic wavelength at the same single wavelength phase sensitivity φ_i leads to a reduction in height estimation accuracy. Hence, it is of paramount importance to achieve the highest phase sensitivity possible.

2.2.3. THEORETICAL ACCURACY OF DWDH PHASE ESTIMATION

The accuracy of phase measurement defines the height accuracy and can be quantified by the standard deviation of the phase reconstruction $\sigma(\varphi)$. This metric not only reflects the minimal detectable phase change but also describes the spread in phase measurements over time. In practice, surface roughness, technical noises, and environment will influence the accuracy of phase measurement [38–41]. For polished surface, the impact of roughness could be irrelevant compared to other noise sources [38, 41]. Maintaining stable experimental conditions and using a high-performance camera can effectively decreases many types of noise, such as dark-current and background noise. However, shot-noise is the ultimately limiting factor and sets a baseline for the phase accuracy [39, 40]. Chen et al. [40] theoretically studied the phase sensitivity for single-wavelength off-axis DH and derived an analytical expression for the best achievable phase accuracy estimation under shot-noise limited detection

$$\sigma_\varphi = \sqrt{\frac{|O|^2+|R|^2}{2g|O|^2|R|^2}\frac{S}{MN}}, \tag{2.4}$$

where the intensities are measured in photoelectron counts on the camera, 'g' is the camera gain, and S/MN denotes the ratio of the filter area S to the entire Fourier area MN. The ratio of the DC term of the hologram over the amplitude of the interference is the reciprocal of the fringe visibility. It is worth noting that the accuracy $\sigma(\varphi_i)$ is a functions of x and y as a result of the non-uniformity of the reference and sample field. The camera gain g, with unit of $\mathrm{e}^-/\mathrm{ADU}$, is calibrated using the mean-variance fitting method [43], serving as the conversion factor between the number of photoelectrons and the analog-to-digital unit (ADU) reading of the camera. A higher g leads to improved phase accuracy (decreasing phase standard deviation). This is consistent with physical intuition: with a larger camera gain at the same camera readout, a pixel contains more photoelectrons; therefore, the impact of shot noise, which follow a Poisson distribution, on the signal decreases. The calibrated gain of the camera we used is $g = 9.6 \pm 0.15$.

We apply the phase accuracy model Chen et al. [40] to off-axis DWDH. First, due to the non coherence of the two independent laser sources and the linear detection efficiency, the dual-wavelength hologram of Eq. (2.1) can be considered as a superposition of two individual single wavelength holograms. Second, as previously discussed, the respective amplitudes $|O_i|$ for each wavelength can be determined utilizing different filters via Fourier filtering. Therefore, following similar derivation steps, we find that the phase accuracy σ_{φ_i} reconstructed from a dual-wavelength hologram under the condition of shot-noise limited detection is

$$\sigma_{\varphi_i} = \sqrt{\frac{|O_1|^2+|R_1|^2+|O_2|^2+|R_2|^2}{2g|O_i|^2|R_i|^2}\frac{S}{MN}}. \tag{2.5}$$

This expression shares a close resemblance with Eq. (2.4). The difference lies in the DC term: in the dual-wavelength case, the DC term is the summation of the two DC terms from the two individual single-wavelength. To avoid detector

saturation, the maximum value of $|O_i||R_i|$ in dual-wavelength needs to be smaller than in the single-wavelength case. Consequently, when using the same hardware and reconstruction algorithm, a comparison of Eq. (2.4) and Eq. (2.5) suggests that, even if the phase measurement accuracy at an individual wavelength is the focus of interest, the phase accuracy obtained from a dual-wavelength hologram is inferior to that from a single-wavelength hologram. For DWDH with equal power in the two wavelengths, a total power of the illumination equal to that for the single-wavelength case, and a perfectly balanced interferometer, the phase accuracy at individual wavelengths is a factor $\sqrt{2}$ worse than the result from a single-wavelength DH measurement.

For the beat phase Φ, which is given by the subtraction of two independent phase maps, as expressed in Eq. (2.3), its variance equals the sum of the variances of the other two phases, i.e.,

$$\begin{aligned}\sigma_{\Phi}^2 &= \sigma_{\varphi_1}^2 + \sigma_{\varphi_2}^2 \\ &= \frac{|O_1|^2 + |R_1|^2 + |O_2|^2 + |R_2|^2}{2g} \frac{S}{MN} \times \left[\frac{1}{|O_1|^2 |R_1|^2} + \frac{1}{|O_2|^2 |R_2|^2} \right].\end{aligned} \tag{2.6}$$

This can be considered the shot noise limited phase accuracy for DWDH and can be converted to height accuracy via Eq. (2.3). Eqs. (2.5) and (2.6) make it possible to quantify and evaluate the phase accuracy of a DWDH setup, solely from one hologram.

2.3. RESULTS

2.3.1. LATERAL RESOLUTION AND FIELD OF VIEW

In conventional optical microscopy, there is generally a trade-off between the lateral field of view (FOV) and image resolution as the objective lens and tube lens are matched for a minimal aberration. While a high NA objective lens can enhance the lateral resolution, it comes at the expense of a smaller lateral FOV, and vice versa. In a lensless DH setup with plane wave illumination, the imaging FOV is equal to the sensor size, and the lateral resolution is determined by both the NA of the system and the pixel size of the sensor Δx. According to the Abbe criteria, the theoretical resolution can be calculated using the formula $r_A = \lambda/2\text{NA}$. Decreasing the distance from the sample to the sensor or increasing the sensor size can increase the NA of the system and improve resolution. However, it ultimately is limited by the finite pixel size, because the image is discretely sampled by the sensor in lensless DH. This usually does not pose a big problem in classical microscopes, because in magnified images the point spread function is wider than the pixel size.

The experimentally achievable resolution and FOV were determined by imaging a USAF resolution target, see Figure 2.2. Figure 2.2(a) and (b) show the acquired 5×5 mm^2 hologram and the corresponding power spectrum, respectively. The width of the spectrum, also referred to as the sensor bandwidth, depends on the pixel size Δx and is equal to $1/\Delta x$. According to the Nyquist theorem, only signals with a spatial frequency within the sensor bandwidth can be accurately sampled

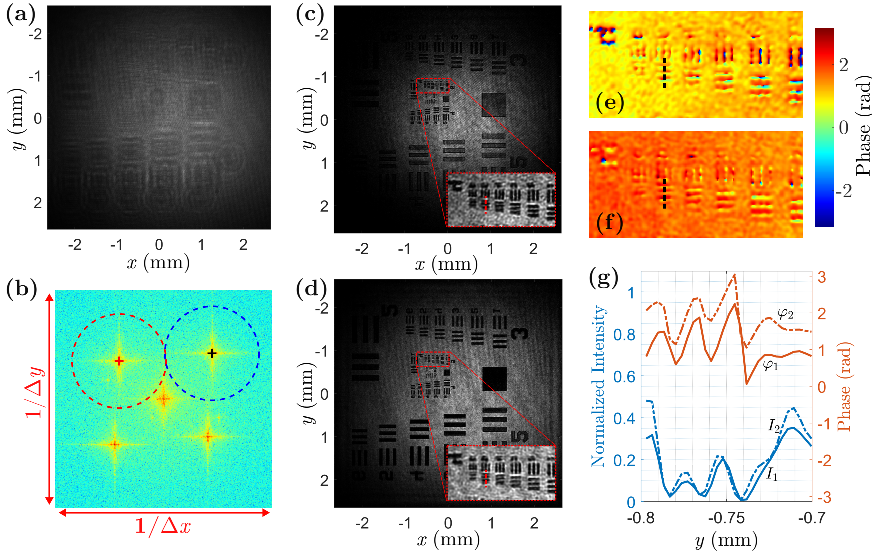

Figure 2.2: DWDH measurement on USAF resolution target. (a) The acquired dual-wavelength hologram. (b) The corresponding power spectrum. The width is equal to $1/\Delta x$. (c-d) Reconstructed intensity maps for λ_1 and λ_2, where the inset represents the zoomed-in image of the selected areas. (e-f) The respective phase map of the selected areas in (c) and (d). (g) Intensity and phase profile curves of element 5-5 of the USAF target.

and retrieved. Since the spectra of the fields $O_i R_i^*$ and their complex conjugates are symmetrically distributed and have the same bandwidth, the optimal spectrum arrangement in DWDH should be a diagonal distribution with the two wavelengths along different diagonals, as shown in Figure 2.2(b). The dashed circle in the figure indicates the bandwidth of the sideband, which is smaller than the sensor bandwidth, leading to the achievable resolution given by the Abbe diffraction limit. During the data processing, the distance from the sample to the sensor was found to be 76.11 mm. Consequently, $r_A \approx 9.1$ µm was the best achievable DWDH resolution, as the resolution for the two wavelengths are almost equal.

The reconstructed intensities for λ_1 and λ_2 are shown in Figure 2.2(c) and (d), respectively. The insets displays zoomed-in images of the red dashed box area, from which we can see that the smallest distinguishable pattern is element 5-5 which has 50.8 line pairs per millimeter. Also note that the FOV of the images is 5×5 mm^2, the same dimensions as the hologram in Figure 2.2(a). However, only part of the FOV is useful as the beam intensity is diminished at the edges. Figure 2.2(e) and (f) shows the respective phase maps of the zoomed-in image for λ_1 and λ_2, respectively. Figure 2.2(g) shows both the intensity and phase profiles of element 5-5 along the dashed line in Figure 2.2(c-f). We can observe that this set of patterns just can be resolved for both intensity and phase. Therefore, it can

be concluded that the spatial resolution of the setup is better than 9.84 µm, a value close to the theoretical resolution of $r_A \approx 9.1$ µm.

2.3.2. Phase accuracy

The phase measurement accuracy for DWDH was experimentally quantified and compared with the theoretical model. A silver mirror was used as the object to avoid the influence of the scattering decorrelation noise on the phase that stems from the surface roughness. The experimental method for measuring the phase accuracy is as follows: first, we took a series of holograms at 40 ms intervals during 10 seconds. Second, the phase maps from each hologram were reconstructed separately for the two wavelengths and the synthetic wavelength by using Eq. (2.2) and Eq. (2.3), that is φ_1, φ_2, and Φ. Finally, the standard deviation σ_{exp} of the phase variation at every location was calculated from the time series. Figure 2.3(a) shows the three phase maps for λ_1, λ_2, and Λ reconstructed from one of the captured holograms. The phases are constant for the mirror object. Figure 2.3(b) shows the variation of the phase at one point (marked with a red cross) in (a) on each reconstruction, and the statistical distribution is shown in the histogram. As can be seen, due to noise in the experiment, there are temporal fluctuations in the phase. We can obtain the phase measurement accuracy σ_{exp} at the indicated point, which are 15.8, 19.7 and 24.7 mrad for λ_1, λ_2, and Λ, respectively.

The spatially resolved phase measurement accuracy maps are illustrated in Figure 2.4. Figure 2.4(a) shows the experimental phase accuracy for λ_1, λ_2, and Λ and Figure 2.4(b) shows the theoretical phase accuracy calculated with Eqs. (2.5) and (2.6) All parameters required to obtain the theoretical accuracy can be computed from a single captured hologram. A quantitative comparison between the theoretical and experimental accuracy is presented in Figure 2.4(c), each plot corresponds to the comparison along the red dashed lines in (a) and (b). From Figure 2.4(c), it can be seen that higher phase accuracy appears at the center of the detector area for both the experimental and theoretical accuracy. This characteristic can be explained by the Gaussian illumination profile, which results in a higher intensity (more photons) at the center and thus less noise. Furthermore, the comparison reveals that the experimental accuracy is basically lower bounded by the theoretical accuracy. The theoretical accuracy is based on shot noise only; however, the severe fluctuations observed in the experimental results imply that other factors such as readout noise, pixel inconsistency, and sources instability also affect our measurements to some extent.

2.3.3. Application to industrial inspection

Several experiments were conducted to demonstrate the applicability of our setup for industrial inspection. Figure 2.5 shows quantitative 3D reconstruction of a metal workpiece (manufactured by Rubert & Co Ltd, product type 515) which consists of six engraved grooves on its surface (with depths of 1, 5, 10, 50, 100, 1000 µm). Figure 2.5(a) is the acquired dual-wavelength hologram, which is a superposition of two interference patterns. The inset in Figure 2.5(a) depicts the

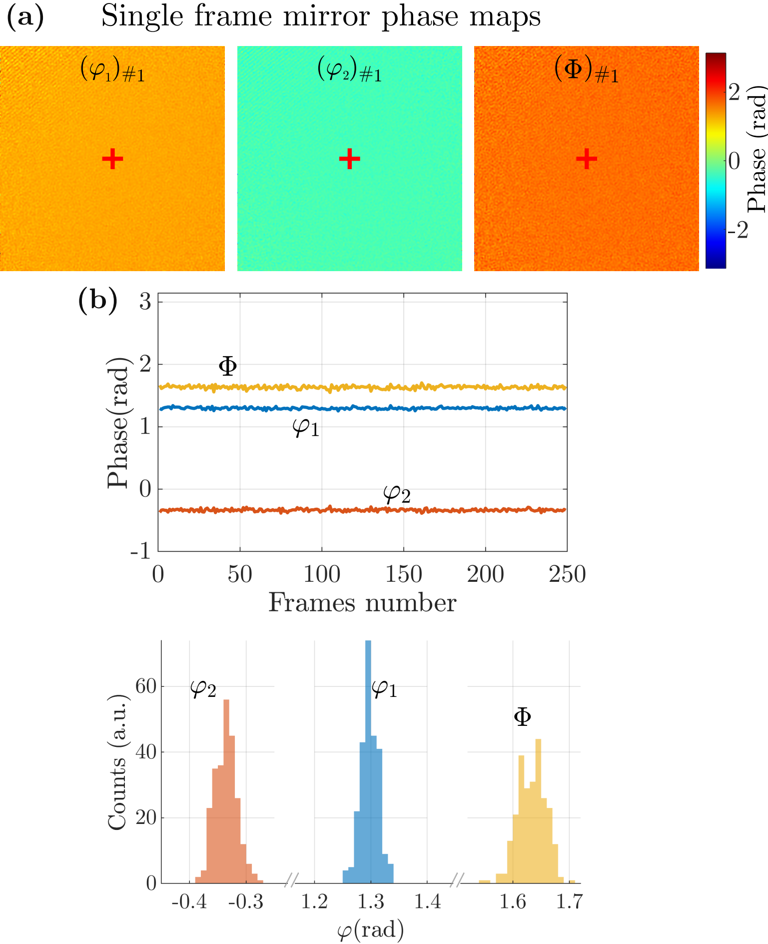

Figure 2.3: (a) DWDH reconstructed phase maps of a mirror sample for λ_1, λ_2, and Λ. (b) The phase change over time for the three phases at the selected point in (a). The histogram on the right shows the corresponding statistical distribution.

power spectrum density distribution of the hologram. The spectrum shows that the spectra for λ_1 and λ_2 are diagonally distributed and well separated. Figure 2.5(b) and (c) show the reconstructed intensity and phase map for λ_1 (the result for λ_2 has a similar appearance). The phase map, Figure 2.5(c), displays a wrapped phase according to spherical waves, which is caused by the slight concavity on the workpiece surface. Nevertheless, the presence of the grooves is still discernible, as the groove depth introduces additional phase delays, resulting in discontinuities in the phase distribution around the groove edges.

The beat phase map Φ, computed via Eq. (2.3) and after subtraction of a linear

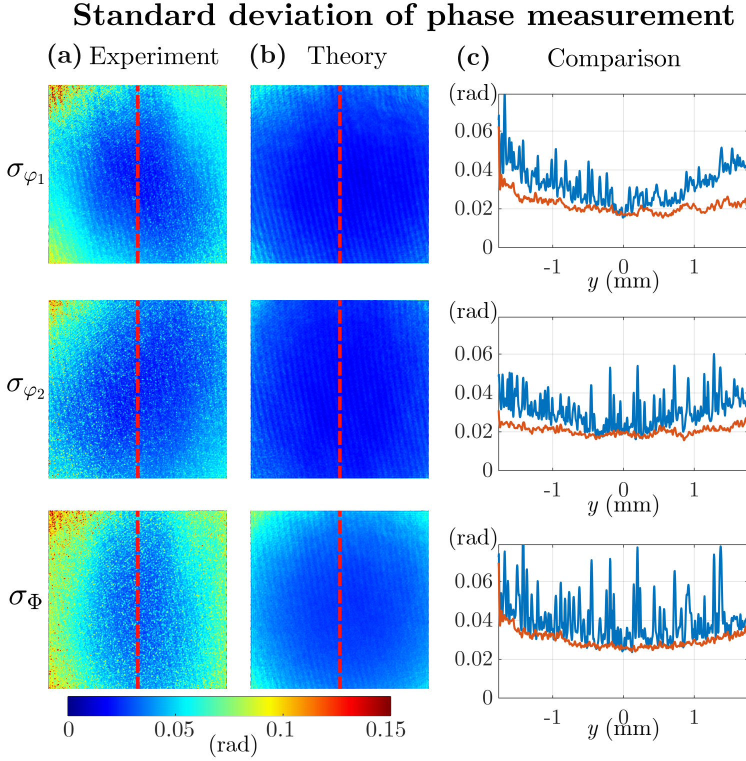

Figure 2.4: Experimental (a) and theoretical (b) DWDH phase accuracy comparison for λ_1, λ_2, and Λ. (c) Comparison along the red lines in (a) and (b), where the blue line is the experimental data and the red line is the theoretical prediction.

phase tilt, is illustrated in Figure 2.5(d). It is evident from the figure that the issue of phase wrapping has been significantly alleviated, and that the grooves are well visible due to their difference in phase value with respect to the surface. The phase values in regions with insufficient intensity have been removed and replaced with NAN (not a number). This is necessary, as calculating the phase in these areas results in an ill-defined phase due to the denominator of the arctangent being zero or close to zero. These regions occur around the periphery of the image and on either side of the grooves. The former is attributed to the non-uniform illumination of the Gaussian beam, while the latter is because the grooves have very vertical side walls, making it challenging to obtain reflective light from these areas. Figure 2.5(e) demonstrates a 3D topography map of the region highlighted in red in Figure 2.5(d) where the phase has been converted to height distribution and the linear phase has been subtracted. The 3D map clearly distinguishes the presence of two grooves with nominal depths of 5 µm and 10 µm. The red line depicted in Figure 2.5(e) denotes the projection of the reconstructed height

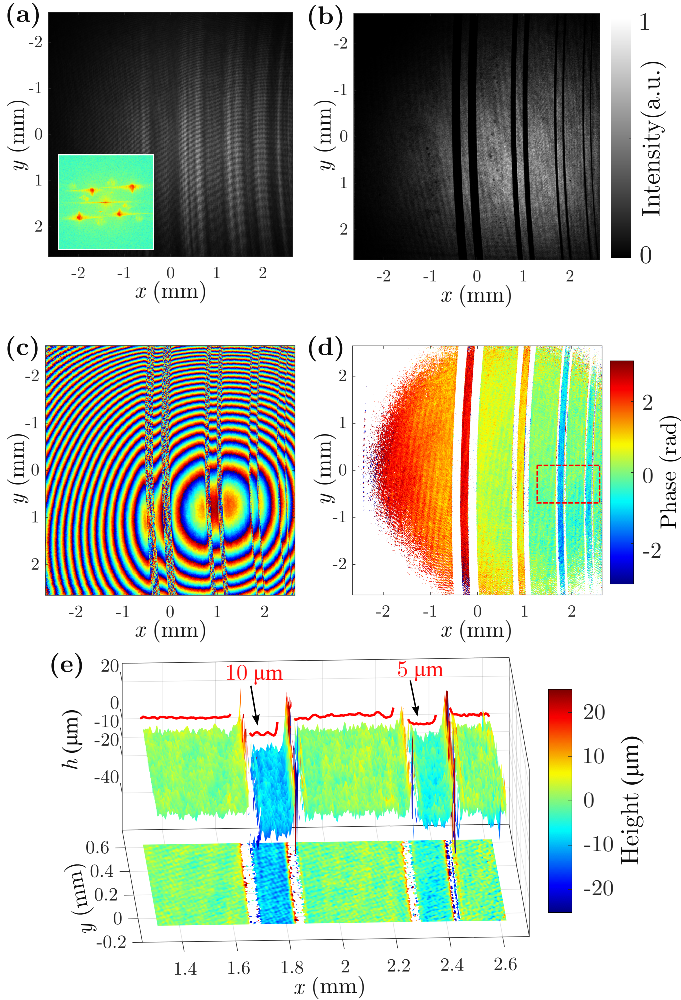

Figure 2.5: DWDH measurement on a metal workpiece. (a) The obtained dual-wavelength hologram, where the inset shows its spectrum. (b-c) Reconstructed intensity and wrapped phase for λ_1. (d) Beat phase map computed by Eq. (2.3) after tilt compensation and ignoring low intensity areas. (e) 3D topography map of the selected area in (d).

distribution along the y-axis, confirming that the depths of the identified grooves are in line with the expected nominal values. The manufacturer stated nominal bottom width of the 10 µm groove measures 134 µm and that of the 5 µm measures 111 µm. These two dimensions measured from our results are 132.6 ± 3.9 and 119.4 ± 7.5 µm respectively. Given that the discretization interval of the image equals the pixel size (3.45 µm), the deviation between the measurement and the

nominal value is reasonable.

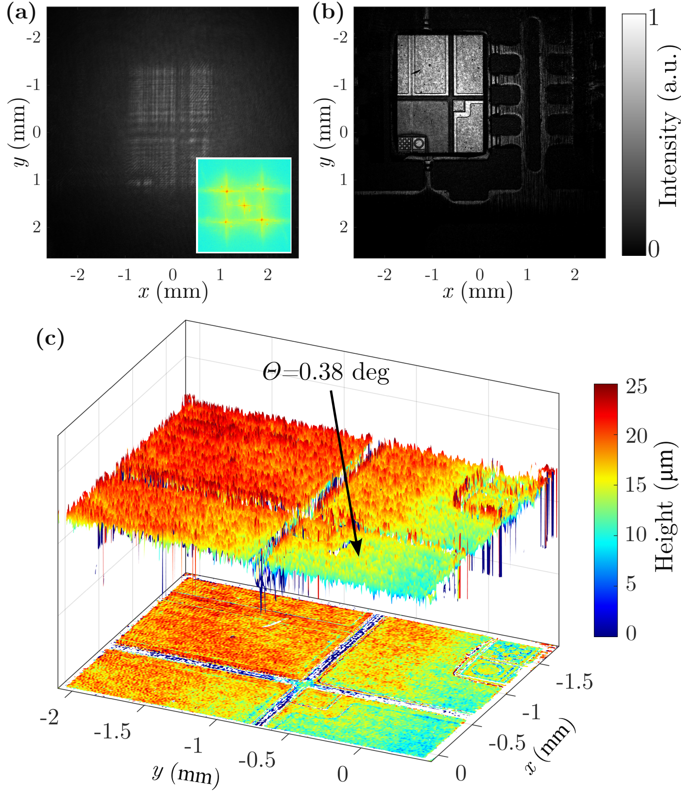

Figure 2.6: DWDH application demonstration on chip tilt detection. (a) The captured dual-wavelength hologram and its spectrum. (b) Sum of the reconstructed intensities for λ_1 and λ_2. (c) Calculated height map and 3D topography map of the chip obtained from the beat phase. The tilt angle of the chip surface is indicated.

Figure 2.6 demonstrates the application of DWDH to industrial 3D chip inspection to determine the tilt of a die on a substrate. This tilt primarily results from the shrinkage and expansion of the glue solidification during the adhesive bonding process. The recorded hologram and its corresponding spectrum are illustrated in Figure 2.6(a) and the inset therein. Figure 2.6(b) shows the reconstructed intensity at the surface of the chip, which is a superposition of the intensities for λ_1 and λ_2. While the intensity map provides many details about the chips, it fails to discern the presence of any tilt of the die. Furthermore, since the amount of tilt is minimal, the focus variance does not noticeably vary. However, the phase map clearly highlights this tilt as it appears in the form of distinctly increasing phase values. Figure 2.6(c) shows the height calculated from the two wrapped phases with the help of Eq. (2.3), wherein phases with excessively low

intensities were omitted for better visibility. The tilt of the chip can be seen as the color variation from upper left to bottom right. After 3D plane fitting operation, the tilt angle θ relative to the $x - y$ plane is quantified as 0.38 ± 0.006 degrees.

2.4. DISCUSSION

We demonstrated diffraction limited lateral resolution DWDH. In the lensless configuration, the achievable resolution for two wavelengths using only a single detector and single frame acquisition is determined by the numerical aperture, but also by the correct choice of off-axis angle and pixel size Δx. The off-axis angle translates the spectrum of the sideband in the frequency domain, and the pixel size Δx determines the sensor bandwidth. Achieving the Abbe theoretical limit r_A is only possible when the sensor bandwidth covers the entire sideband. If the sideband surpasses the sensor bandwidth, which generally happens when the off-axis angle or system numerical aperture is too large, the achievable resolution will be worse than r_A. It is also worth mentioning that the spatial resolution in coherent imaging depends on the phase difference between two points [42]. Therefore, in real-world measurements of 3D objects, the achievable resolution can either be better or worse than the Abbe diffraction limit.

Although the DWDH FOV is given by the sensor size, in our experiment the useful FOV is more limited by the illumination beams that have a Gaussian light distribution that does not illuminate the entire FOV uniformly. To address this issue the illumination beam can be made more uniform with a flat-top beam collimator, which could be added after the beam expander.

Our paper investigates phase accuracy under conditions where shot noise is dominant factor. For a polished mirror, the surface roughness is sufficiently small (less than 1 nm) that decorrelation noise has very little influence. However, when the specimen has a rough surface, diffuse reflection can lead to speckle decorrelation, which deteriorates the phase measurement. Therefore, for phase accuracy measurements of rough objects, we recommend using the noise model proposed by Piniard et al. [38] along with the approach outlined in this paper to achieve a more precise prediction of phase accuracy.

The speed of the DWDH imaging proposed here is limited by two factors. First, the acquisition time of the camera, which typically ranged in the order of hundreds of microseconds, varying slightly depending on the reflectivity of the object. Notably, a single measurement proved sufficient to complete the entire imaging process. The imaging speed can be further enhanced by taking a higher speed camera and more powerful light sources. Second, the data processing time is a few seconds for any of our experiments. We anticipate that faster data processing can be achieved with code optimization or conversion to a dedicated pre-compiled programming language.

In this paper, we only show one application case, nevertheless, we believe that this method will have multiple untapped industrial applications.

2.5. Conclusion

In this paper, we demonstrate a lensless single-shot DWDH system designed to address challenges encountered in modern industrial inspection. The dual-wavelength approach effectively extends the unambiguous measurement range to 50 micrometers in height. Combination off-axis and spatial frequency multiplexing offers a feasible solution for achieving single-shot dual-wavelength acquisition. We derive general expressions for quantifying and evaluating the phase accuracy for a DWDH setup from a single hologram under the condition of shot-noise limited detection. Our experimental result shows a good agreement with our theoretical model. Also we demonstrate the capability of DWDH for 3D optical industrial inspection.

REFERENCES

[1] H. Shangguan, H. P. Urbach and J. Kalkman. *Lensless Single-Shot Dual-Wavelength Digital Holography for Industrial Metrology*. Applied Optics **63**, 4427–4434 (2024).

[2] T. Yoshizawa. *Handbook of Optical Metrology: Principles and Applications*. CRC Press, 2009.

[3] R. Leach. *Optical Measurement of Surface Topography*. Springer Berlin Heidelberg, 2011.

[4] S. Catalucci, A. Thompson, S. Piano, D. T. Branson and R. Leach. *Optical Metrology for Digital Manufacturing: A Review*. The International Journal of Advanced Manufacturing Technology **120**, 4271–4290 (2022).

[5] D. Gabor. *A New Microscopic Principle*. Nature **161**, 777–778 (1948).

[6] E. N. Leith and J. Upatnieks. *Reconstructed Wavefronts and Communication Theory*. J. Opt. Soc. Am. **52**, 1123–1130 (1962).

[7] E. Cuche, F. Bevilacqua and C. Depeursinge. *Digital Holography for Quantitative Phase-Contrast Imaging*. Optics Letters **24**, 291–293 (1999).

[8] B. Javidi, A. Carnicer, A. Anand, G. Barbastathis, W. Chen, P. Ferraro, J. W. Goodman, R. Horisaki, K. Khare, M. Kujawinska, R. A. Leitgeb, P. Marquet, T. Nomura, A. Ozcan, Y. Park, G. Pedrini, P. Picart, J. Rosen, G. Saavedra, N. T. Shaked, A. Stern, E. Tajahuerce, L. Tian, G. Wetzstein and M. Yamaguchi. *Roadmap on Digital Holography [Invited]*. Optics Express **29**, 35078–35118 (2021).

[9] W. Osten, A. Faridian, P. Gao, K. Körner, D. Naik, G. Pedrini, A. K. Singh, M. Takeda and M. Wilke. *Recent Advances in Digital Holography [Invited]*. Applied Optics **53**, G44–G63 (2014).

[10] J. Zhang, S. Dai, C. Ma, T. Xi, J. Di and J. Zhao. *A Review of Common-Path off-Axis Digital Holography: Towards High Stable Optical Instrument Manufacturing*. Light: Advanced Manufacturing **2**, 333–349 (2021).

[11] H. Zhou, M. M. R. Hussain and P. P. Banerjee. *A Review of the Dual-Wavelength Technique for Phase Imaging and 3D Topography*. Light: Advanced Manufacturing **3**, 314–334 (2022).

[12] J. van Rooij and J. Kalkman. *Sub-Millimeter Depth-Resolved Digital Holography*. Applied Optics **56**, 7286–7293 (2017).

[13] D. Carl, M. Fratz, M. Pfeifer, D. M. Giel and H. Höfler. *Multiwavelength Digital Holography with Autocalibration of Phase Shifts and Artificial Wavelengths*. Applied Optics **48**, H1–H8 (2009).

[14] T. Colomb, S. Krivec, H. Hutter, A. A. Akatay, N. Pavillon, F. Montfort, E. Cuche, J. Kühn, C. Depeursinge and Y. Emery. *Digital Holographic Reflectometry*. Optics Express **18**, 3719–3731 (2010).

[15] E. S. R. Fonseca, P. T. Fiadeiro, M. Pereira and A. Pinheiro. *Comparative Analysis of Autofocus Functions in Digital In-Line Phase-Shifting Holography*. Applied Optics **55**, 7663–7674 (2016).

[16] M. A. Herráez, D. R. Burton, M. J. Lalor and M. A. Gdeisat. *Fast Two-Dimensional Phase-Unwrapping Algorithm Based on Sorting by Reliability Following a Noncontinuous Path*. Applied Optics **41**, 7437–7444 (2002).

[17] H. S. Abdul-Rahman, M. A. Gdeisat, D. R. Burton, M. J. Lalor, F. Lilley and C. J. Moore. *Fast and Robust Three-Dimensional Best Path Phase Unwrapping Algorithm*. Applied Optics **46**, 6623–6635 (2007).

[18] Z. Zhao, H. Zhang, Z. Xiao, H. Du, Y. Zhuang, C. Fan and H. Zhao. *Robust 2D Phase Unwrapping Algorithm Based on the Transport of Intensity Equation*. Measurement Science and Technology **30**, 015201 (2018).

[19] S. Park, Y. Kim and I. Moon. *Automated Phase Unwrapping in Digital Holography with Deep Learning*. Biomedical Optics Express **12**, 7064–7081 (2021).

[20] C. Wagner, W. Osten and S. Seebacher. *Direct Shape Measurement by Digital Wavefront Reconstruction and Multi-Wavelength Contouring*. Optical Engineering **39**, 79–85 (2000).

[21] J. Gass, A. Dakoff and M. K. Kim. *Phase Imaging without 2π Ambiguity by Multiwavelength Digital Holography*. Optics Letters **28**, 1141–1143 (2003).

[22] M. K. Kim. *Phase Microscopy and Surface Profilometry by Digital Holography*. Light: Advanced Manufacturing **3**, 481–492 (2022).

[23] U. Abeywickrema, D. Beamer, P. Banerjee and T.-C. Poon. *Holographic Topography Using Acousto-Optically Generated Large Synthetic Wavelengths*. Practical Holography XXX: Materials and Applications **9771**, 69–75 (2016).

[24] X. Tian, X. Tu, J. Zhang, O. Spires, N. Brock, S. Pau and R. Liang. *Snapshot Multi-Wavelength Interference Microscope*. Optics Express **26**, 18279–18291 (2018).

[25] M. T. Rinehart, N. T. Shaked, N. J. Jenness, R. L. Clark and A. Wax. *Simultaneous Two-Wavelength Transmission Quantitative Phase Microscopy with a Color Camera*. Optics Letters **35**, 2612–2614 (2010).

[26] J. Min, B. Yao, P. Gao, R. Guo, B. Ma, J. Zheng, M. Lei, S. Yan, D. Dan, T. Duan, Y. Yang and T. Ye. *Dual-Wavelength Slightly off-Axis Digital Holographic Microscopy*. Applied Optics **51**, 191–196 (2012).

[27] N. T. Shaked, V. Micó, M. Trusiak, A. Kuś and S. K. Mirsky. *Off-Axis Digital Holographic Multiplexing for Rapid Wavefront Acquisition and Processing*. Advances in Optics and Photonics **12**, 556–611 (2020).

[28] M. Fratz, T. Beckmann, J. Anders, A. Bertz, M. Bayer, T. Gießler, C. Nemeth and D. Carl. *Inline Application of Digital Holography [Invited].* Applied Optics **58**, G120–G126 (2019).

[29] M. Fratz, T. Seyler, A. Bertz and D. Carl. *Digital Holography in Production: An Overview.* Light: Advanced Manufacturing **2**, 283–295 (2021).

[30] M. Piniard, B. Sorrente, G. Hug and P. Picart. *Melt Pool Monitoring in Laser Beam Melting with Two-Wavelength Holographic Imaging.* Light: Advanced Manufacturing **3**, 14–25 (2022).

[31] J. Kühn, T. Colomb, F. Montfort, F. Charrière, Y. Emery, E. Cuche, P. Marquet and C. Depeursinge. *Real-Time Dual-Wavelength Digital Holographic Microscopy with a Single Hologram Acquisition.* Optics Express **15**, 7231–7242 (2007).

[32] R. Guo and F. Wang. *Compact and Stable Real-Time Dual-Wavelength Digital Holographic Microscopy with a Long-Working Distance Objective.* Optics Express **25**, 24512–24520 (2017).

[33] A. Khmaladze, M. Kim and C.-M. Lo. *Phase Imaging of Cells by Simultaneous Dual-Wavelength Reflection Digital Holography.* Optics Express **16**, 10900–10911 (2008).

[34] Z. Wang, Z. Jiang and Y. Chen. *Single-Shot Dual-Wavelength Phase Reconstruction in off-Axis Digital Holography with Polarization-Multiplexing Transmission.* Applied Optics **55**, 6072–6078 (2016).

[35] J. Kühn, F. Charrière, T. Colomb, E. Cuche, F. Montfort, Y. Emery, P. Marquet and C. Depeursinge. *Axial Sub-Nanometer Accuracy in Digital Holographic Microscopy.* Measurement Science and Technology **19**, 074007 (2008).

[36] C. Remmersmann, S. Stürwald, B. Kemper, P. Langehanenberg and G. von Bally. *Phase Noise Optimization in Temporal Phase-Shifting Digital Holography with Partial Coherence Light Sources and Its Application in Quantitative Cell Imaging.* Applied Optics **48**, 1463–1472 (2009).

[37] S. Chen and Y. Zhu. *Phase Sensitivity Evaluation and Its Application to Phase Shifting Interferometry.* Methods **136**, 50–59 (2018).

[38] M. Piniard, B. Sorrente, G. Hug and P. Picart. *Modelling of the Photometric Balance for Two-Wavelength Spatially Multiplexed Digital Holography.* SPIE Optical Metrology 2021 **11783**, 1178308 (2021).

[39] P. Hosseini, R. Zhou, Y.-H. Kim, C. Peres, A. Diaspro, C. Kuang, Z. Yaqoob and P. T. C. So. *Pushing Phase and Amplitude Sensitivity Limits in Interferometric Microscopy.* Optics Letters **41**, 1656–1659 (2016).

[40] S. Chen, C. Li, C. Ma, T.-C. Poon and Y. Zhu. *Phase Sensitivity of Off-Axis Digital Holography.* Optics Letters **43**, 4993–4996 (2018).

[41] F. Charriére, B. Rappaz, J. Kühn, T. Colomb, P. Marquet and C. Depeursinge. *Influence of Shot Noise on Phase Measurement Accuracy in Digital Holographic Microscopy.* Optics Express **15**, 8818–8831 (2007).

[42] J. Goodman. *Introduction to Fourier Optics*. McGraw-Hill Physical and Quantum Electronics Series. W. H. Freeman, 2005.

[43] L. J. Van Vliet, D. Sudar and I. T. Young. *Digital Fluorescence Imaging Using Cooled Charge-Coupled Device Array Cameras*. Cell Biology **3**, 109–120 (1998).

3

SUB-PIXEL RESOLUTION AND CENTIMETER-SCALE DEPTH RANGE IN LENSLESS SINGLE-SHOT DWDH

Lensless single-shot dual-wavelength digital holography is resolution limited by the pixel-size of the camera and often has an insufficient depth range. We present a novel dual-wavelength holographic configuration with expanding wavefront illumination that breaks the pixel-limited resolution barrier and achieves diffraction-limited spatial resolution. By implementing expanding wavefront illumination with dual-wavelength digital holography based on a wavelength-tunable laser, we achieve a high-resolution centimeter-scale depth range. A quantitative precision analysis demonstrates that single-shot acquisition reaches the shot-noise-limited detection depth detection. The proposed holographic scheme provides a robust 3D optical inspection solution for high-throughput, micro-scale resolution industrial inline metrology.

This chapter has been published in APL Photonics **10**, 12 (2025) [1].

3

3.1. Introduction

In modern semiconductor manufacturing, device inspection, sample metrology, and defect detection play a critical role in ensuring good product quality and reliability [2, 3]. With growing manufacturing complexity, increasing throughput, and reduced sample dimensions, conventional 2D optical inspection methods struggle to meet demands [4, 5]. In high-speed semiconductor production lines, device inspection must not only achieve sub-micrometer 3D surface measurement accuracy, but also enable fast, non-contact imaging. Although existing optical 3D imaging techniques – including computational quatitative phase imaging [6], fringe projection profilometry [7], and optical coherence tomography [8] – each offer unique advantages, their application in industry is restricted by their limited resolution or need for scanning. Moreover, industrial environments can have vibrations, temperature fluctuations, and air disturbances that further complicate their use. Therefore, developing a 3D imaging technology that balances high resolution, large depth range, and resilience to environmental factors has become an urgent need in industrial inspection.

Off-axis digital holography (DH) [9–11] is an ideal choice for high-speed industrial inspection due to its single-shot, non-contact, full-field imaging capability and strong robustness against environmental noise [12–14]. However, conventional single-wavelength DH faces the fundamental 2π phase ambiguity limitation [15–17]. This issue occurs when the surface height variations exceed half the illumination wavelength (typically a few hundred nanometers), leading to 2π phase jumps that compromise the measurement accuracy. This is particularly problematic in industrial products with complex surface topography, as they often feature abrupt height changes that cause the failure of phase unwrapping algorithms.

Dual-wavelength digital holography (DWDH) [18–20] addresses this issue by combining two interferograms obtained at two different wavelengths. The holograms at the two wavelengths are typically multiplexed onto a single camera, allowing for single-shot DWDH acquisition. By combining the fields of the two wavelengths, a beat wave can be created with a synthetic wavelength that can span hundreds or even thousands of times the wavelength of the individual light sources. DWDH significantly expands the depth range while maintaining the native lateral resolution of single-wavelength DH systems, which makes it suitable for measuring complex surfaces with large height variations [21, 22]. However, DWDH still faces several challenges in industrial application settings. First, achieving a large depth range requires precise wavelength selection and stability. For example, to reach centimeter-scale depth ranges, the wavelength difference should be on the order of a few picometers, imposing stringent demands on wavelength accuracy and long-term stability [23, 24]. Second, for lensless DWDH configurations, despite their advantages in setup compactness and flexibility, they suffer from lateral resolution limitations dictated by the detector pixel size [25, 26].

Instead of achieving superresolution through the acquisition of multiple measurements [27–29], this paper demonstrates improved lateral resolution lensless DWDH using expanding wavefront illumination [30–33]. The proposed method overcomes the lateral resolution limit imposed by the detector finite-pixel size,

achieving an enhanced, numerical aperture-limited resolution. With DWDH implemented using a fixed wavelength and a tunable laser, centimeter-scale depth range and numerical-aperture limited resolution were demonstrated. We demonstrate a practical wavelength calibration scheme to ensure accurate height measurement and develop a corresponding phase-retrieval algorithm that corrects for additional expanding wavefront aberrations. Experimental results verify the feasibility of our method, with phase measurement precision approaching the shot-noise limit. The findings and methods presented in this paper are expected to advance the practical application of digital holography in industrial metrology and inspection.

3.2. METHODS

3.2.1. EXPANDING WAVE ILLUMINATION DUAL-WAVELENGTH DIGITAL HOLOGRAPHY SETUP

The setup for a reflective lensless dual-wavelength digital holography (DWDH) with expanding wavefront illumination (EWI) is illustrated in Figure 3.1(a). A He-Ne laser (HRS015B, Thorlabs) with wavelength $\lambda_1 = 632.992$ nm and a tunable laser diode (VBG-0633-020-BFY, Sacher Lasertechnik) with typical central wavelength $\lambda_2 = 633$ nm are used as light sources. Both beams first pass through a beam expander to increase the beam size to cover the entire sample. The beam expander for λ_1 is composed of two positive lenses (LA1805-A and LA1509-A, Thorlabs) and a pinhole (P30K, Thorlabs) and for λ_2 is composed of two lenses (LA1131-A and LA1509-A, Thorlabs) and a pinhole (P25K, Thorlabs). The expanded and collimated beam for λ_1 and λ_2 enter their respective Mach-Zehnder interferometers. For both wavelengths, the light is first split by a cube beam splitter (BS013, Thorlabs) into two beams: a reference beam (R) and an object beam (O). In the reference arm, lens $L2$ (LA1422-A, Thorlabs) is used to focus the reference beam and make an expanding wavefront, which is then reflected by a pellicle beam splitter P2 (BP250, Thorlabs). In the object arm, the beam is reflected by mirror M2, passes through a pellicle beam splitter P1 (BP250, Thorlabs), and is focused by lens $L1$ (LA1422-A, Thorlabs). The sample is illuminated by the expanding wavefronts, and the back-reflected field from the sample is redirected by a beam splitter BS2 (BS013, Thorlabs) to the camera. The object and reference beam interfere in the plane of the camera (MC124MG-SY-UB, XIMEA). The camera has dimensions of 4112×3008 pixels and a pixel size $\Delta x = \Delta y = 3.45$ µm). The case for λ_2 is similar.

Since the two lasers are mutually incoherent, the recorded hologram is the sum of the individual holograms and are recorded simultaneously on the camera. To enable single-shot measurement [34, 35], we deliberately arrange the two holograms to have distinct interference fringe orientations and employ spatial frequency multiplexing in the Fourier domain. The intensity of the resulting dual-wavelength hologram H_{DW} captured by the camera can be expressed as:

$$I_{DW} = \sum_i |O_i|^2 + |R_i|^2 + O_i R_i^* + O_i^* R_i \,, \tag{3.1}$$

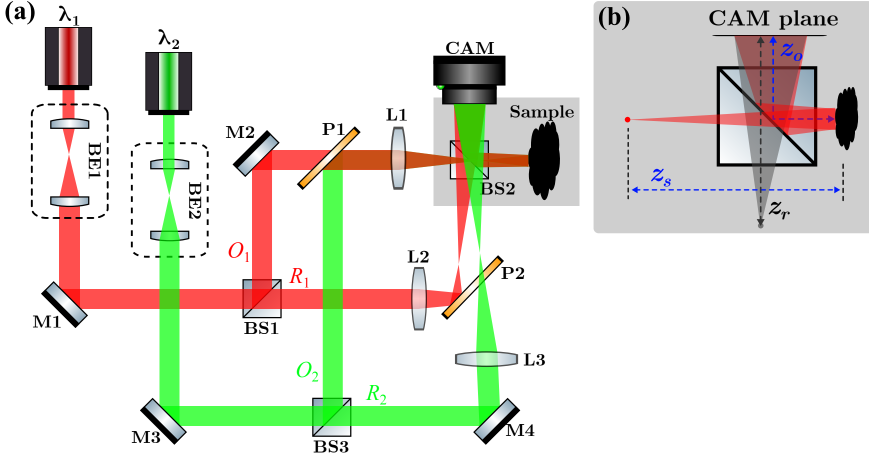

Figure 3.1: (a) Schematic diagram of a reflective lensless expanding wavefront DWDH setup (both lasers emit red beam, and the color difference is solely for visual distinction). M: Mirror; BS: Beam splitter; L: Lens; P: Pellicle; CAM: camera. (b) Zoom-in illustration of the illumination and reference beam. z_o: Sample-to-camera distance; z_s: Illumination focal point-to-sample distance. z_r: Reference beam focal point-to-camera distance.

where O_i and R_i refer to the object and reference fields at the detector plane respectively, $i = 1, 2$ indicates the two wavelengths, and the * is complex conjugation. Assuming the object field at the sample plane is $U(\xi, \eta) = |U| \exp(i\phi_o)$, where ϕ_o is the phase delay introduced by the object. The field O_i, resulting from the object being illuminated by the expanding wavefront and propagating to the camera, can be expressed as:

$$O_i(x, y) = \exp\left\{\frac{i\pi}{\lambda_i c_o}(x^2 + y^2)\right\} \cdot \\ \text{Fresnel}_{\frac{z_o}{M_a}} [U(\xi, \eta)] \left(\frac{x}{M_a}, \frac{y}{M_a}\right), \tag{3.2}$$

where $M_a = (z_o + z_s)/z_s$, z_o the sample-to-camera distance, and z_s the distance from the focal point of L1 to the sample, as illustrated in Figure 3.1(b). A physical interpretation of Eq. (3.2) is that the object field $U(\xi, \eta)$ undergoes Fresnel propagation over a distance z_o/M_a while being magnified by a factor M_a and has a parabolic phase term with curvature c_o. A detailed derivation and exact expression for the curvature c_o is provided in Appendix A. For the off-axis EWI holography configuration, the reference beam is modeled with a paraxial approximation of a spherical wavefront expressed as:

$$R_i = |R_i| \exp\left\{\frac{i\pi}{\lambda_i c_r}[(x - x_0)^2 + (y - y_0)^2]\right\}. \tag{3.3}$$

Here, the wavefront curvature parameter c_r corresponds to the distance z_r which is the distance from the source location of the expanding wave to the camera as defined in Figure 3.1(b), while x_0, y_0 are the lateral coordinates of the source location of the reference beam.

In standard off-axis digital holography processing, the off-axis term $O_i R_i^*$ is extracted by Fourier filtering, followed by a backpropagation to retrieve the sample phase ϕ_o. In DWDH, two phase maps ϕ_{o1} and ϕ_{o2} can be retrieved from the dual-wavelength hologram I_{DW}. The synthetic phase or beat phase Φ is calculated with $\Phi = \phi_{o1} - \phi_{o2}$. Assuming a single reflecting surface, the height h can be calculated according to

$$h = \frac{\Phi}{4\pi} \frac{\lambda_1 \lambda_2}{|\lambda_1 - \lambda_2|} = \frac{\Phi}{4\pi} \Lambda \,, \tag{3.4}$$

where $\Lambda = \frac{\lambda_1 \lambda_2}{|\lambda_1 - \lambda_2|}$ is the synthetic wavelength.

3.2.2. PWI- AND EWI- DWDH RESOLUTION

In conventional lensless digital holography with plane wavefront illumination (PWI), the lateral resolution depends on the numerical aperture (NA) and the size of the pixel. The NA is defined as $\mathrm{NA} = \sin(\tan^{-1}[\mathrm{W_{cam}}/(2z_o)])$, where $\mathrm{W_{cam}}$ is the width of the camera sensor, and z_o the sample-to-camera distance. The resolution for PWI is then $r = 0.82\lambda/\mathrm{NA}$, where the factor 0.82 is the proportionality factor commonly used for coherent imaging [36]. However, since the diffracted field is discretely sampled by the sensor, the pixel size Δx limits the lateral resolution. The maximum frequency support of the camera is given by the Nyquist limit, which restricts the lateral resolution to twice the pixel size $2\Delta x$. The achievable resolution is given by the larger one of the two. The resolution of DH is shown in Figure 3.2(a), where the dashed line shows the resolution for PWI-DH system with respect to the sample-to-camera distance z_o for a camera with the specifications as used in our experiment. As the distance decreases, the NA increases, and the diffraction-limited resolution decreases. However, at a certain distance, the diffraction-limited resolution equals twice the pixel size. Thereafter, no matter how much distance is reduced, the resolution no longer improves.

For the case of expanding wavefront illumination (EWI), as shown in the configuration of Figure 3.1(b), the optical field from the sample is progressively magnified as it propagates to the camera. The magnification of the field on the camera is $M_a = (z_o + z_s)/z_s$ (see Appendix A for a more detailed derivation). Equivalently, this can be viewed as the effective pixel size being reduced by a factor of M_a in the object plane. We can therefore conclude that, for the pixel size not to limit the spatial resolution, it must hold that

$$\frac{2\Delta x}{M_a} \leq 0.82 \frac{\lambda}{\mathrm{NA}} \,. \tag{3.5}$$

Substituting $M_a = (z_o + z_s)/z_s$ into the equation and rearranging, we get

$$\frac{\Delta x}{\lambda} \leq \frac{0.41}{\sin\left[\tan^{-1}\left(\frac{\mathrm{W_{cam}}}{2z_o}\right)\right]} \frac{z_o + z_s}{z_s} \,. \tag{3.6}$$

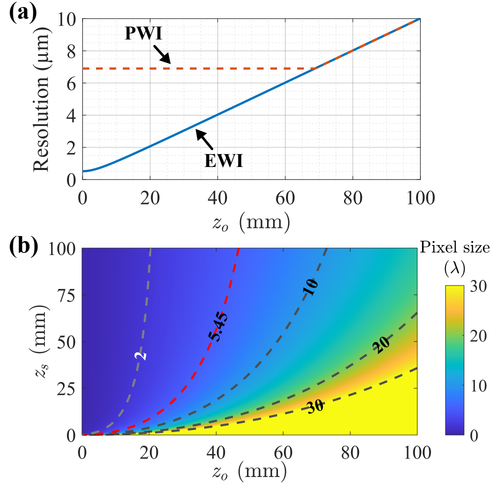

Figure 3.2: (a) Comparison of the lateral resolution in plane (PWI) and expanding wavefront illumination (EWI) holography. (b) Contour plot of the right-hand side of Eq. (3.6), which indicates the maximum allowed pixel size (in units of wavelength λ) to achieve diffraction-limited resolution.

Eq. (3.6) indicates that the diffraction-limited resolution is always achievable in the EWI-DH, provided that the system configuration fulfills the required condition. Figure 3.2(b) shows the contour plot of the right-hand side of Eq. (3.6), representing the maximum allowed pixel size (in units of wavelength λ) for a given setup with specific z_o and z_s to achieve diffraction-limited resolution. The red contour line in Figure 3.2(b) shows the pixel size of $\Delta x = 5.45\lambda$ of our setup. The resolution of EWI is depicted by the solid blue line in Figure 3.2(a) and shows a close to linear relation between object distance and resolution.

3.2.3. Quantitative phase reconstruction in EWI-DWDH

Extracting the sample phase ϕ_{oi} from the off-axis term $O_i R_i^*$ in EWI-DWDH is more complicated than in conventional PWI-DWDH. The entire data processing for EWI-DWDH is shown in Figure 3.3. Since the two wavefront curvatures of the object c_o and reference c_r can be mismatched, the term of $O_i R_i^*$ will contain a residual parabolic phase with curvature $c' = c_o c_r/(c_r - c_o)$. Any parabolic phase results in a broadening of the ± 1 orders in the Fourier spectrum. Figure 3.3(a) shows an experimental spectrum of a typical EWI-DWDH hologram and a zoomed-in view of one of the off-axis terms. The broadening of the spectrum is clearly seen in the diagonally distributed off-axis terms. Despite the broadening, the diffraction orders are well separated because of the carefully chosen incidence angle.

From an analysis of the spectrum, many parameters can be estimated [37–40]. For example, the residual wavefront curvature c' is related to the spread of the

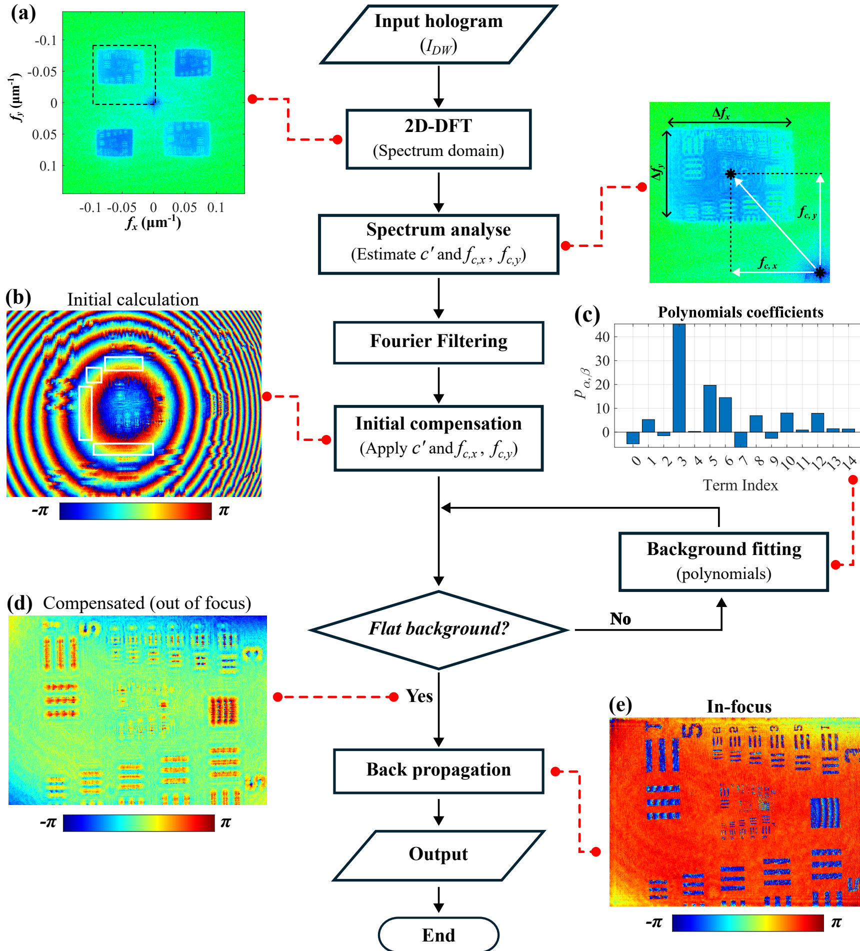

Figure 3.3: Data processing flowchart for EWI-DWDH. (a) Spectrum of a dual-wavelength hologram with expanding wavefront illumination. (b) Reconstructed phase of the off-axis term after initial compensation for tilt and parabolic phase. (c) Coefficients of the first 15 polynomials fitted from the background. (d) Compensated phase for (b). (e) The in-focus phase after backpropagation.

spectrum Δf_x and Δf_y, which is given by $\Delta f_x = M\Delta x/(\lambda_i c')$ along the x direction and $\Delta f_y = N\Delta y/(\lambda_i c')$ along the y direction. The carrier spatial frequencies can be estimated by measuring the distance between the coordinates origin and the centroid of the spectrum in the frequency domain, as indicated in Figure 3.3(a). The carrier spatial frequencies are expressed as $f_{c,x}$ for the x direction, and $f_{c,y}$ for the y direction. Figure 3.3(b) shows the experimental results of a reconstructed field of one of the off-axis terms after compensating for the slope and parabolic

phase calculated using the analysis described above. Clearly visible is a residual parabolic phase due to the imprecise determination of Δf_x and Δf_y. This imprecision arises from estimation errors that, as observed in the spectrum analysis step, originate from the unsharp edges of the off-axis term.

To address this issue, we implement a background fitting loop. Given a sample that contains known flat areas of the same height, we cut the flat areas out and fit an overall background phase map on them. Assuming that the objects located in the dashed boxes of Figure 3.3(b) are flat, coplanar, and the phase aberrations are continuous, they give a unique solution. We fit the phase from these areas with the standard polynomial

$$\phi_{fit}(x,y) = \sum_{\alpha+\beta=0}^{\alpha+\beta=\gamma} p_{\alpha,\beta} x^{\alpha} y^{\beta}, \tag{3.7}$$

where γ is the order of the fit, and $p_{\alpha,\beta}$ are the weight coefficients. For a specific order, there are $(\gamma+1)(\gamma+2)/2$ coefficients. In our experience, we found that fourth-order ($\gamma = 4$) is sufficient to cope with the phase distortions caused by aberrations that may be encountered.

Figure 3.3(c) shows the coefficients of the first 15 polynomials of the fitted result. It shows that the major components fall into the third and fifth terms, which correspond to x^2 and y^2. This result aligns with our expectation; Figure 3.3(b) shows that the spherical phase is dominant. Figure 3.3(d) shows the results after compensating for the fitted phase, which displays a homogeneous phase background, similar to a sample illuminated by a plane wave. Subsequently, the in-focus field (Figure 3.3(e)) is obtained through angular spectrum backpropagation of the equivalent distance z_e (see Appendix A for more details). However, note that when using the camera coordinates (x, y) instead of the scaled coordinates $\left(\frac{x}{M_a}, \frac{y}{M_a}\right)$, the actual backpropagation distance becomes $z_e M_a^2$ (or equivalently $z_o M_a$). The magnification M_a can be calibrated using a well-defined sample, such as a resolution target. Subsequently, the setup parameters z_o, z_s, c_r can be determined accordingly. The same data-processing procedures apply to the off-axis term for the second wavelength. If necessary, image registration is performed to correct for minor misalignment between the two on-focus images. Rigid registration is applied by circular shifting one image relative to the other. The cross-correlation coefficient is used as the similarity metric: the shift that produces the highest coefficient is chosen, and the image is translated accordingly to achieve optimal alignment.

3.2.4. LASER CALIBRATION AND TUNABILITY

Increasing the depth range of DWDH requires a large synthetic wavelength, which is equivalent to reducing the separation between the two wavelengths. Therefore, we use a highly stable, non-tunable He-Ne laser with a wavelength of $\lambda_1 = 632.992\,\text{nm}$. As a second wavelength (λ_2) source we use a tunable external cavity diode laser (ECDL) operating at approximately 633 nm, which can be slightly tuned in wavelength by adjusting the diode temperature or drive current. The key

challenge for obtaining a large synthetic wavelength is to accurately calibrate the operating wavelength of the ECDL. Achieving a cm-scale synthetic wavelength Λ requires λ_2 to be separated less than 40 pm from the wavelength of the He-Ne laser. A high-resolution wavemeter could address this problem by externally monitoring λ_2. However, a high-resolution wavemeter is not always available. Here, we propose a simple and practical method for calibrating the wavelength of ECDL. The proposed method involves using the DWDH setup to measure a sample with a well-defined step height. With the reconstructed beat phase Φ, Eq. (3.4) can be applied to calculate the synthetic wavelength, $\Lambda = 4\pi h/\Phi$. Assuming stable He-Ne laser operation at λ_1, λ_2 can be calculated as:

3

$$\lambda_2 = \frac{4\pi h \lambda_1}{4\pi h - \lambda_1 \Phi} . \tag{3.8}$$

This calibration was performed with a sample with several grooves with well-defined depths (Rubert & Co Ltd, product type 515). The groove with a depth of 1000 µm, was selected for calibration. To ensure complete imaging of the entire sample, the calibration was performed without using expanding wavefront illumination. Figure 3.4(a) shows the reconstructed complex field for synthetic wavelength from our DWDH setup (ECDL operating at $T = 18\,^{\circ}\mathrm{C}$ and $I = 91\,\mathrm{mA}$), where the image brightness indicates the reflected intensity and the color represents the synthetic phase. The bottom of the grooves has a distinctly different phase value compared to the surrounding surface, the black areas are locations where, due to shadowing, no reflected light reaches the camera. Figure 3.4(b) shows the cross section profile along the red dashed line in (a). The phase distribution on both sides of the grooves is not entirely flat due to the slight curvature of the workpiece surface. The plot exhibits a clear phase contrast with sharp transitions, indicating the distinct height change. To mitigate the effect of phase fluctuations, the phase value is calculated by selecting a small region and averaging the values within it. Thirty repeated experiments yield a result of $\Phi_{2-1} = 2.48 \pm 0.09$ rad with respect to the relative phase of the groove. Using the specified groove depth of 993.554 µm, we calculated $\Lambda = 5.04 \pm 0.18$ mm and $\lambda_2 = 633.072 \pm 0.003$ nm.

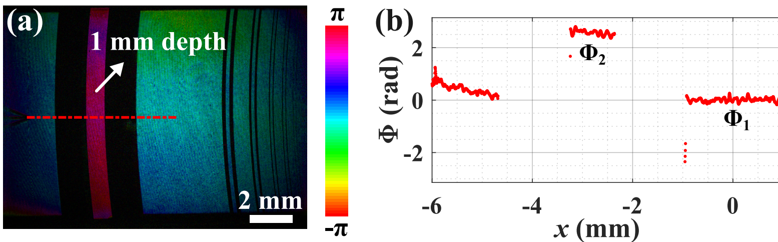

Figure 3.4: λ_2 calibration with a standard height sample. (a) Retrieved complex field of the sample, where the brightness indicates the amplitude and the color indicates the phase. (b) Cross section of the phase along the red dash line in (a).

3

The wavelength of the ECDL can be tuned by adjusting either the drive current or the diode temperature. In general, the wavelength λ_2 decreases with decreasing temperature and drive current. Using the same calibration procedure, we investigated the tunability of the ECDL. Figure 3.5 presents the calibration results for λ_2 at $T = 18\,^{\circ}\mathrm{C}$ with drive currents I ranging from 81 to 95 mA. For each drive current, 30 measurements were performed where the error bars in the plot represent the statistical standard deviation. The wavelength of the He-Ne laser ($\lambda_1 = 632.992\,\mathrm{nm}$) is plotted as the red dashed line in the plot. The results indicate that the ECDL undergoes mode hopping near drive currents of 82 and 93 mA. Between these points, λ_2 increases with increasing drive current, in agreement with the data provided by the manufacturer. Although additional λ_2 calibrations can be performed at different temperatures or drive currents, this demonstration shows the ability to precisely control both λ_2 and Λ.

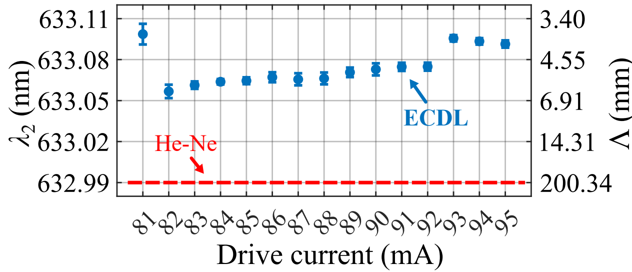

Figure 3.5: Drive current tuning of wavelength of the external cavity diode laser (ECDL) at $T = 18\,^{\circ}\mathrm{C}$. The right-hand axis indicates the obtained synthetic wavelength.

3.3. LATERAL RESOLUTION ENHANCEMENT RESULTS

The experimentally achievable resolution and field of view (FOV) were evaluated using a USAF resolution target. In lensless digital holography with PWI, the lateral resolution is mainly constrained by the numerical aperture (NA) and the sensor pixel size Δx. Figure 3.6(a) and (b) show the experimental results of optical field reconstruction under this configuration, where the FOV corresponds to the sensor size (10.38×14.19 mm^2 in our case). The sample-to-sensor distance, determined by visual optimization of image sharpness, is $z_o = 46.61$ mm, resulting in a theoretical resolution limit of $r_a = 4.66$ µm. However, since this value is smaller than twice the pixel size ($2\Delta x = 6.9$ µm), the achievable PWI resolution is limited to 6.9 µm. Figure 3.6(b) provides a zoomed-in view of the white dashed box in Figure 3.6(a), showing that the patterns of ”group 4 & 5” are distinguishable. The smallest distinguishable pattern is ”group 6-1”, its cross profile is plotted as the blue line in Figure 3.6(e). The nominal line spacing in ”group 6-1” is 7.81 µm, which can be considered as the effective resolution of the PWI system and closely approximates the expected resolution limit of two pixels.

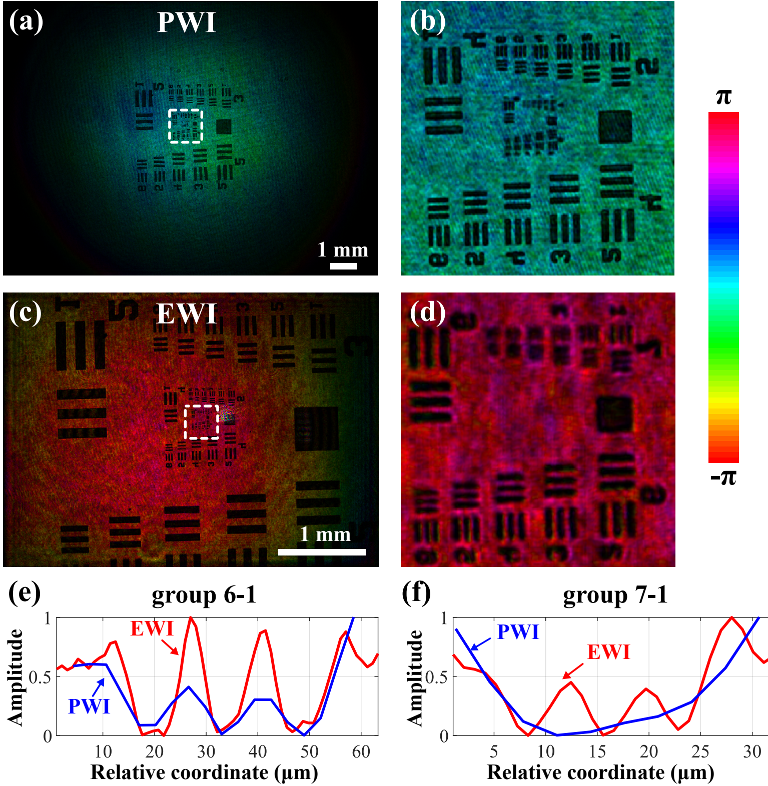

Figure 3.6: Achievable lateral resolution comparison in dual-wavelength digital holography. (a-b) Reconstructed field for plane wavefront illumination (PWI). (c-d) Reconstructed field for expanding wavefront illumination (EWI). (e) Comparison of cross profile plot of pattern in ”group 6-1”. (f) Comparison of cross profile plot of pattern in ”group 7-1”.

Figure 3.6(c) and (d) present the results obtained with EWI. As illustrated in Figure 3.2, the lateral resolution in lensless EWI-DWDH can be smaller than two pixels $2\Delta x$ as long as the configuration of the setup satisfies the condition in Eq. (3.6). From the reconstructed image in Figure 3.6(c), the magnification is determined as $M_a = 3.35\times$ by comparing the measured line spacing with the specified value. The sample-to-sensor distance is determined to be $z_o = 41.22$ mm. This closely matches the value measured with a ruler and differs slightly from the PWI presented in the previous paragraph because the two measurements were conducted independently. The distance z_s is calculated as 17.55 mm based on the relationship $M_a = (z_o + z_s)/z_s$. These parameters yield a theoretical diffraction limit of $r_a = 4.16$ μm, achievable as long as $z_s \leq 23.93$ mm. Since this condition for z_s is satisfied, the theoretical diffraction limit is NA limited to $r_a = 4.16$ μm. Figure 3.6(d) provides a zoomed-in view of the white dashed box in Figure 3.6(c),

showing that the pattern of "group 7-1" is just distinguishable, as can be seen from its cross-section profile that is plotted as the red line in Figure 3.6(f). The nominal line spacing in "group 7-1" is 3.91 µm, demonstrating the ability of EWI-DWDH to enhance resolution and break the pixel-size resolution limit. This resolution enhancement comes at the cost of a reduced lateral FOV, which, in EWI-DWDH, is scaled down by a factor of M_a. This reduction is evident when comparing the imaged object sizes in Figure 3.6 (a) and (c).

3.4. LARGE HEIGHT MEASUREMENTS RESULTS

To demonstrate our large DWDH depth-range measurement capability, we measured a stepped sample of which its surface covers a large height range. The sample was made of brass and machined with a high-precision CNC machine (Fehlmann, PICOMAX 56L TOP). It has multiple height steps with a height increment of 0.5 mm, as shown in Figure 3.7(a). The ECDL operated at a temperature of $T = 8.5\,°\mathrm{C}$ and a drive current of $I = 87\,\mathrm{mA}$, with the synthetic wavelength and the ECDL wavelength calibrated as $\Lambda = 9.17 \pm 0.25$ mm and $\lambda_2 = 633.0360 \pm 0.0012$ nm, respectively. Figure 3.7(b-c) shows the reconstructed complex fields for He-Ne and ECDL separately. In the field maps, brightness indicates the wave intensity and color represents the phase. Both maps share the same color and scale bar. The results clearly show distinct well-separated strips that are the steps of the sample. The phase values indicate depth variations, enabling the extraction of surface topography information. However, the inhomogeneous phase distribution at each step indicates surface irregularities, which appear on a scale larger than half the wavelength. Moreover, every step contains a few wrapped cycles of the phase, indicating fluctuations on the order of µm. Given the precision of the CNC machine (around 5 µm), this level of roughness is reasonable.

The two individual phase maps in Figure 3.7 show phase wrapping due to the large step height and height variation. Without additional information, phase unwrapping algorithms cannot resolve such sharp phase jumps. Figure 3.8(a) presents the result of applying a phase unwrapping algorithm [16] to the results in Figure 3.7(b). The steps are all mapped to the same height because the phase jumps are very large and there are areas where no phase information is available. This shows that the stepped structure cannot be reconstructed from single-wavelength DH. In DWDH, this issue is addressed by calculating the beat phase and the unambiguous height map is computed with Eq. (3.4). The reconstructed height map is presented in Figure 3.8(b), where all the steps, visualized with different colors, are distinguishable. Since each step is effectively flat on the millimeter scale, it is displayed in a relatively uniform color corresponding to its height. The inset displays the cross section along the black dashed line, providing a clearer visualization of the reconstruction of the stepped structure. From right to left, each step rises around 0.5 mm higher than the preceding one, as expected. The results demonstrate a successful measurement of all the steps without wrapping because the synthetic wavelength $\Lambda = 9.17 \pm 0.25$ mm covers the entire 3.5 mm height range of the sample. The 3D perspective image

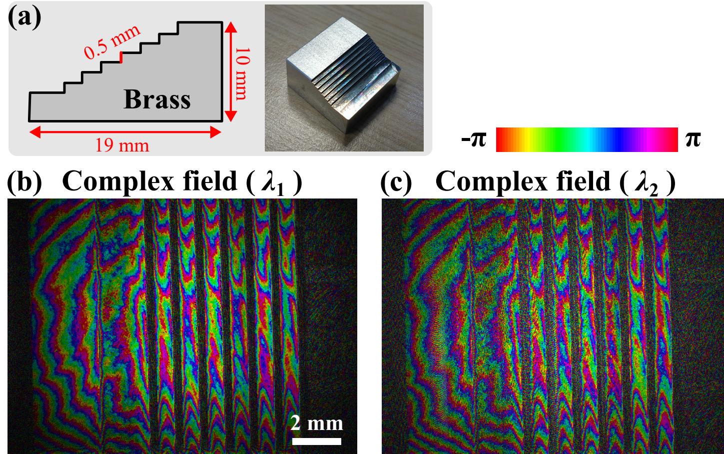

Figure 3.7: (a) Schematic on the left is a dimensional drawing of the stepped sample, and the photograph of it is on the right. Each step has a height of 0.5 mm. (b-c) The retrieved field for individual lasers.

in Figure 3.8(c) clearly illustrates the stepped stairs and the increase in height. For quantitative comparison, we set the rightmost step as the baseline and determined the relative heights of the remaining steps by averaging the height values from a small, central region of each step for both our measurement and the white-light interferometer (WLI, Bruker ContourGT-K). Figure 3.8(d), shows the obtained results with the horizontal axis showing the reference height measured by WLI, and the orange points represent the mean heights measured by our DWDH setup at $\Lambda = 9.17$ mm with error bars indicating standard deviation within each region. The black dashed line, with a slope of unity, serves as a reference. The spatial averaging in a center region minimizes edge effects and reduces noise.

To further validate the versatility of our method, we also performed measurements on objects with height variations exceeding 1 cm. The results, which are presented in Appendix 3.9 , confirm that we can quantitatively measure heights for cm-scale and potentially larger depth ranges. Since the height difference in this case surpasses the measurement range of our WLI system, no WLI reference measurements are provided.

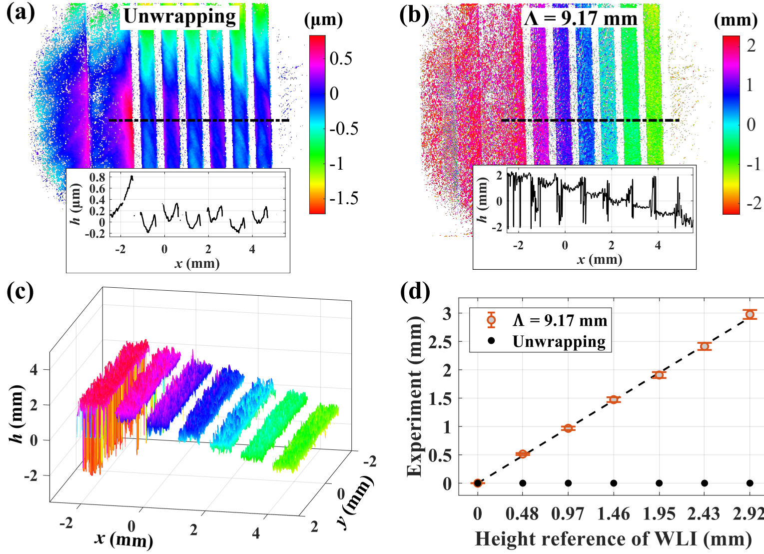

Figure 3.8: Height map reconstruction of the stepped sample. (a) Result of applying the phase unwrapping algorithm. (b) Results of dual-wavelength digital holography at $\Lambda = 9.17\,\mathrm{mm}$. (c) 3D perspective view of the result of (b). (d) Relative steps height for dual-wavelength digital holography and white light interferometry.

3.5. Instantaneous and temporal precision

DWDH phase measurements are affected by multiple noise sources, including speckle decorrelation noise, shot noise, and environmental disturbances such as mechanical vibrations and air currents [41–43]. Although noise is inherent in practical measurements, analyzing its sources and impact provides crucial insights into measurement precision. The single-shot measurement nature of our proposed method, with acquisition times under a 1 ms, minimizes the impact of ambient disturbances on individual measurements. However, the effect of these disturbances on long-time stability needs further investigation, as we will do here.

Instantaneous precision characterizes the reliability of a single DWDH measurement and is mainly influenced by speckle decorrelation and noise. Speckle decorrelation noise is caused by surface roughness. When the laser light scatters off a rough surface, microscale irregularities induce random phase shifts to the scattered wavefronts. The resultant constructive and destructive interference generates grainy speckle intensity patterns with a partially random phase. Increased levels of surface roughness enhance these phase variations, causing the speckle patterns to decorrelate more rapidly, resulting in more pronounced phase fluctuations. Technical noise sources include shot noise, quantization noise, dark noise, and laser intensity fluctuations or relative intensity noise. Among these, shot noise is the fundamental limitation in phase-reconstruction precision. According to the model

developed by Gong and Piniard [41, 44] the phase retrieval precision from an off-axis hologram is

$$\sigma_\phi = \sqrt{\frac{4\cdot \mathrm{FR}}{V^2\alpha^2}\left[\frac{\alpha}{N_{sat}} + \frac{1}{12(2^{nbit}-1)^2}\right] + \left(\frac{7}{4}\right)^2\left(\frac{8\pi^2 R_a^2}{\Lambda^2}\right)^{\frac{4}{5}}}, \quad (3.9)$$

where, FR is the filter ratio of the filter window size used to extract the off-axis terms to the total spatial bandwidth of the sensor in the spatial frequency domain, N_{sat} is the full well capacity of a pixel, and $nbit$ indicates the image bit depth. The parameters V and α represent the modulation depth (or fringe visibility) and saturation of the hologram, respectively. R_a is the surface roughness. Under the square root, the first term corresponds to the shot noise contribution, the second term represents the quantization noise contribution, and the third term accounts for speckle decorrelation noise. Dark noise and readout noise are excluded from consideration in Eq. (3.9) as we will show them to be negligible.

3

To isolate the system from speckle decorrelation noise effects, a mirror was used as a test sample. The theoretical phase precision was calculated using Eq. (3.9) for a hologram captured with a camera having $N_{sat} = 9900e^-$ and recorded as a grayscale image of $nbit = 8$. The exposure time was around 200 µs and was maximized without causing overexposure. Additional parameters were determined during data processing. For example, the modulation depth of the hologram V was calculated as $V_i = 2AC_i/DC$, where AC_i is the amplitude of the off-axis term and DC is the amplitude of the constant background bias. Both values are obtained through Fourier filtering and are spatially dependent. In DWDH, the DC bias is a superposition of the individual DC biases from two lasers and cannot be separated without additional measurements. Similarly, since the individual hologram saturation α cannot be determined independently, we assume they are equivalent for both lasers, leading to $\alpha = 0.5 \cdot DC/(2^{nbit}-1)$. The resulting theoretical precision values σ_ϕ^T are 18.0 mrad for the He-Ne laser and 12.9 mrad for the ECDL. The theoretical beat phase precision σ_Φ^T is calculated as 22.1 mrad by computing the square root of their summed squares.

Experimental evaluation of the instantaneous phase precision was performed through differential measurements: the phase map of one hologram was subtracted from that of the subsequent hologram. This process cancels out constant illumination aberrations that would otherwise bias the calculated spatial phase variance. The analysis focused on a central 256 × 256 pixel region with relatively uniform amplitude. Figure 3.9 shows the beat phase map (a) and its statistical distribution (b). Ideally, the phase across the mirror should be constant; however, the observed fluctuations – displayed as a quasi-Gaussian distribution in the histogram (Figure 3.9(b)) – indicate the presence of noise. The experimental measurement yielded a standard deviation of $\sigma_\Phi^E = 31.1$ mrad, which is slightly higher than the theoretical expected precision σ_Φ^T. This discrepancy may be attributed to data imperfections, including parasitic fringes caused by coherent laser diffraction and internal optical reflections superimposed on the hologram. The Gaussian shape of the phase distribution is in agreement with the predominance

3

of shot-noise, since the high surface flatness (peak-to-valley: 63 nm) leads to low decorrelation noise (0.75 mrad phase deviation).

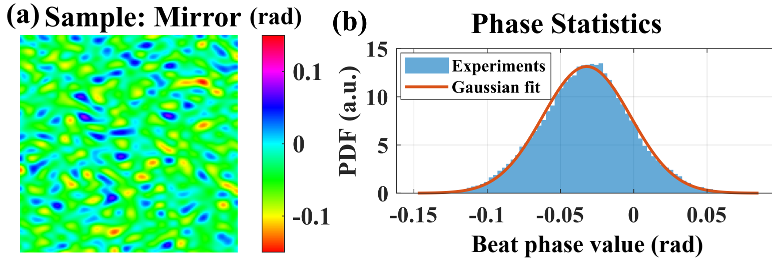

Figure 3.9: (a) Single frame beat phase map Φ on a central area of a mirror. (b) Statistical distribution of the beat phase values in (a).

The temporal precision of the phase measurements was investigated using 10000 consecutive holograms from a mirror, acquired at a rate of 100 Hz. A specific point was selected from the retrieved phase maps, and its phase value was tracked over time. Figure 3.10(a) displays the time series of the phase at this point showing from top to bottom the He-Ne laser field phase ($\phi_{\text{He-Ne}}$), the ECDL field phase (ϕ_{ECDL}), and the beat phase (Φ). All three signals exhibited significant temporal phase fluctuations, an expected outcome considering the ambient vibrations in the lab and the inherent sensitivity of phase measurement. Power spectral density (PSD) analysis (Figure 3.10(b)) reveals local maxima at 38 Hz and 47 Hz in both $\phi_{\text{He-Ne}}$ and ϕ_{ECDL}. These spectral peaks are absent in the PSD plot of Φ, suggesting that a common noise source – possibly camera noise or sample jitter – affects the phase of both lasers equally and cancels out during the beat-phase calculation.

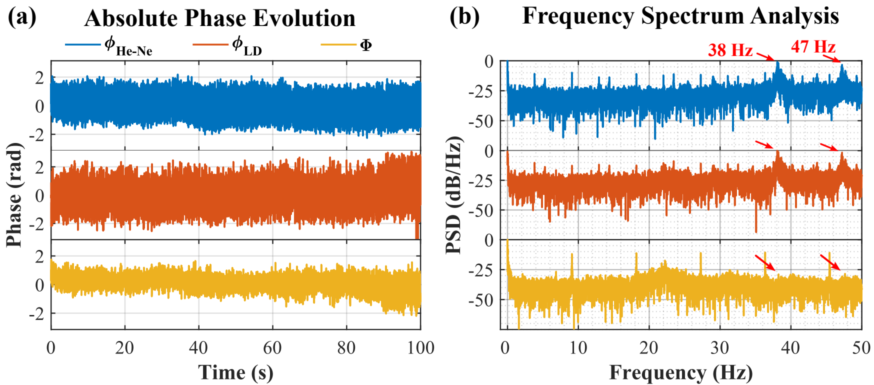

Figure 3.10: (a) Time resolved results of three phase values at one point: He-Ne laser field phase ($\phi_{\text{He-Ne}}$), ECDL field phase (ϕ_{ECDL}), and beat phase (Φ). (b) The corresponding power spectral density (PSD) analysis.

However, the time-domain plot of the absolute beat phase Φ still exhibits

significant fluctuations. The corresponding PSD shows that while the data is free from characteristic frequency noise, perturbations at 9 Hz and its integer multiples are visible, although their origin remains unidentified. The strong temporal jitter in the absolute beat phase Φ can be attributed to the non-common path system, in which the two arms are exposed to different environmental disturbances. In this case, the effect of vibrations manifests itself in frame-to-frame uncertainty and can be treated as random noise over long time periods. We mitigated this issue by selecting two points on the sample and calculating the relative phase difference, $\Delta\Phi$. The result, shown in Figure 3.11(a), demonstrates that the phase variation is significantly reduced. The PSD plot of $\Delta\Phi$ has a pattern similar to that of the absolute phase Φ but with a significantly reduced amplitude. This provides indirect confirmation of the temporal randomness of the noise, as its elimination results in an overall background reduction in the PSD plot.

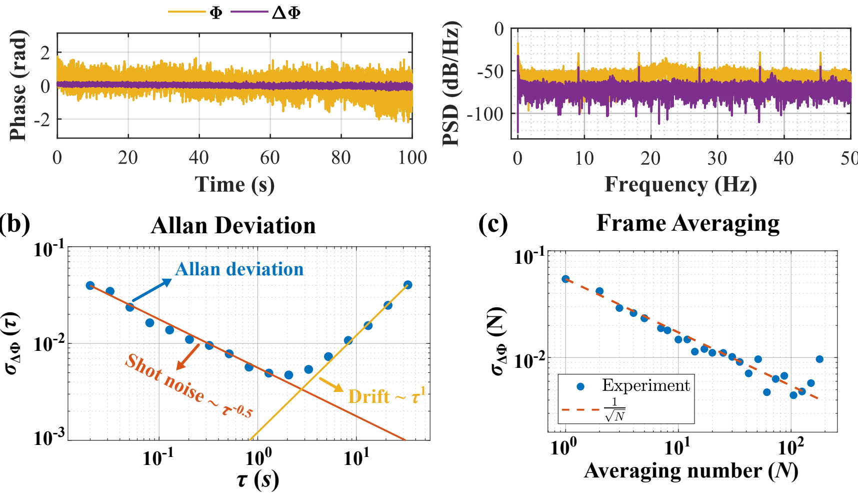

Figure 3.11: (a) Comparative analysis of Φ and $\Delta\Phi$ in the time and frequency domain. (b) Allan deviation analysis regarding $\Delta\Phi$. (c) Standard deviation of the synthetic phase versus frame number showing the reduction of the noise upon averaging.

To further elucidate the cause of the noise, we applied an Allan variance analysis [45], which is a widely used and effective tool for characterizing temporal stability, providing insights into various noise types and long-term drift behavior. In the Allen variance analysis, the time series phase data are segmented into sections of equal duration τ and the phase is averaged. Then it quantifies how much the time average of each section differs from that of the previous average, mathematically expressed as

$$\sigma^2_{\Delta\Phi}(\tau) = \frac{1}{2}\langle(\overline{\Delta\Phi}_{i+1} - \overline{\Delta\Phi}_i)^2\rangle\,, \tag{3.10}$$

where $\langle\ .\ \rangle$ denotes temporal averaging, $\overline{\Delta\Phi}_i$ is the ith sample of the average of $\Delta\Phi$ over observation time τ. Figure 3.11(b) shows an Allan deviation ($\sqrt{\sigma^2(\tau)}$) analysis of $\Delta\Phi$ and is plotted on a log-log scale, with τ ranging from 0.02 s to around 33 s. The calculated Allan deviation from the experimental data is represented by the blue curve, accompanied by two trend lines illustrating different noise components: shot noise (shown in red), which has a slope of $\tau^{-0.5}$, and systematic drift (shown in yellow), which has a slope of τ^1. For short averaging times ($\tau < 1$ s), the Allan deviation $\sigma(\tau)$ decreases with a slope similar to the shot noise line. As the averaging time increases, systematic drift becomes dominant, causing $\sigma(\tau)$ to increase roughly as τ^1. The minimum occurs around $\tau = 1$ - 2 s, indicating the maximum averaging duration to achieve minimal signal noise before drift becomes dominant. The predominance of shot noise on short time scales was verified by comparing the measured standard deviation σ against the frame averaging number (N), as shown in Figure 3.11(c). The experimental data points (blue dots) closely align with the theoretical prediction of $1/\sqrt{N}$ (dashed red line), confirming shot noise as the primary noise source at short time scales [42, 43].

3.6. Discussion

The height measurement precision of DWDH is fundamentally determined by the phase measurement accuracy, which in our setup is primarily limited by shot noise. We achieve an experimental phase measurement accuracy of $\sigma_\Phi^E = 31.1$ mrad. As described by Eq. (3.4), the height error scales linearly with the synthetic wavelength Λ, i.e., $\sigma_h = \sigma_\Phi^E/(4\pi)\cdot\Lambda = 0.24\%\Lambda$. Phase averaging techniques can effectively improve phase precision by a factor of $\sqrt{N}$ in shot-noise-limited detection, where N is the number of averaged frames, as shown in Figure 3.11. Practical implementation in our setup allows for averaging up to 100 frames (see Figure 3.11(c)), thereby providing up to tenfold improvement. Besides, frame averaging compromises the single-shot nature of our approach and may introduce errors due to lateral sample drift.

To preserve the advantages of single-shot measurement, an approach to obtain better height sensitivity is to use more optical power to reduce relative phase noise. In principle, the single-shot height measurement range is infinite. We have shown height measurements in excess of 1 cm, see Appendix 3.9. However, further extending this range will be limited by the wavelength stability of both lasers and the accuracy of the calibration method. Another approach to obtain an improved height sensitivity is to use the tunability of Λ to optimize the height precision for a given sample, where the highest precision is obtained by choosing Λ just larger than twice the expected height difference. Additionally, although median filtering was applied to suppress high-frequency noise in our results, further improvement is possible. Advanced denoising techniques, both numerical and experimental strategies, could be explored in future work to further enhance measurement precision.

Although DWDH can be performed using a single light source combined with acousto-optic modulators (AOM) [23] the selection of the ECDL as secondary light

source was primarily motivated by three considerations.

First, the ECDL provides relatively broad wavelength tunability. Similar to Figure 3.5, which shows the operating wavelength of the ECDL at $T = 18\,^{\circ}\mathrm{C}$, we performed wavelength calibrations at various temperatures (T) and drive currents (I). These results show wavelength overlap with the emission band of the He-Ne laser and a tuning range up to a maximum wavelength of 633.756 nm (achieved at $T = 30\,^{\circ}\mathrm{C}$ and $I = 103\,\mathrm{mA}$). Based on this tuning range, the synthetic wavelength Λ can be varied from 0.53 mm to effectively infinity. In contrast, AOM-based approaches generally only provide a frequency shift less than 1 GHz, which restricts $\Lambda \geq 300\,\mathrm{mm}$.

Second, the ECDL provides application-specific height resolution control. Considering that the height precision is linear to Λ and that semiconductor products have height variations in the sub-mm to cm scale range, the use of an ECDL provides better height resolution and sensitivity. However, ECDL mode hopping may occur during ECDL tuning, and operating at the extremities of the tuning range can induce output instability, resulting in linewidth broadening and coherence degradation. These effects should be carefully avoided, for example, by using an ECDL frequency locked to the HeNe laser [46].

Third, ECDL power generation is efficient. Although commercial low-frequency AOMs can achieve 70-90% first-order diffraction efficiency, their performance is highly sensitive to angular alignment and thermal stability. In contrast, high-frequency AOMs suffer from significant losses, as exemplified by a mere 11% diffraction efficiency for a 5 GHz frequency shift [47]. This technical limitation becomes critical when considering the generation of cm-scale synthetic wavelengths, where the required frequency shift exceeds 30 GHz. Additionally, because the dual-wavelength scheme requires use of the zero- and first-order transmitted beam as well, this imposes high demands on the laser power.

This paper demonstrates that expanding wavefront illumination breaks the pixel size limitation on spatial resolution, leaving it only constrained by the NA of the system. Hence, the demonstrated spatial resolution of 3.91 µm, as shown in Figure 3.6, is not the fundamental limit. Reduction of the sample-sensor distance can improve resolution, but practical constraints arise from the physical dimensions of the beam splitter that limit the reduction of the object to sensor distance. An alternative approach involves using larger-size detectors, where the demonstrated decoupling of resolution from the pixel size allows the use of larger-pixel sensors while maintaining the resolution enhancement potential.

3.7. CONCLUSION

In this paper, we demonstrated a lensless, single-shot dual-wavelength digital holography scheme with expanding wavefront illumination (EWI-DWDH). Our method overcomes the pixel-size limitations inherent in the spatial resolution of conventional digital holography systems. Experimental results demonstrate that the EWI-DWDH enhances spatial resolution to 3.91 µm (smaller than two pixels 6.9 µm) and is in agreement with diffraction-limited theoretical predictions.

Moreover, by combining a tunable diode laser with a He–Ne laser, a centimeter-scale depth measurement range is achieved, thereby broadening the applicability of digital holography in 3D industrial inspection. With respect to measurement precision, the single-shot nature of our approach yields results that approach shot-noise limited detection efficiency. However, systematic drift does affect the measurements for long-time operation. In summary, the proposed scheme provides an efficient and precise 3D inspection tool for industrial fields with stringent requirements for high speed, high resolution, wide field-of-view, and high precision, such as semiconductor manufacturing.

3.8. Appendix A: The equivalent propagation distance

Considering the model illustrated in Figure 3.1(b), and assuming that the sample field is $U(\xi,\eta)$, the optical field of the sample illuminated with a spherical wave right after the sample could be written as

$$U_1(\xi,\eta) = U(\xi,\eta)\exp\left[\frac{i\pi}{\lambda z_s}(\xi^2+\eta^2)\right]. \tag{3.11}$$

This field propagates a distance z_o to the camera plane, assuming the paraxial approximation holds in this propagation (i.e.,$z_o \gg \sqrt[3]{\pi D^4/(4\lambda)}$, where D is the diameter of the sample), then the object field at the camera plane can be described by the Fresnel diffraction integral [38]

$$\begin{aligned} U_2(x,y,z_o) = \exp\left[\frac{i\pi}{\lambda z_o}(x^2+y^2)\right] \iint U_1(\xi,\eta) \\ \exp\left[\frac{i\pi}{\lambda z_o}(\xi^2+\eta^2)\right]\exp\left[-\frac{i2\pi}{\lambda z_o}(x\xi+y\eta)\right]\mathrm{d}\xi\mathrm{d}\eta\,. \end{aligned} \tag{3.12}$$

Notably, substituting Eq. (3.11) into the integral and defining $z_e = z_o z_s/(z_o+z_s)$ and $M_a = (z_o+z_s)/z_s$, the first two parabolic terms in the integrand can be combined and the last exponential term can also be rewritten, producing the integrand having an expression as

$$U(\xi,\eta)\exp\left[\frac{i\pi}{\lambda z_e}\left(\xi^2+\eta^2\right)\right]\exp\left[-\frac{i2\pi}{\lambda z_e}\left(\frac{x}{M_a}\xi+\frac{y}{M_a}\eta\right)\right]. \tag{3.13}$$

The variable z_e is what we call the equivalent propagation distance and M_a is the magnification factor. The physical meaning of these parameters will become clearer in the following derivation. A closer examination of Eq. (3.13) reveals that it also takes the form of a Fresnel diffraction integral, except that it lacks a parabolic phase term for the scaled coordinates $\left(\frac{x}{M_a},\frac{y}{M_a}\right)$, and the propagation distance is replaced by z_e. Therefore, Eq. (3.12) can be expressed as:

$$U_2(x,y,z_o) = \exp\left[\frac{i\pi}{\lambda(z_o+z_s)}(x^2+y^2)\right]\cdot U_2'\left(\frac{x}{M_a},\frac{y}{M_a},z_e\right), \tag{3.14}$$

$$U_2'(\frac{x}{M_a},\frac{y}{M_a},z_e) = \iint U(\xi,\eta)\exp\left\{\frac{i\pi}{\lambda z_e}\left[\left(\frac{x}{M_a}-\xi\right)^2+\left(\frac{y}{M_a}-\eta\right)^2\right]\right\}\mathrm{d}\xi\mathrm{d}\eta. \tag{3.15}$$

Eqs. (3.14) and (3.15) imply that the field $U_2'\left(\frac{x}{M_a},\frac{y}{M_a},z_e\right)$ is essentially a geometrically magnified sample field $U(\xi,\eta)$ illuminated by a plane wave and propagating an equivalent distance z_e. The object field $U_2(x,y,z_o)$ is essentially $U_2'\left(\frac{x}{M_a},\frac{y}{M_a},z_e\right)$ with a superimposed parabolic phase distribution. To validate this equivalence, we conducted numerical simulations using a rectangular function as input. Figure 3.12 shows a simulated comparison of diffraction amplitudes. The black line is the input, and the blue curve represents the theoretical prediction from Eq. (3.12) with a propagation distance $z_o = 41.22$ mm (the same value as Section 3.3). The green curve shows the object field with plane wave illumination and propagating the equivalent distance $z_e = 12.31$ mm, as given by Eq. (3.15). After applying coordinate scaling to the green curve, the result (red dashed line) shows perfect agreement with the prediction (blue). The inset in the figure shows more clearly the role of coordinate scaling and the equivalence of two methods.

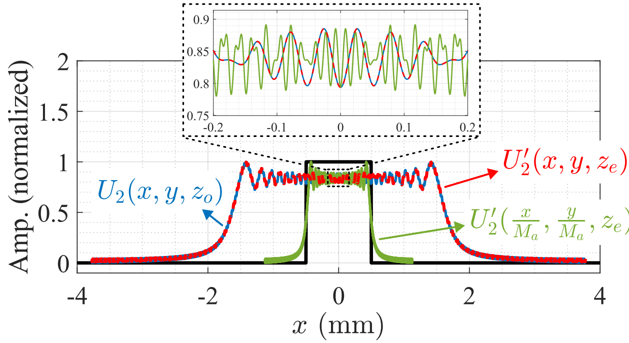

Figure 3.12: Comparison of diffraction amplitudes calculated with two different methods.

3.9. APPENDIX B: VALIDATION OF CENTIMETER-SCALE DEPTH MEASUREMENT

To validate the capability of the method for centimeter-scale depth measurements, we measured a combined object consisting of a 10-mm step and a standard height sample. This arrangement enabled simultaneous wavelength calibration and height measurement in a single acquisition. Figure 3.13(a) shows the object. The

beat phase map reconstructed by our system is presented in Figure 3.13(b). The wavelength calibration procedure follows that described in the main text. After compensating for tilt in the yellow box region, Figure 3.13(c) displays the phase map and the cross-sectional profile for standard height measurement. From the known groove depth and phase difference, the synthetic wavelength and the ECDL wavelength were determined as $\Lambda = 44.52 \pm 8.15$ mm and $\lambda_2 = 633.0010 \pm 0.0013$ nm (from 20 measurements and the ECDL operated at $T = 9.4\,^{\circ}$C and $I = 96\,$mA).

After calibration, the height of the step in the red box region can be quantified using the obtained synthetic wavelength. Figure 3.13(d) shows the processed phase map (tilt-compensated and converted to height), along with the cross-sectional profile. The step height was measured as 10.31 ± 0.256 mm. Due to the rough surface, some fluctuations are observed, so the reported value is the average over small regions. These results confirm the effectiveness of our method for achieving centimeter-scale depth measurements and potential larger synthetic wavelengths.

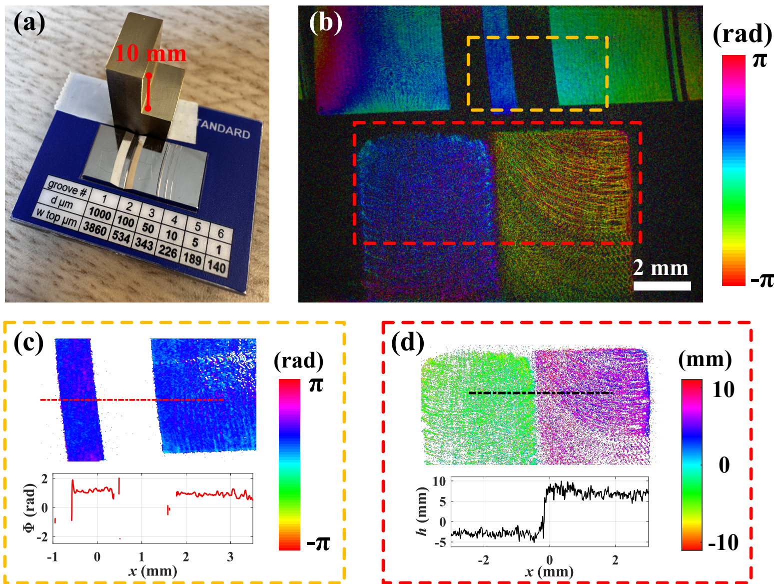

Figure 3.13: (a) Object with a 10 mm step and standard height sample. (b) Reconstructed beat phase map. (c) Reconstruction on the standard-height sample (yellow box in (b)) for the wavelength calibration. (d) Height map and cross profile for the step measurement.

REFERENCES

[1] H. Shangguan, H. P. Urbach and J. Kalkman. *Lensless Single-Shot Dual-Wavelength Digital Holography with Sub-Pixel Resolution and Centimeter Depth Range*. APL Photonics **10** (2025).

[2] R. B. Bergmann, M. Kalms and C. Falldorf. *Optical In-Process Measurement: Concepts for Precise, Fast and Robust Optical Metrology for Complex Measurement Situations*. Applied Sciences **11**, 10533 (2021).

[3] Y. Shimizu, L.-C. Chen, D. W. Kim, X. Chen, X. Li and H. Matsukuma. *An Insight into Optical Metrology in Manufacturing*. Measurement Science and Technology **32**, 042003 (2021).

[4] R. Leach. *Optical Measurement of Surface Topography*. Springer Berlin Heidelberg, 2011.

[5] S. Catalucci, A. Thompson, S. Piano, D. T. Branson and R. Leach. *Optical Metrology for Digital Manufacturing: A Review*. The International Journal of Advanced Manufacturing Technology **120**, 4271–4290 (2022).

[6] A. Ivanina, M. Marshall, K. Abrashitova, T. van Leeuwen and L. V. Amitonova. *Quantitative Phase Imaging with a Multimode Fiber*. APL Photonics **10**, 046116 (2025).

[7] J. Xu and S. Zhang. *Status, Challenges, and Future Perspectives of Fringe Projection Profilometry*. Optics and Lasers in Engineering **135**, 106193 (2020).

[8] M.-Y. Fu, Z.-H. Yin, X.-Y. Yao, J. Xu, Y. Liu, Y. Dong and Y.-C. Shen. *The Progress of Optical Coherence Tomography in Industry Applications*. Advanced Devices & Instrumentation **5**, 0053 (2024).

[9] D. Gabor. *A New Microscopic Principle*. Nature **161**, 777–778 (1948).

[10] E. N. Leith and J. Upatnieks. *Reconstructed Wavefronts and Communication Theory*. J. Opt. Soc. Am. **52**, 1123–1130 (1962).

[11] B. Tayebi, M. R. Jafarfard, F. Sharif, Y. S. Bae, S. H. H. Shokuh and D. Y. Kim. *Reduced-Phase Dual-Illumination Interferometer for Measuring Large Stepped Objects*. Optics Letters **39**, 5740–5743 (2014).

[12] E. Cuche, F. Bevilacqua and C. Depeursinge. *Digital Holography for Quantitative Phase-Contrast Imaging*. Optics Letters **24**, 291–293 (1999).

[13] Z. Huang and L. Cao. *Quantitative Phase Imaging Based on Holography: Trends and New Perspectives*. Light: Science & Applications **13**, 145 (2024).

3

[14] J. Huang, S. Zhu, Y. Li, C. Wang and E. Y. Lam. *Computational Polarized Holography for Automatic Monitoring of Microplastics in Scattering Aquatic Environments*. APL Photonics **10**, 036114 (2025).

[15] H. S. Abdul-Rahman, M. A. Gdeisat, D. R. Burton, M. J. Lalor, F. Lilley and C. J. Moore. *Fast and Robust Three-Dimensional Best Path Phase Unwrapping Algorithm*. Applied Optics **46**, 6623–6635 (2007).

[16] M. A. Herráez, D. R. Burton, M. J. Lalor and M. A. Gdeisat. *Fast Two-Dimensional Phase-Unwrapping Algorithm Based on Sorting by Reliability Following a Noncontinuous Path*. Applied Optics **41**, 7437–7444 (2002).

[17] S. Park, Y. Kim and I. Moon. *Automated Phase Unwrapping in Digital Holography with Deep Learning*. Biomedical Optics Express **12**, 7064–7081 (2021).

[18] J. Gass, A. Dakoff and M. K. Kim. *Phase Imaging without 2π Ambiguity by Multiwavelength Digital Holography*. Optics Letters **28**, 1141–1143 (2003).

[19] H. Zhou, M. M. R. Hussain and P. P. Banerjee. *A Review of the Dual-Wavelength Technique for Phase Imaging and 3D Topography*. Light: Advanced Manufacturing **3**, 314–334 (2022).

[20] M. K. Kim. *Phase Microscopy and Surface Profilometry by Digital Holography*. Light: Advanced Manufacturing **3**, 481–492 (2022).

[21] M. Piniard, B. Sorrente, G. Hug and P. Picart. *Melt Pool Monitoring in Laser Beam Melting with Two-Wavelength Holographic Imaging*. Light: Advanced Manufacturing **3**, 14–25 (2022).

[22] D. Khodadad, E. Hällstig and M. Sjödahl. *Shape Reconstruction Using Dual Wavelength Digital Holography and Speckle Movements*. Optical Measurement Systems for Industrial Inspection VIII **8788**, 106–116 (2013).

[23] U. Abeywickrema, D. Beamer, P. Banerjee and T.-C. Poon. *Holographic Topography Using Acousto-Optically Generated Large Synthetic Wavelengths*. Practical Holography XXX: Materials and Applications **9771**, 69–75 (2016).

[24] A. Wada, M. Kato and Y. Ishii. *Large Step-Height Measurements Using Multiple-Wavelength Holographic Interferometry with Tunable Laser Diodes*. J. Opt. Soc. Am. A **25**, 3013–3020 (2008).

[25] H. Shangguan, H. P. Urbach and J. Kalkman. *Lensless Single-Shot Dual-Wavelength Digital Holography for Industrial Metrology*. Applied Optics **63**, 4427–4434 (2024).

[26] E. Serabyn, K. Liewer, C. Lindensmith, K. Wallace and J. Nadeau. *Compact, Lensless Digital Holographic Microscope for Remote Microbiology*. Optics Express **24**, 28540–28548 (2016).

[27] X. Wu, J. Sun, Y. Chen, J. Wei, Q. Chen, T.-C. Poon, P. Gao and C. Zuo. *Wavelength-Scanning Pixel-Super-Resolved Lens-Free on-Chip Quantitative Phase Microscopy with a Color Image Sensor*. APL Photonics **9**, 016111 (2024).

[28] Y. Gao and L. Cao. *Iterative Projection Meets Sparsity Regularization: Towards Practical Single-Shot Quantitative Phase Imaging with in-Line Holography*. Light: Advanced Manufacturing **4**, 37–53 (2023).

[29] Z. Huang and L. Cao. *K-Space Holographic Multiplexing for Synthetic Aperture Diffraction Tomography*. APL Photonics **9**, 056101 (2024).

[30] E. Serabyn, K. Liewer and J. K. Wallace. *Resolution Optimization of an Off-Axis Lensless Digital Holographic Microscope*. Applied Optics **57**, A172–A180 (2018).

[31] F. Wicki and T. Latychevskaia. *Double-Slit Holography—a Single-Shot Lensless Imaging Technique*. Scientific Reports **14**, 12528 (2024).

[32] S. Na, S. Shin and Y. Yu. *Digital Holographic Microscopy Using a Spherical Reference Wave and Polarization Hologram*. Journal of the Korean Physical Society **77**, 908–911 (2020).

[33] S. Rehman, K. Matsuda, M. Yamauchi, M. Muramatsu, G. Barbastathis and C. Sheppard. *A Simple Lensless Digital Holographic Microscope*. Biomedical Optics and 3-D Imaging (2012), Paper DSu3C.3, DSu3C.3 (2012).

[34] J. Kühn, T. Colomb, F. Montfort, F. Charrière, Y. Emery, E. Cuche, P. Marquet and C. Depeursinge. *Real-Time Dual-Wavelength Digital Holographic Microscopy with a Single Hologram Acquisition*. Optics Express **15**, 7231–7242 (2007).

[35] D. G. Abdelsalam, R. Magnusson and D. Kim. *Single-Shot, Dual-Wavelength Digital Holography Based on Polarizing Separation*. Applied Optics **50**, 3360–3368 (2011).

[36] T. Latychevskaia. *Lateral and Axial Resolution Criteria in Incoherent and Coherent Optics and Holography, near- and Far-Field Regimes*. Applied Optics **58**, 3597–3603 (2019).

[37] J. Min, B. Yao, S. Ketelhut, C. Engwer, B. Greve and B. Kemper. *Simple and Fast Spectral Domain Algorithm for Quantitative Phase Imaging of Living Cells with Digital Holographic Microscopy*. Optics Letters **42**, 227–230 (2017).

[38] J. Goodman. *Introduction to Fourier Optics*. McGraw-Hill Physical and Quantum Electronics Series. W. H. Freeman, 2005.

[39] D. Khodadad. *Phase-Derivative-Based Estimation of a Digital Reference Wave from a Single off-Axis Digital Hologram*. Applied Optics **55**, 1663–1669 (2016).

[40] R. Riesenberg and M. Kanka. *Self-Calibrating Lensless Inline-Holographic Microscopy by a Sample Holder with Reference Structures*. Optics Letters **39**, 5236–5239 (2014).

[41] L. Gong, G. Penelet and P. Picart. *Noise and Bias in Off-Axis Digital Holography for Measurements in Acoustic Waveguides*. Applied Optics **60**, A93–A103 (2021).

[42] P. Hosseini, R. Zhou, Y.-H. Kim, C. Peres, A. Diaspro, C. Kuang, Z. Yaqoob and P. T. C. So. *Pushing Phase and Amplitude Sensitivity Limits in Interferometric Microscopy*. Optics Letters **41**, 1656–1659 (2016).

[43] F. Charriére, B. Rappaz, J. Kühn, T. Colomb, P. Marquet and C. Depeursinge. *Influence of Shot Noise on Phase Measurement Accuracy in Digital Holographic Microscopy*. Optics Express **15**, 8818–8831 (2007).

[44] M. Piniard, B. Sorrente, G. Hug and P. Picart. *Modelling of the Photometric Balance for Two-Wavelength Spatially Multiplexed Digital Holography*. SPIE Optical Metrology 2021 **11783**, 1178308 (2021).

[45] D. Allan. *Statistics of Atomic Frequency Standards*. Proceedings of the IEEE **54**, 221–230 (1966).

[46] J. Biesheuvel, D. W. E. Noom, E. J. Salumbides, K. T. Sheridan, W. Ubachs and J. C. J. Koelemeij. *Widely Tunable Laser Frequency Offset Lock with 30 GHz Range and 5 THz Offset*. Optics Express **21**, 14008–14016 (2013).

[47] C. Zhou, C. He, S.-T. Yan, Y.-H. Ji, L. Zhou, J. Wang and M.-S. Zhan. *Laser Frequency Shift up to 5 GHz with a High-Efficiency 12-Pass 350-MHz Acousto-Optic Modulator*. Review of Scientific Instruments **91**, 033201 (2020).

3

4

IMPROVING DEPTH RANGE AND RESOLUTION WITH MULTI-WAVELENGTH DIGITAL HOLOGRAPHY

This chapter demonstrates multi-wavelength digital holography for large distance measurement with improved depth resolution. Wavelengths from a tunable external-cavity diode laser are calibrated from beat phases measured across a reference sample consisting of a trench of known depth. This enables wavelength calibration without external metrology. The sample distance can be recovered over a large depth range through the wavenumber-domain processing of beat phases, combining Fourier-based coarse localization with linear phase fitting. Large distance measurement is experimentally validated by measuring a mirror–sample separation of approximately 40 mm. Compared with conventional dual-wavelength schemes, the proposed method achieves 0.2 mm depth resolution over a 800 mm depth range. Error analysis shows that the height uncertainty scales as $N^{-3/2}$ *under constant wavenumber spacing, where* N *is the number of wavelength measurements.*

4

4.1. Introduction

Applications such as semiconductor manufacturing, assembly, and precision machining often involve height variations spanning several millimeters or even centimeters, while still requiring micrometer-scale depth precision [1]. Therefore, accurate optical metrology over an extended depth range is a critical, yet challenging, task in industrial inspection [2, 3]. Achieving such a large depth range with coherent optical techniques is particularly difficult, as the measurable depth is fundamentally constrained by phase ambiguity and coherence-related artifacts.

Digital holography (DH) can provide full-field quantitative phase retrieval with single-shot acquisition and, therefore, has attracted substantial interest for high-throughput metrology. However, conventional single-wavelength DH suffers from intrinsic limitations arising from 2π phase wrapping, resulting in a limited unambiguous depth range when large and steep height variation or multiple-reflection are present. Dual-wavelength digital holography (DWDH) partially alleviates the measurable depth range constraint by synthesizing a longer effective wavelength from two closely spaced illumination wavelengths, thereby extending the measurable height to the mm range [4–6]. However, the measurable range remains bounded by the synthetic wavelength Λ and practically limited by the accurate control of a very small wavelength separation. Moreover, DWDH linearly amplifies phase noise during the conversion to height and is highly sensitive to wavelength calibration errors, leading to a trade-off between depth accuracy and depth range. These issues restrict the applicability of DWDH to large depth variation metrology while losing the ability for small height sensitivity.

Multi-wavelength or frequency-scanning interferometric techniques offer an alternative approach by exploiting the spectral dependence of the interference signal to infer relative depth [7]. Techniques that are based on this are: scanning white-light interferometry [8], swept-source optical coherent tomography [9–11], and frequency-modulated continuous-wave (FMCW) [12–15]. In these techniques, axial depth is linearly related to a modulation frequency in the wavenumber domain, which allows for the spectral separation of signals originating from different axial positions. Extending this concept to digital holography, swept-source digital holography (SS-DH) has demonstrated the ability to recover depths from complex fields that are reconstructed from measured intensities with improved robustness compared to ordinary DH. Despite these advances, most existing swept-source DH implementations [16–18] face several practical barriers that prevent their wider adoption in industrial metrology. First, most reported swept-source systems [19] require lasers with highly linear wavelength tuning and high reproducibility, which are often expensive and require a k-clock to acquire data linear in k. This hardware requirement increases system cost and limits robustness in long-term operation. Second, dense and continuous wavelength/frequency sampling is usually required in their application, generally involving hundreds or thousands of spectral measurements. Such large data volumes require increased acquisition time and have high computational complexity, which are incompatible with real-time industrial inspection. Finally, prior swept-source DH studies are typically designed under a trade-off between depth range and depth resolution, which is imposed

by the finite tuning range and sampling rate. As a result, the potential of swept-source holography for centimeter-scale, high-precision 3D metrology remains largely unexplored.

Here, we present a multi-wavelength digital holography framework specifically designed for long depth range measurement under practical hardware constraints. Rather than relying on continuous and linear wavelength sweeps, the proposed approach employs discrete wavelength sampling with only a limited number of tuning steps. A self-referenced wavelength calibration strategy is introduced to recover the effective synthetic wavenumbers directly from the measured beat phase, eliminating the need for external wavelength-monitoring devices. By formulating the depth estimation in the spectral domain and interpolating onto a uniform wavenumber grid, the method enables Fourier-domain ranging over centimeter-scale depths while maintaining high depth precision. The proposed framework is experimentally validated by accurately measuring the separation between two reflective objects separated by approximately 40 mm in height, exceeding the unambiguous depth range of conventional DWDH while using only a small set of discrete wavelength samples. The results highlight the potential of multi-wavelength DH as a practical, high-accuracy, and hardware-efficient solution for industrial 3D metrology, particularly in scenarios demanding large depth range, high resolution, and robustness to coherent mixing.

4.2. THEORY

4.2.1. MULTI-WAVELENGTH DIGITAL HOLOGRAPHY

Multi-wavelength digital holography (MWDH) extends conventional digital holography by recording a sequence of holograms with different wavelengths. In MWDH, the depths of the object are retrieved by analysis of the interferometric spectral data. To establish the underlying principle, we first consider a single interface sample illuminated by a plane wave at perpendicular incidence with wavelength λ. The reflected field from the surface can be expressed as

$$O(\lambda) = r\,A\,\exp\left(i\frac{2\pi}{\lambda}2z_d\right), \tag{4.1}$$

where A is the incident amplitude, r is the reflection coefficient of the sample. The term z_d denotes the optical depth of the object surface measured from the reference plane (defined at $z = 0$), and the factor of 2 arises from the round-trip propagation path. To implement an off-axis configuration with the field retrieved from a single measurement, the reference beam R is chosen as a tilted plane wave, with the off-axis angle denoted as θ. The interference pattern, also called the hologram, is

$$I(\lambda) = |O(\lambda) + R(\lambda)|^2 = |O(\lambda)|^2 + |R(\lambda)|^2 + O(\lambda)R(\lambda)^* + O(\lambda)^*R(\lambda)\,. \tag{4.2}$$

Due to the oblique reference wave, after Fourier transform of the hologram, the terms OR^* and O^*R appear as translated versions of the Fourier transform of the object O. Using Fourier filtering, the object field $O(\lambda)$ is extracted by isolating one

for the cross-terms in the frequency domain and subsequently applying an inverse Fourier transform:

$$O(\lambda) = \mathcal{F}^{-1}\Big\{\mathcal{F}\{I(\lambda)\} \cdot W(f_x, f_y)\Big\} \cdot R_{dig}(\lambda)\,, \tag{4.3}$$

where $\mathcal{F}$ and $\mathcal{F}^{-1}$ denote the forward and inverse Fourier transform, $W(f_x, f_y)$ is a band-pass filter window that selects the spectral region containing the spatial spectrum of OR^*, and $R_{dig}(\lambda)$ is a digitally generated reference field used to compensate for the oblique phase of the reference beam.

In multi-wavelength digital holography, the laser wavelength is tuned sequentially, and a hologram is captured at each wavelength. After reconstruction using Eq. (4.3), one obtains a set of object fields $[O(\lambda_1), O(\lambda_2), \dots, O(\lambda_N)]$. It is more convenient to express the field in terms of the wavenumber $k = 2\pi/\lambda$:

4

$$O(k) = r\,A\,\exp\left(ikz_d\right). \tag{4.4}$$

Let the swept wavenumber range be $k \in [k_1, k_N]$, sampled uniformly with increment Δk. The discrete sampling grid is then

$$k_n = k_1 + n\Delta k\,, \quad n = 0, 1, \dots, N-1\,. \tag{4.5}$$

This uniformly sampled representation forms the basis for subsequent Fourier-domain processing and enables depth-resolved reconstruction via a discrete Fourier transform.

Applying a discrete inverse Fourier transform (IDFT) to the sampled field $O(k_n)$ yields the depth response:

$$\hat{O}(z_m) = \mathrm{IDFT}\Big\{O(k_n)\Big\} = \sum_{n=0}^{N-1} O(k_n)\exp\left(ik_n z_m\right), \tag{4.6}$$

where z_m represents the discrete depth coordinate, corresponding to the mapping of the wavenumber axis, given by

$$z_m = \left(m - \frac{N}{2}\right)\frac{2\pi}{N\Delta k}, \qquad m = 0, 1, \dots, N-1\,. \tag{4.7}$$

The depth sampling interval Δz and maximum unambiguous total depth range z_{total} follow immediately:

$$\Delta z = \frac{2\pi}{N\Delta k}\,, \quad z_{\text{total}} = \frac{2\pi}{\Delta k}\,. \tag{4.8}$$

Eqs. (4.6) to (4.8) show that amplitude and phase variations with respect to k are mapped to spatial localization along z, and peaks in $|\hat{O}(z_m)|$ correspond to physical reflectors whose OPD lies within the depth range $[0, z_{\text{max}}]$.

Looking at Eq. (4.4) and assuming that the object consists of a single reflecting interface with a k_n−independent amplitude A and reflection coefficient r, the object field and its spatial-domain representation are given by

$$O(k_n) = rA\exp\left(ik_n z_d\right) \quad \Rightarrow \quad \hat{O}(z_m) \propto rA \cdot \mathrm{sinc}\left(\frac{N\Delta k}{2}(z_m - z_d)\right), \tag{4.9}$$

which exhibits a peak centered at $z_m = z_d$. Thus, the multi-wavelength procedure provides a direct transformation from the measured $k-$domain field to a depth-resolved structural profile of the object.

4.2.2. MULTI-WAVELENGTH DH DEPTH RESOLUTION ENHANCEMENT

Conventional dual-wavelength digital holography (DWDH) improves the unambiguous depth range by exploiting the beat phase $\Phi = \phi_1 - \phi_2$, where ϕ_1 and ϕ_2 are the phases retrieved from two distinct lasers operating at wavelength λ_1 and λ_2. The corresponding synthetic wavelength $\Lambda = \frac{\lambda_1 \lambda_2}{|\Delta\lambda|}$ defines the extended depth range, where $\Delta\lambda$ is the wavelength separation between the two wavelengths. For a single reflecting surface object, the surface height h is then quantified as

$$h = \frac{1}{2}\frac{\Phi}{2\pi}\Lambda \quad \text{or} \quad h = \frac{1}{2}\frac{\Phi}{\Delta k}, \tag{4.10}$$

4

where $\Delta k = 2\pi \left| \frac{1}{\lambda_1} - \frac{1}{\lambda_2} \right|$ is the difference in wavenumber between the two sources.

In DWDH, the phase retrieved from digital holography is influenced by shot noise, speckle decorrelation, and environmental disturbances. Under proper operating conditions, shot-noise-limited detection can be achieved, in which the phase accuracy σ_ϕ is mainly governed by the full well capacity of the sensor [4, 20]. A detailed derivation of the relationship between shot noise and σ_ϕ is provided in Chapter 2. Besides, because ϕ_1 and ϕ_2 are independent, the measured beat phase Φ would have a standard deviation of $\sigma_\Phi = \sqrt{2}\sigma_\phi$. Assuming the wavelength is perfectly determined and stable, applying error propagation to Eq. (4.10) yields the height precision

$$\sigma_h = \frac{\sigma_\Phi}{2\Delta k} = \frac{\sqrt{2}\sigma_\phi}{2\Delta k}. \tag{4.11}$$

This reveals a concerning limitation: small wavenumber differences Δk amplify uncertainty in h, as $\sigma_h \propto 1/\Delta k$. Yet, small Δk is exactly what is required to generate a long synthetic wavelength. Hence, in DWDH large depth range measurements are more noise-sensitive.

As an example, consider a reflective step with height $h = 1\,\text{mm}$ measured using $\lambda_1 = 633\,\text{nm}$ as one of the DWDH light sources. The second light source has a wavelength difference of $\Delta\lambda = 1\,\text{pm}$, resulting in a synthetic wavelength of $\Lambda = 400\,\text{mm}$. Assuming optimal shot-noise-limited phase accuracy of $\sigma_\phi \approx 0.02$ rad – a value experimentally determined in the preceding chapter and adopted here [21] – substituting these values into Eq. (4.11) gives a height uncertainty of $\sigma_h = 0.902\,\text{mm}$, i.e., the measurement error is almost equal to the true height. The DWDH depth estimation process is plotted in Figure 4.1(a), where the height error is visualized as the uncertainty in the gradient of a linear fit of the phase ϕ with respect to wavenumber k. The shaded area represents the confidence interval associated with the 1σ uncertainty band of the fitted gradient. Since the height corresponds to half of the gradient of a line connecting the phase values at the two wavenumbers, large amounts of phase noise yields a large uncertainty in the gradient estimate, producing unreliable height values.

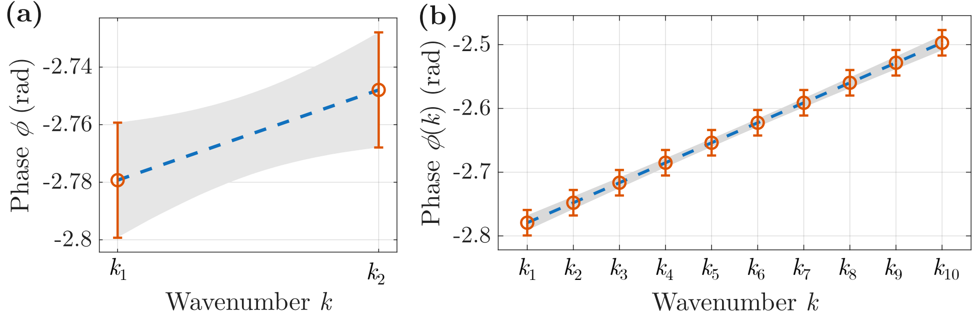

Figure 4.1: Height estimation and error analysis for DWDH and MWDH. Height h is estimated from half of the phase-wavenumber ($\phi - k$) gradient. (a) Two-point linear fitting, characteristic of DWDH, where the shaded region indicates the confidence interval. Note that phase noise σ_ϕ reduces the reliability of the gradient estimate as the wavenumber interval Δk decreases. (b) Multi-point fitting in MWDH. Maintaining the same sampling interval Δk while utilizing more sampling points over an extended k−range provides a more accurate gradient estimation.

Multi-Wavelength DH overcomes this limitation by retrieving phase measurements at a set of discrete wavenumbers $[k_1, k_2, \dots, k_N]$. Since the measured phase of a single-interface reflector satisfies $\phi(k) = 2kh$, the height h can be estimated from the gradient of a linear regression of ϕ versus k. Compared with the two-point estimation used in DWDH, fitting over multiple wavenumbers exploits redundancy in the data and yields a lower estimator variance for the slope. Assuming independent, identically distributed phase noise with variance σ_ϕ^2, ordinary least-squares regression gives the variance of the fitted gradient $\hat{s}$ as

$$\sigma_{\hat{s}}^2 = \frac{\sigma_\phi^2}{\sum_{n=1}^{N}(k_n - \bar{k})^2}, \tag{4.12}$$

where $\bar{k}$ denotes the mean wavenumber. This expression shows that the estimation accuracy is governed by the second central moment of the sampled wavenumbers, rather than solely by the total tuning range.

When the wavenumbers are uniformly spaced with a constant sampling interval Δk, as defined in Eq. (4.5), the summation in the denominator can be calculated analytically as $\sum_{n=1}^{N}(k_n - \bar{k})^2 = \Delta k^2 N(N^2 - 1)/12$. Using the relation $h = \hat{s}/2$, the resulting height precision becomes

$$\sigma_h = \frac{1}{2}\sqrt{\frac{\sigma_\phi^2}{\sum_{n=1}^{N}(k_n - \bar{k})^2}} = \frac{\sigma_\phi}{\Delta k}\sqrt{\frac{3}{N(N^2 - 1)}}. \tag{4.13}$$

Note that under this assumption, increasing the number of sampled wavenumbers N simultaneously enlarges the total tuning range $N\Delta k$. Consequently, the

improvement in σ_h with increasing N should be understood as arising from both the increase in the number of points of the regression and the associated increase in the range of wavenumbers. Eq. (4.13) highlights a scaling behavior $\sigma_h \propto N^{-3/2}$ for large N, indicating a rapid improvement in height precision as more wavelengths are incorporated. The expression naturally reduces to the two-point DWDH case when $N = 2$. As illustrated in Figure 4.1(b), including more wavenumber samples produces a clearer linear dependence of $\phi(k)$, thereby averaging out the influence of individual phase errors. As an example, using $N = 10$ and the previously mentioned single wavelength phase uncertainty, Eq. (4.13) predicts a height uncertainty $\sigma_h \approx 70.21\,\mu\text{m}$, representing more than an order-of-magnitude improvement over the two-point DWDH precision of 0.902 mm.

4.3. Results

4.3.1. Experimental Setup

The experiments were conducted using a lensless off-axis digital holography setup based on a Mach-Zehnder interferometer, operating in reflection mode, similar to the setup described in Chapter 3 and illustrated in Figure 4.2. A tunable external-cavity diode laser (ECDL) with a center wavelength around 633 nm was the illumination source. The camera was a monochrome CMOS sensor with 4112×3008 pixels and a pixel pitch of 3.45 µm. Each interferogram was captured in a single-shot with an exposure time of approximately 200 µs.

Two objects were positioned within the field of view: (i) a well-defined trench with a nominal depth of $d = 993.554\,\mu\text{m}$ and a specified standard deviation of 0.042 µm (Rubert & Co. Ltd, product type 515; a schematic of the trench geometry is presented in Figure 4.2(a)) and (ii) a planar mirror positioned roughly 40 mm in front of the trench. The trench served as a reference for calibrating all wavelengths, while the mirror was used for large range depth estimation. The ECDL wavelength was sequentially detuned by changing the drive current from 81 mA to 100 mA at a fixed temperature of 7 °C, resulting in 20 discrete wavelengths, each associated with one single-shot hologram.

4.3.2. Beat Phase and Synthetic Wavelength Calculation

Each interferogram was demodulated using the off-axis Fourier filtering method described in Eq. (4.3). After isolating the object field from the hologram, the angular spectrum method was applied to numerically propagate the diffracted field to the minimum-diffraction plane, corresponding to the top surface of the calibration trench. In the absence of high-precision wavelength detection instruments, the exact absolute operating wavelength λ_i at each tuning step could not be measured directly. Instead, the difference in two wavelengths can be inferred from the beat phase between the top and bottom of the trench. Let $O_i(x, y)$ denote the reconstructed complex object field at the i−th wavelength. For any two measurements $i, j \in \{1, \ldots, 20\}$, the beat-phase map is computed as

$$\Phi_{i,j}(x, y) = \arg\left(O_i(x, y)\, O_j^*(x, y)\right) . \tag{4.14}$$

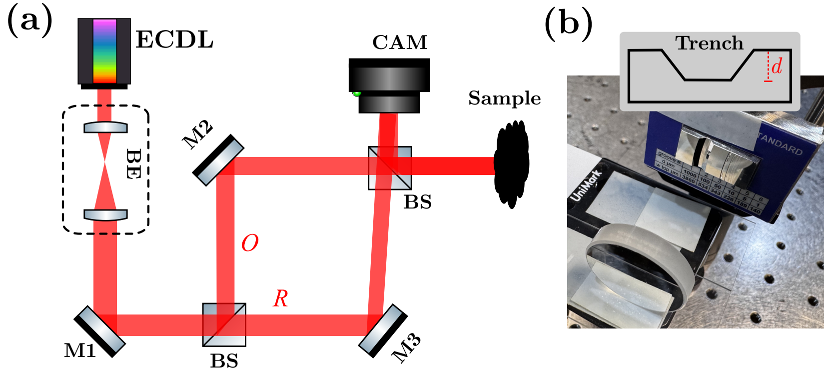

Figure 4.2: (a) Schematic diagram of the multi-wavelength digital holography setup. ECDL: external-cavity diode laser with tunable wavelength, BS: beamsplitter, BE: beam expander, CAM: camera, and M: mirror . (b) Photograph of the measured object, where a mirror is placed around 40 mm in front of the calibration target with trench.

Each pairwise combination of these 20 wavelengths yields a unique synthetic wavelength, giving rise to $\binom{20}{2} = 190$ synthetic wavelengths in total.

Figure 4.3(a) shows a representative beat-phase map $\Phi_{1,3}$ associated to the wavelength pair (λ_1, λ_3). The green area in the figure corresponds to the results of the calibration target featuring in the center a trench with a nominal depth $d = 993.554\,\mu\text{m}$. In contrast, the blue area arises from the reflection of the mirror positioned around 40 mm in front of the sample surface. Extracting the phase along the red dashed line yields the one-dimensional profile shown in Figure 4.3(b). Owing to the additional optical path length introduced by the trench, the phases within the trench region are slightly shifted relative to those of the surrounding surfaces.

Let $\Phi^d_{i,j}$ denote the beat phase associated with the trench depth d relative to the surface. This quantity is obtained by a piecewise linear fit to the one-dimensional phase profile, separating the trench region from the adjacent top surface regions. In reflection geometry, the corresponding synthetic wavelength for each pairwise combination $\Lambda_{i,j}$ is given by

$$\Lambda_{i,j} = \frac{4\pi d}{\Phi^d_{i,j}}\,. \tag{4.15}$$

where the factor of $4\pi d$ accounts for the round-trip optical path difference. Applying this relation to the example in Figure 4.3(b) where $\Phi^d_{1,3} = -0.22\,\text{rad}$ is measured and $d = 993.554\,\mu\text{m}$, it follows that the synthetic wavelength is: $\Lambda_{1,3} = 56.25\,\text{mm}$. Following the determination of the synthetic wavelengths, the individual wavelength separations $\Delta\lambda_{i,j} = |\lambda_i - \lambda_j|$ are retrieved. For this, we assume a quasi-monochromatic approximation to the synthetic wavelength numerator where $\lambda_i \approx \lambda_j \approx \lambda_c$, which is justified since the total tuning range is negligible relative to the central wavelength λ_c. Taking the first tuning step as a reference, the

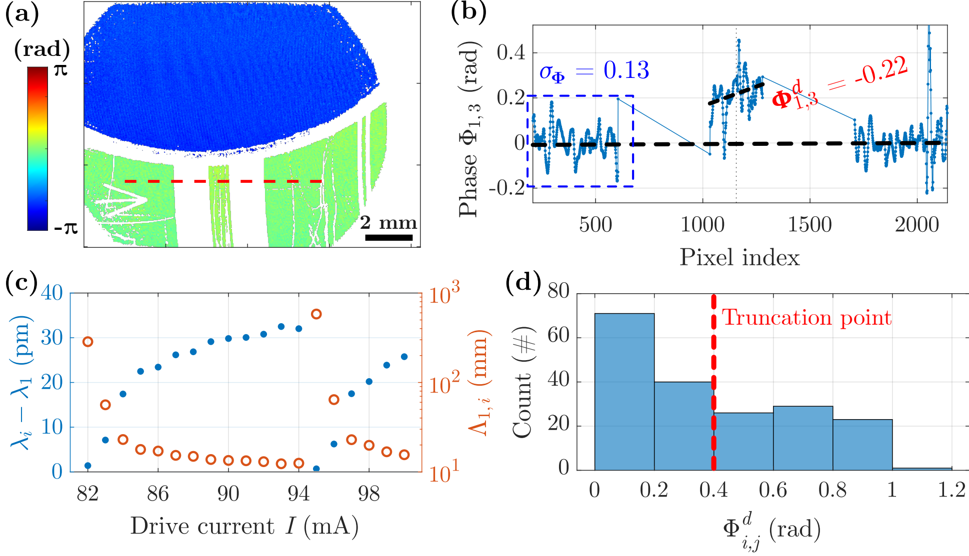

Figure 4.3: (a) Beat phase map $\Phi_{1,3}$ of the sample consisting of two objects, showing the calibration trench (bottom) and a mirror (top). The red dashed lines mark the cross-section used for 1D analysis in (b). (b) Extracted phase profiles. The trench exhibits a slightly elevated phase relative to the adjacent platform. (c) Wavelength differences $\lambda_i - \lambda_1$ and synthetic wavelengths $\Lambda_{1,i}$ as a function of laser drive current I. (d) Distribution of $\Phi^d_{i,j}$ from 190 wavelength pairs. Negative values were sign-corrected. To suppress noise-dominated estimates, all phases with $\Phi^d_{i,j} \leq 0.4\,\text{rad}$ will be discarded.

wavelength differences between λ_1 and the remaining 19 working wavelengths were calculated and are shown in Figure 4.3(c). Overall, the results indicate that an increase in the drive current leads to an increase in wavelength difference, except for jumps between 94 mA to 98 mA, consistent with the typical tuning behavior of an ECDL. The tuning curve is clearly nonlinear, and the presence of abrupt change suggests the occurrence of mode hopping during current tuning. The right hand vertical axis shows the obtained synthetic wavelengths ranging from the millimeter to meter level.

Repeating this procedure for all 190 wavelength pairs results in a statistical ensemble of beat-phase values $\Phi^d_{i,j}$, whose histogram distribution is shown in Figure 4.3(d). Negative phases were corrected to ensure a consistent sign convention throughout the analysis. However, because of the influence of noise, the phase measurements inevitably exhibit fluctuations. As larger synthetic wavelengths correspond to smaller $\Phi^d_{i,j}$, noise can dominate when $\Phi^d_{i,j}$ approaches zero. From the flat platform region in Figure 4.3(b), the beat phase standard deviation is estimated to be $\sigma_\Phi = 0.13\,\text{rad}$. Therefore, to avoid unreliable

noise-dominated quantification of $\Phi^d_{i,j}$, all synthetic wavelengths with beat phases $\Phi^d_{i,j} \leq 0.4\,\text{rad}$ were discarded from further analysis.

4.3.3. Distance estimation

With the synthetic wavelengths calibrated from the trench depth, we will now determine the distance h between the mirror and the top of the trench sample, from now on called sample. Let $\Phi^h_{i,j}$ denote the beat phase associated with the mirror-sample separation for the wavelength pair (λ_i, λ_j). Under dual-wavelength reflection geometry, $\Phi^h_{i,j}$ satisfies

$$\Phi^h_{i,j} = \frac{4\pi h}{\Lambda_{i,j}}\,, \tag{4.16}$$

4

where $\Lambda_{i,j}$ is the synthetic wavelength for a wavelength pair previously calibrated from the trench depth. Defining the synthetic wavenumber as $K_{i,j} = 2\pi/\Lambda_{i,j} = \Phi^d_{i,j}/(2d)$, then Eq. (4.16) can be rewritten as a linear phase–wavenumber relation:

$$\Phi^h_{i,j} = K_{i,j}\,2h\,. \tag{4.17}$$

Hence, in principle we could determine h by fitting $\Phi^h_{i,j}$.

First, we take the beat phase map Φ_{13} as an example. Figure 4.4(a) shows the one-dimensional phase profile along the black dashed line in the inset. The beat phase of the mirror-groove depth is again obtained by piecewise fitting and yields $\Phi^h_{1,3} = -2.32\,\text{rad}$. Applying the same procedure to all wavelength pairs and excluding data corresponding to $\Phi^d_{i,j} \leq 0.4\,\text{rad}$ results in a beat phase distribution shown in Figure 4.4(b). In principle, h could be estimated by direct linear regression of an unwrapped $\Phi^h_{i,j}$ against $K_{i,j}$. However, in practice, this approach is not feasible for several reasons. First, the phase $\Phi_{i,j}$ is strongly 2π-wrapped and cannot be reliably unwrapped as shown in Figure 4.4(a). Second, the sampling of $K_{i,j}$ is non-uniform because the ECDL exhibits a nonlinear tuning characteristic with respect to the drive current. Third, the synthetic wavenumber $K_{i,j}$ inherits noise from the trench beat phase $\Phi^d_{i,j}$. The beat phase noise is amplified for wavelength pairs with small beat phases, i.e., the case of large $\Lambda_{i,j}$ or small $K_{i,j}$. These combined factors collectively prevent a straightforward least-squares regression.

To obtain a stable estimate of h, $\Phi^h_{i,j}$ are instead interpreted as a complex sequence in the wavenumber domain. Each beat phase is first converted to its complex representation $S_{i,j} = \exp(i\,\Phi^h_{i,j})$, and the corresponding $K_{i,j}$ values are sorted and interpolated onto a uniformly spaced wavenumber K grid. This interpolation is performed on the complex phasors rather than directly on the wrapped phase, ensuring continuity and avoiding interpolation across phase discontinuities. After resampling, the signal takes the form $S(K) \approx \exp(i\,2hK)$, where the physical distance h represents a linear phase coefficient with respect to the wavenumber K.

A discrete Fourier transform (DFT) of $S(K)$ produces a depth-dependent spectrum, and the band-limited linear phase term maps to a shifted sinc function

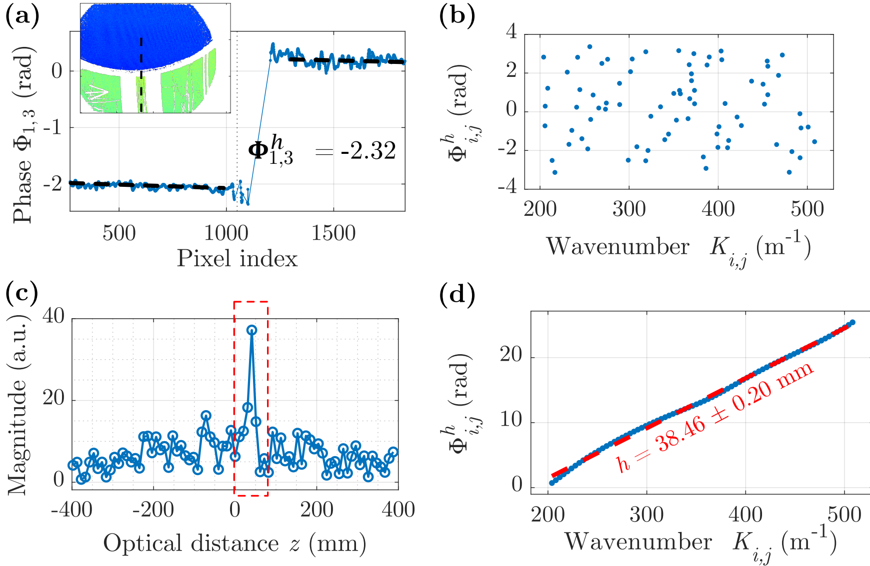

Figure 4.4: (a) Beat phase profile along the dashed line in the inset, from which the mirror–sample phase $\Phi^h_{13} = -2.32$ rad is determined by piecewise fitting. (b) Retrieved beat phase $\Phi^h_{i,j}$ (wrapped), from which direct linear regression is impractical because of the 2π-wrapping and non-uniform wavenumber sampling. (c) Coarse depth estimate obtained by resampling the complex phasors $S_{i,j} = \exp(i\,\Phi^h_{i,j})$ onto a uniform wavenumber grid K and applying a DFT. The dominant spectral peak appears around $z \approx 40$ mm. (d) Refined estimate of the mirror–sample depth by applying a band-pass window around the DFT peak in (b), followed by inverse DFT, phase unwrapping, and linear fitting.

whose magnitude exhibits a dominant peak at $z \approx h$. This process is analogous to the mechanism of FD-OCT, where the depth position of the reflector corresponds to the frequency of the interferometric modulation in wavenumber space. The depth resolution of this coarse estimate is fundamentally limited by the available wavenumber span $K_{\text{span}} = K_{\text{max}} - K_{\text{min}}$, giving a theoretical resolution in our case of approximately $\Delta z \approx 10$ mm. The coarse depth estimate obtained from the DFT is shown in Figure 4.4(c), where a clear peak appears around $z \approx 40$ mm. A refined estimate can be obtained by applying a band-pass window around the DFT peak, suppressing noise and side lobes, followed by an inverse DFT to recover a filtered complex signal with reduced noise whose phase varies linearly with K. This phase is then unwrapped and fitted to the linear model of Eq. (4.17) using a least-squares regression. The fitting result is shown in Figure 4.4(d), where the mirror–sample depth h is defined as half the slope fit value. The estimated value of h is 38.46 mm, with an associated uncertainty of $\sigma_h = 0.20$ mm, which is calculated from the regression covariance matrix.

Using Eq. (4.13), the theoretical height precision corresponding to the data in Figure 4.4(b) is calculated. Assuming a constant beat phase precision of $\sigma_\Phi = 0.13\,\text{rad}$ across all measurements, the resulting height precision is $\sigma'_h = 0.08\,\text{mm}$. However, the precision obtained from the fitting method is lower than this theoretical value. This discrepancy could be attributed to the simplified assumption of uniform phase noise. This may not hold in practice as the performance of the laser may vary depending on the drive current settings, leading to increased phase errors. In addition, phase noise affects not only the beat phase but also the synthetic wavenumber $K_{i,j}$ calibration, introducing further uncertainty that the current model does not account for. Despite these limitations, the proposed multi-wavelength approach demonstrates a clear improvement in precision over conventional dual-wavelength schemes. To clearly demonstrate this, Figure 4.5 shows the result for the wavelength pair $(\lambda_7, \lambda_{11})$. The dual wavelength beat phase measured across the trench is $\Phi^d_{7,11} = 0.12\,\text{rad}$, corresponding to a synthetic wavelength of $\Lambda_{7,11} = 103.4\,\text{mm}$. The mirror-sample beat phase is measured as $\Phi^h_{7,11} = 4.82\,\text{rad}$, yielding a height estimate of $h = 39.67\,\text{mm}$. Due to the linear amplification of phase noise by large synthetic wavelengths, the resulting height uncertainty is $\sigma_h = 1.51\,\text{mm}$. We contrast this to our 20 wavelength estimate of 38.46 ± 0.20 mm, which is almost a factor 10 better.

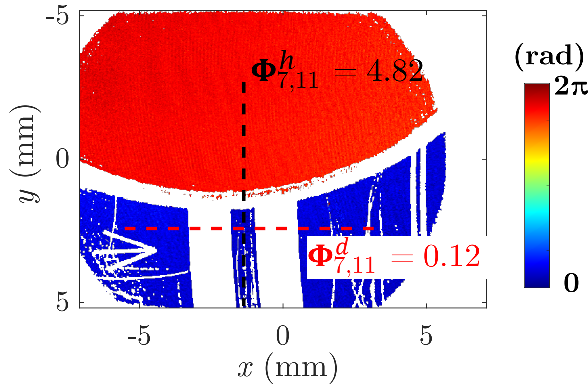

Figure 4.5: Beat phase map for the single wavelength pair $(\lambda_7, \lambda_{11})$: with trench phase $\Phi^d_{7,11}$ and mirror-sample phase $\Phi^h_{7,11}$ indicated. These phase values correspond to $\Lambda_{7,11} = 103.4\,\text{mm}$, and $h = 39.67 \pm 1.51$ mm.

4.4. Discussion

The results presented in this work demonstrate that multi-wavelength DH can overcome several practical limitations of conventional dual-wavelength DH. The proposed method relies on pairwise beat-phase measurements from multiple discrete wavelength tunings on a known reference depth to calibrate the corresponding synthetic wavelengths. The proposed methods avoids the need for high-precision wavelength measurement and/or high repeatability of the

laser detuning. Experiments demonstrate the ability to construct a dense set of wavenumbers from only 20 single-shot holograms.

A practical constraint is the nonuniform sampling of the synthetic wavenumber arising from the nonlinear tuning characteristics of the ECDL. As shown in the experimental results, direct linear regression of the mirror beat phases is unreliable under such sampling. By treating the beat phases as the exponential of complex phasors and interpolating onto a uniform K-grid, the measurements can be treated within a Fourier-domain ranging framework. The coarse DFT peak and subsequent phase-based refinement jointly yield accurate long-range distance estimates, with improved depth resolution.

The simulation and analysis of fitting error highlights the advantage of multi-wavelength method in improving fitting accuracy. It shows that the error in height estimation h exhibits an approximate $N^{-3/2}$ scaling when the wavenumber step Δk is held constant. In contrast, if the total tuning range $N\Delta k$ is fixed, which is often the case with a limited laser tuning bandwidth, then increasing N reduces Δk and the improvement becomes proportional to $N^{-1/2}$. Besides, thanks to the off-axis DH field retrieval, the reconstructed depth spectrum is full range instead of the usual half range from real-valued intensity measurements. This property enables the unambiguous depth range to be extended to twice that of the conventional OCT. These results indicate that multi-wavelength DH provides a flexible framework for full-field depth imaging over an extended range.

4.5. CONCLUSION

We introduce a multi-wavelength digital holography approach with potential 800 mm depth range. The obtained depth resolution of 0.2 mm for our experimental settings is almost 10 times better than obtained with dual wavelength digital holography. Our method does not require precise wavelength monitoring nor uniform wavenumber sampling. By exploiting pairwise beat phases from 20 wavelength measurements, 190 synthetic wavenumbers were generated and calibrated using a reference target. Combined with interpolation to uniform k, Fourier-domain ranging, and Fourier filtering and fitting, this framework delivers a few centimeter-scale depth range and high depth resolution using single-shot and full-field holograms at each tuning step. The demonstrated performance suggests strong potential for applications in optical metrology, multilayer inspection, and long-range structural characterization. Future work may focus on increasing the usable k-bandwidth, improving phase stability between wavelength steps, and applying the method to multi-interface samples.

REFERENCES

[1] K. Wu, C.-C. Lee, N. J. Brock and B. Kimbrough. *Multilayer Thin-Film Inspection through Measurements of Reflection Coefficients*. Optics Letters **36**, 3269–3271 (2011).

[2] H. Quan, W. Shi and L. Kong. *Non-Destructive Optical Measurement of Transparent Objects: A Review*. Light: Advanced Manufacturing **6**, 333–357 (2025).

[3] T. Liu, Y. Hong, J. Wu, W. Zhu and B. Ju. *A New Method for Measuring Multilayer Thickness Using a Chromatic Confocal Sensor*. Nanomanufacturing and Metrology **7**, 22 (2024).

[4] H. Shangguan, H. P. Urbach and J. Kalkman. *Lensless Single-Shot Dual-Wavelength Digital Holography for Industrial Metrology*. Applied Optics **63**, 4427–4434 (2024).

[5] T. Colomb, S. Krivec, H. Hutter, A. A. Akatay, N. Pavillon, F. Montfort, E. Cuche, J. Kühn, C. Depeursinge and Y. Emery. *Digital Holographic Reflectometry*. Optics Express **18**, 3719–3731 (2010).

[6] D. Carl, M. Fratz, M. Pfeifer, D. M. Giel and H. Höfler. *Multiwavelength Digital Holography with Autocalibration of Phase Shifts and Artificial Wavelengths*. Applied Optics **48**, H1–H8 (2009).

[7] M. V. Sarunic, S. Weinberg and J. A. Izatt. *Full-Field Swept-Source Phase Microscopy*. Optics Letters **31**, 1462–1464 (2006).

[8] L. Yuan, T. Guo, D. Tang, H. Liu and X. Guo. *Simultaneous Film Thickness and Refractive Index Measurement Using a Constrained Fitting Method in a White Light Spectral Interferometer*. Optics Express **30**, 349–363 (2022).

[9] J. de Wit, K. Angelopoulos, J. Kalkman and G.-O. Glentis. *Fast and Accurate Spectral-Estimation Axial Super-Resolution Optical Coherence Tomography*. Optics Express **29**, 39946–39966 (2021).

[10] M. Siddiqui, A. S. Nam, S. Tozburun, N. Lippok, C. Blatter and B. J. Vakoc. *High-Speed Optical Coherence Tomography by Circular Interferometric Ranging*. Nature Photonics **12**, 111–116 (2018).

[11] J. Xu, Y. Shi, S. Song and R. K. Wang. *High-Resolution Long-Range Swept-Source OCT for Volumetric Imaging and Metrology up to 200 m*. Optica **12**, 1144–1152 (2025).

[12] J. Zheng. *Optical Frequency-Modulated Continuous-Wave (FMCW) Interferometry*. Springer Series in Optical Sciences. Springer, 2005.

[13] M. Okano and C. Chong. *Swept Source Lidar: Simultaneous FMCW Ranging and Nonmechanical Beam Steering with a Wideband Swept Source*. Optics Express **28**, 23898–23915 (2020).

[14] H. Zhang, Q. Xie, Q. Na, N. Zhang, L. Wang, L. Qin, J. Song and L. Wang. *Optical Parametric-Assist Frequency Modulation for FMCW Lidar Enabling Double-Range Velocity Measurement*. Optics and Lasers in Engineering **178**, 108203 (2024).

[15] L. Zhang, M. Gagino, A. Millan-Mejia, K. A. Williams and V. Dolores Calzadilla. *Directly Modulated FMCW Tunable Laser with Highly Linear Frequency Chirp and Narrow Linewidth*. APL Photonics **9**, 106101 (2024).

[16] V. Lédl, P. Psota, F. Kaván, O. Matoušek and P. Mokrý. *Surface Topography Measurement by Frequency Sweeping Digital Holography*. Applied Optics **56**, 7808–7814 (2017).

[17] D. Hillmann, H. Spahr, H. Sudkamp, C. Hain, L. Hinkel, G. Franke and G. Hüttmann. *Off-Axis Reference Beam for Full-Field Swept-Source OCT and Holoscopy*. Optics Express **25**, 27770–27784 (2017).

[18] R. Guo, Z. Liao, J. Li, A. Li, P. Song and R. Zhu. *Optical Homogeneity Measurement of Parallel Plates by Wavelength-Tuning Interferometry Using Nonuniform Fast Fourier Transform*. Optics Express **27**, 13072–13082 (2019).

[19] Y. Kim, N. Sugita and M. Mitsuishi. *Measurement of Highly Reflective Surface Shape Using Wavelength Tuning Fizeau Interferometer and Polynomial Window Function*. Precision Engineering **45**, 187–194 (2016).

[20] S. Chen, C. Li, C. Ma, T.-C. Poon and Y. Zhu. *Phase Sensitivity of Off-Axis Digital Holography*. Optics Letters **43**, 4993–4996 (2018).

[21] H. Shangguan, H. P. Urbach and J. Kalkman. *Lensless Single-Shot Dual-Wavelength Digital Holography with Sub-Pixel Resolution and Centimeter Depth Range*. APL Photonics **10** (2025).

5

CONCLUSIONS AND OUTLOOK

This chapter concludes the thesis and provides perspectives for future research. First, the main contributions of this thesis to digital holography (DH) for industrial inspection are summarized, with emphasis on the challenges addressed in measurement throughput, depth range, spatial resolution, and depth precision. Subsequently, an outlook is provided on future directions for further development, including the extension to depth-resolved tomographic imaging of multilayer structures, noise mechanism studies in speckle-dominated samples, and strategies for further enhancing depth precision beyond the limits demonstrated in this thesis.

5.1. CONCLUSIONS

In this thesis DH is investigated as a full-field, three-dimensional, high-throughput optical metrology technique for industrial inspection. The primary focus has been on extending the depth range, improving spatial resolution, and enhancing depth precision while maintaining the intrinsic advantages of DH, such as full-field and quantitative phase imaging capability. These objectives are motivated by the increasingly stringent requirements of advanced semiconductor manufacturing and related applications, where micrometer-scale accuracy must be achieved over centimeter-scale depths and lateral dimensions under high throughput constraints. Three key challenges, inherent to DH-based metrology, were addressed. The first is the limited unambiguous depth range of single-wavelength DH caused by phase wrapping. The second is the lateral resolution constraint imposed by the finite sensor pixel size, which is particularly severe in lensless and compact DH system configurations. The third is the trade-off between depth range and depth precision in dual-wavelength DH, where phase noise is amplified by the synthetic wavelength.

In Chapter 2 the applicability of DH to high-speed three-dimensional industrial inspection scenarios of samples with large and abrupt height variations was demonstrated. A dual-wavelength DH scheme was employed to extend the unambiguous depth range from half a wavelength to half the synthetic wavelength. By combining off-axis DH with spatial-frequency multiplexing, single-shot measurement at two wavelengths was achieved without sacrificing acquisition speed.

A theoretical analysis of phase precision was derived under shot-noise-limited detection and was experimentally validated. Measurements on calibrated height targets and representative industrial samples confirmed reliable reconstruction over an extended depth range, demonstrating the suitability of lensless single-shot dual-wavelength DH for full-field and 3D industrial metrology.

Chapter 3 focused on overcoming pixel-size-limited lateral resolution in lensless DH. An expanding wavefront illumination scheme was introduced to increase the captured angular spectrum of the object field. In parallel, an aberration compensation algorithm was developed to estimate and correct global background aberrations from locally sampled regions. This combined approach enabled an improvement in lateral resolution in a lensless DH configuration while retaining single-shot measurement capability. In addition, the use of a tunable external-cavity diode laser extended the accessible measurement depth range to the centimeter scale, thereby allowing macroscopic depth measurements to be combined with microscopic spatial resolution.

Chapter 4 addressed the depth-precision limitation of conventional dual-wavelength DH, in which height uncertainty increases linearly with the synthetic wavelength as the unambiguous depth range is extended. To mitigate this trade-off, a multi-wavelength DH approach based on discrete wavelength sampling was introduced, enabling depth estimation through multi-point phase fitting in the wavenumber domain. By combining Fourier-based coarse depth localization filtering with linear phase regression, long-range measurement was achieved with improved depth resolution. A self-calibration strategy based on pairwise beat-phase analysis of a known calibration sample eliminated the need for additional wavelength metrology. The results demonstrate that multi-wavelength DH provides an effective means of decoupling depth range from depth precision, which is critical for applications involving large height variations.

In summary, this thesis demonstrates that several fundamental limitations of DH can be mitigated through a combination of optical system design and advanced reconstruction algorithms. The proposed methods extend the depth range and improve both lateral resolution and depth precision, while preserving the intrinsic advantages of DH, including full-field imaging, quantitative phase retrieval, and computational flexibility. However, these advances introduce new practical challenges. Multi-wavelength acquisition increases data volume and computational complexity, and high-resolution configurations impose stricter requirements on system stability and calibration accuracy. These factors may limit direct deployment in fully in-line, high-throughput manufacturing environments. Nevertheless, as a complementary technique to established inspection tools, DH offers unique capabilities for non-destructive, depth-resolved, and high-precision characterization of complex industrial structures. Building on the results presented in this thesis, the following section discusses future research directions.

5.2. TOWARDS DIGITAL HOLOGRAPHIC TOMOGRAPHY

5.2.1. MODELING THE FIELD FROM MULTILAYERED OBJECTS

When an optical field interacts with a multilayer object, the reflected field arises from the coherent superposition of partial waves generated at each interface. As an example of a simple multilayer object, consider a stack of planar homogeneous layers with refractive indices $n_0, n_1, \dots, n_N$ and interface positions at $z = z_1, \dots, z_N$. Medium 0 is the ambient medium (e.g. air), and medium N denotes the substrate. Figure 5.1(a) illustrates an example of a two-layer stack with three interfaces ($N = 3$). When an incident field E_{inc} interacts with a multilayer structure, the total reflected field in the ambient medium is the result of the coherent superposition of partial waves generated at each interface. As the field propagates through the stack, successive reflection and transmission events occur at every refractive index discontinuity. The resulting upward-propagating components combine to form the measured field in medium 0, with the amplitude and phase of each contribution governed by the Fresnel coefficients, as well as by the thicknesses and refractive indices of the individual layers. Consequently, the total reflected field is highly sensitive to variations in wavelength, incidence angle, layer thickness, and the refractive indices of the constituent layers.

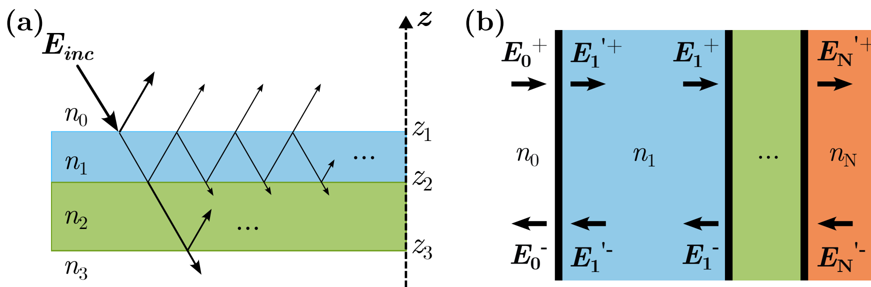

Figure 5.1: (a) Illustration of multiple internal reflections and transmissions generated at each interface when light with amplitude E_{inc} is incident on a multilayered structure (ray refraction is omitted for visual clarity). (b) Transfer-matrix method representation of the fields in the multilayer system, where $(\cdot)^+$ and $(\cdot)^-$ denote the forward- and backward-propagating field components, respectively, while E_j' and E_j denote the fields at the left and right of the medium n_j.

To quantify the field from the multiple-reflection process, we employ the transfer-matrix method (TMM) [1–3]. For simplicity, we use normal incidence and s-polarization for the following derivation, and assume that the field is incident from air ($n_0 = 1.0$). Then the field reaching the first interface can be expressed as $E_{inc} = A_0 \exp(ik_0 z_1)$, where A_0 is the incidence complex amplitude, $k_0 = 2\pi/\lambda_0$ is the wavenumber in air. The TMM divides the field in the medium into two components, the forward/ transmitted component E^+ and the backward/ reflected component E^- as illustrated in Figure 5.1(b). The fields at the left- and right-hand

side of an interface $j\,(1 \leq j \leq N)$ are related by the interface matrix $D_{j-1,j}$:

$$\begin{pmatrix} E_{j-1}^{+} \\ E_{j-1}^{-} \end{pmatrix} = D_{j-1,j} \begin{pmatrix} E_{j}^{\prime +} \\ E_{j}^{\prime -} \end{pmatrix}, \qquad D_{j-1,j} = \frac{1}{t_{j-1,j}} \begin{pmatrix} 1 & r_{j-1,j} \\ r_{j-1,j} & 1 \end{pmatrix}. \tag{5.1}$$

where $r_{j-1,j}$ and $t_{j-1,j}$ are the reflection and transmission coefficients determined by the Fresnel equations:

$$\begin{cases} r_{j-1,j} = \dfrac{n_{j-1} - n_j}{n_{j-1} + n_j}, \\ t_{j-1,j} = \dfrac{2n_{j-1}}{n_{j-1} + n_j}. \end{cases} \tag{5.2}$$

Then, the fields at the left and right of the medium j are associated with the phase-delay matrix P_j:

$$\begin{pmatrix} E_{j}^{\prime +} \\ E_{j}^{\prime -} \end{pmatrix} = P_j \begin{pmatrix} E_{j}^{+} \\ E_{j}^{-} \end{pmatrix}, \qquad P_j = \begin{pmatrix} e^{-i\delta_j} & 0 \\ 0 & e^{i\delta_j} \end{pmatrix}. \tag{5.3}$$

where $\delta_j = k_j d_j$ is the phase shift due to passing through the layer, $k_j = n_j k_0$ is the wavenumber in medium j, $d_j = z_{j+1} - z_j$ is the layer thickness. By multiplying the interface and phase-delay matrices for all $N-1$ layers with N interfaces, one links the field in the incidence medium to the one in the substrate ($j = N$) as:

$$\begin{pmatrix} E_{0}^{+} \\ E_{0}^{-} \end{pmatrix} = D_{01} P_1 D_{12} P_2 \cdots P_{N-1} D_{N-1,N} \begin{pmatrix} E_{N}^{\prime +} \\ E_{N}^{\prime -} \end{pmatrix}. \tag{5.4}$$

The ultimate 2×2 matrix M describing the input and output fields of the multilayer stack are defined by

$$M = \begin{pmatrix} M_{11} & M_{12} \\ M_{21} & M_{22} \end{pmatrix} = D_{01} P_1 D_{12} P_2 \cdots P_{N-1} D_{N-1,N}, \tag{5.5}$$

which is the so-called global system transfer matrix. The overall reflection coefficient of the multilayer system can be calculated as

$$r_{\text{tot}} = \frac{E_0^-}{E_0^+} = \frac{M_{21}}{M_{11}}, \tag{5.6}$$

and the reflected field seen from medium 0 is then $E_r = r_{\text{tot}} A_0 \exp{(ik_0 z_1)}$.

Taking a simple two-interface sample as an example, consider a thick glass plate of thickness d placed between media 0 and 2. The total transfer matrix is then $M = D_{01} P_1 D_{12}$, and the phase shift accumulated during a single pass through the plate is $\delta = n_1 k_0 d$. Combining the above equations yields the total reflection coefficient for the glass layer stack

$$r_{\text{tot}} = \frac{r_{01} + r_{12} e^{i2\delta}}{1 + r_{01} r_{12} e^{i2\delta}}. \tag{5.7}$$

This expression shows that the reflection coefficient is not merely the sum of the two reflections; rather, it arises from the coherent interference between the front-surface reflection (r_{01}) and the back-surface reflection ($r_{12}e^{i2\delta}$). The reflection coefficient r_{tot} is a highly sensitive function of wavelength λ, thickness d, and refractive index n, since a small change in any of these parameters will alter the phase delay δ, which in turn changes the modulus of r_{tot} (i.e., the reflection amplitude).

The transfer-matrix method provides a concise and straightforward framework for calculating the reflected field from multi-interface objects. Furthermore, it can be easily extended to more complicated cases, such as when absorption is present. In such instances, the refractive index is defined as a complex quantity, $n_j = n'_j + i\kappa_j$, where the real and imaginary parts indicates the wavefield phase shift and amplitude attenuation, respectively.

5.2.2. HOLOGRAPHIC IMAGING OF MULTILAYER OBJECT

In addition to long-range depth measurement, multi-wavelength digital holography can also enable the three-dimensional reconstruction of multi-interface objects. To demonstrate this capability, we simulate the structure shown in Figure 5.2(a), consisting of three interfaces in air: a slightly tilted and distorted surface located near $z = 8$ mm, a planar interface at 38 mm, and a third interface at 150 mm containing a 6 mm-deep recess at its center. The working wavelength is tuned from 633.05 nm to 632.95 nm and uniformly sampled in terms of wavenumber k over 128 steps.

Each off-axis digital hologram is demodulated using the Fourier filtering method, producing a sequence of complex object fields that are then stacked to form a discretized representation $O(x, y; k)$. Because the wavenumber samples are uniformly spaced, a Fourier transform can be applied directly along k (Eq. (4.6)), producing a 3D reconstruction $\hat{O}(x, y; z)$. This operation is formally equivalent to the depth-ranging process in Fourier domain OCT (FD-OCT), where depth is encoded as the spatial frequency of the interference modulation in k–domain.

The calculated depth response, shown in Figure 5.2(b), reveals the reconstructed cross-section along $y = 0$, analogous to a B-scan in OCT terminology. The center column of this B-scan corresponds to the axial depth profile at $x = 0$, i.e., an A-scan, and is plotted as the red curve in Figure 5.2(c). Three distinct peaks are observed, corresponding to the three interfaces and appearing at the expected relative separations. Unlike conventional FD-OCT, the reconstructed spectrum in multi-wavelength DH is one-sided rather than symmetric because off-axis holography retrieves complex-valued fields, thereby eliminating the Hermitian conjugate term that produces the symmetric spectrum in OCT. This property allows the reconstructed depth signal to shift within the available depth range by either moving the position of the reference arm or multiplying the k-space field $O(x, y; k)$ by a reference phase factor $\exp(i\,kz_0)$ during data processing. The result shown in Figure 5.2(b) corresponds to a shift of $z_0 = -50$ mm. The reconstructed interfaces accurately reproduce the tilt, surface perturbation, and recess, demonstrating that in principle multi-wavelength DH can recover multi-interface structures over extended depth ranges while maintaining lateral

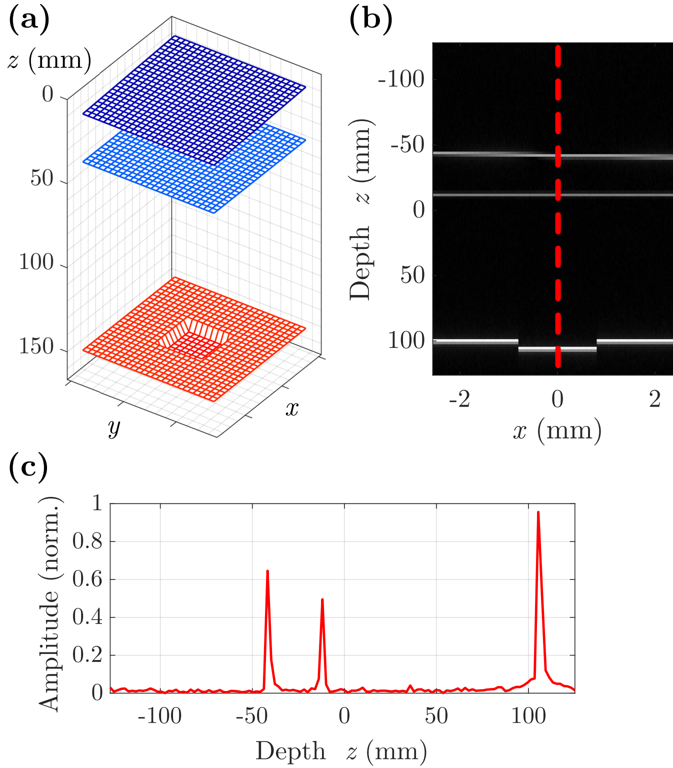

Figure 5.2: 3D reconstruction of a simulated three-interface object using multi-wavelength digital holography. (a) Geometry of the three interfaces. (b) Reconstructed B-scan along $y = 0$ after applying a depth shift of -50 mm. (c) Depth profiles (A-scans) extracted from the center column of (b)(indicated by the red dashed line).

field information.

The multi-wavelength depth-resolution enhancement strategy developed in Chapter 4 can be directly applied here, achieving high-resolution holographic volumetric reconstruction over a large depth range. Despite this potential, several challenges remain for practical multi-wavelength DH tomography. Accurate depth ranging relies on precise knowledge and stability of the light source during wavelength tuning; specifically, both wavelength accuracy and spectral amplitude variations are critical because the reconstruction depends on coherent processing of the complex fields across k. In addition, dispersion and refractive-index variations across layered structures, as well as volumetric and multiple scattering, are not considered in the present simulations and may distort the reconstructed depth response. Addressing these issues is essential for extending multi-wavelength DH tomography toward the quantitative and robust imaging of complex industrial samples.

5.3. MEASURING SPECKLE-DOMINANT OBJECTS

The investigations in the previous chapters focused mainly on optically smooth or weakly scattering objects, for which the complex object fields remain highly correlated between different wavelengths and lateral positions. Under such conditions, phase precision is predominantly limited by acquisition noise, and performance can approach the shot-noise limit. In contrast, many industrial components exhibit optically rough surfaces. Under coherent illumination, height variations within a single resolution cell give rise to different scattering contributions, such that the detected complex field is a random phasor sum forming a fully developed speckle pattern [4, 5]. When the illumination wavelength is changed, the underlying scattering geometry is preserved, but the phase accumulated by each contribution changes proportionally to the wavelength. This modifies the relative phases of the contributing phasors and leads to a reduction in the complex coherence between the speckle fields at the two wavelengths. Consequently, the phase difference contains a random component, commonly referred to as speckle decorrelation noise, which poses challenges to phase-based measurement techniques for rough industrial surfaces.

5.3.1. SPECKLE DECORRELATION NOISE

In general, speckle decorrelation noise arises whenever two complex fields used to compute a phase difference are not perfectly correlated. This decorrelation may be caused by the temporal evolution of the object, changes in illumination or observation geometry, or wavelength variation, etc [4]. Such decorrelation leads to a random phase term, denoted by ϵ, added to the measured phase difference. The statistics of ϵ are governed by the complex coherence factor μ, which quantifies the degree of similarity between the two speckle fields [4, 6, 7]. Specifically, $|\mu|$ measures how strongly the complex amplitudes at corresponding points remain correlated, with $|\mu| = 1$ indicating perfect correlation, and $|\mu| = 0$ corresponding to fully uncorrelated speckle patterns. As $|\mu|$ decreases, the probability density function of the decorrelation noise broadens from a narrow distribution around zero to a uniform distribution over $(-\pi, \pi)$, with a corresponding increase in phase noise variance.

A specific case encountered in multi-wavelength digital holography is wavelength-induced speckle decorrelation. For a rough surface with a root-mean-square (RMS) height variation S_q, the modulus of the complex coherence factor between two speckle fields recorded at wavelengths λ_1 and λ_2 is approximated by [6]

$$|\mu| = \exp\left(-\frac{8\pi^2 S_q^2}{\Lambda^2}\right), \tag{5.8}$$

where $\Lambda = \lambda_1\lambda_2/|\lambda_1 - \lambda_2|$ is the synthetic wavelength. The probability density function (PDF) of the speckle decorrelation noise ϵ depends on the modulus of the complex coherence factor $|\mu|$ and can be expressed as [8]

$$p(\epsilon) \approx \frac{1-|\mu|^2}{2\pi}(1-\beta^2)^{-\frac{3}{2}}\left(\beta\arcsin(\beta) + \frac{\pi\beta}{2} + \sqrt{1-\beta^2}\right). \tag{5.9}$$

where $\beta = |\mu|\cos(\epsilon)$. As $|\mu| \to 0$, the PDF becomes uniformly distributed over the range $(-\pi, \pi)$ with a constant height of $1/2\pi$. Conversely, as $|\mu| \to 1$, the distribution approaches a delta function of ϵ, indicating that the two fields are fully correlated and the decorrelation noise ϵ is close to 0.

The final quantity of interest is the standard deviation of the decorrelation noise, σ_ϵ. When the complex coherence factor is relatively large ($|\mu| > 0.7$), an approximate equation for σ_ϵ was provided by Picart et al. [9]

$$\sigma_\epsilon = \frac{7}{4}\left(1 - |\mu|\right)^{\frac{2}{5}} . \tag{5.10}$$

5.3.2. TOTAL PHASE NOISE AND HEIGHT PRECISION

For single-shot dual-wavelength digital holography, the instantaneous phase precision is generally governed by decorrelation-induced phase noise σ_ϵ and acquisition-related noise $\sigma_{\phi,\mathrm{acq}}$. The total beat phase variance can, to a first order approximation, be expressed as

$$\sigma_\Phi^2 \approx \sigma_{\phi,\mathrm{acq}}^2 + \sigma_\epsilon^2 . \tag{5.11}$$

Acquisition noise $\sigma_{\phi,\mathrm{acq}}$ has been analyzed in detail in previous chapters, where it was shown to be associated with the hologram recording and reconstruction process and depends on parameters such as fringe visibility, detector saturation level, bandpass filter size, full-well capacity, and bit depth, and is ultimately bounded by shot noise. In contrast, σ_ϵ originates from speckle decorrelation and is governed by the surface roughness and synthetic wavelength, independent of camera performance.

The surface height is related to the beat phase through $h = (\Phi/4\pi)\,\Lambda$, to distinguish the individual contribution of speckle noise to the total height precision σ_h, we define the height precision induced purely by speckle decorrelation as

$$\sigma_{h,\epsilon} = \frac{\Lambda}{4\pi}\sigma_\epsilon . \tag{5.12}$$

Although increasing the synthetic wavelength Λ improves the complex coherence factor $|\mu|$ and thus reduces σ_ϵ, see Eqs. (5.8) and (5.10), the mapping from phase to height amplifies the residual phase noise by the factor $\Lambda/4\pi$. Substituting the analytical expression for σ_ϵ yields

$$\begin{aligned} \sigma_{h,\epsilon} &= \frac{\Lambda}{4\pi}\frac{7}{4}\left(1 - \exp\left(-\frac{8\pi^2 S_q^2}{\Lambda^2}\right)\right)^{\frac{2}{5}} \\ &\approx \frac{7}{16\pi}\Lambda^{\frac{1}{5}}\left(8\pi^2\right)^{\frac{2}{5}} S_q^{\frac{4}{5}} . \end{aligned} \tag{5.13}$$

This equation shows that, despite the reduced decorrelation noise in the phase domain, the corresponding height precision $\sigma_{h,\epsilon}$ increases with Λ due to the linear mapping from phase to height. This behavior is clearly illustrated in Figure 5.3,

where it can be seen that $\sigma_{h,\epsilon}$ increases monotonically with Λ for different surface roughness values S_q, confirming that the benefit of reduced speckle decorrelation is outweighed by the linear scaling of height precision with Λ. At the same time, increasing S_q leads to an upward shift of the curves, highlighting the strong sensitivity of height precision to surface roughness.

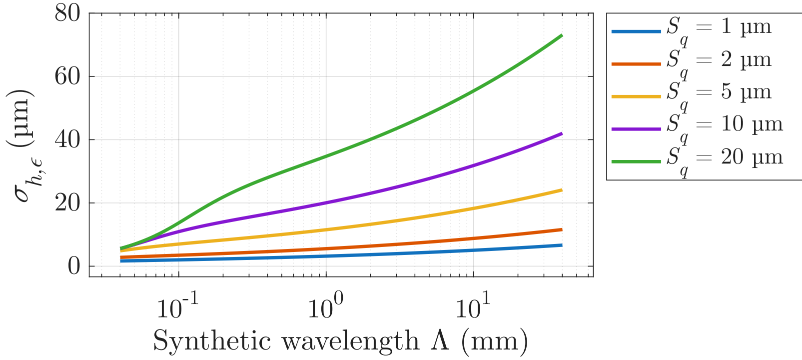

Figure 5.3: Effect of object roughness S_q and synthetic wavelength Λ on height quantification precision $\sigma_{h,\epsilon}$

In practice, the total height precision σ_h is determined by the combined phase noise σ_Φ. Mapping σ_Φ to height gives

$$\sigma_h = \frac{\Lambda}{4\pi}\sigma_\Phi \,. \tag{5.14}$$

The blue line in Figure 5.4 shows σ_h as a function of the synthetic wavelength Λ when both $\sigma_{\phi,\mathrm{acq}}$ and σ_ϵ are included for a surface roughness of $S_q = 10\,\mu\mathrm{m}$. For small Λ, the total noise closely matches the curve that only considers speckle decorrelation noise (purple line), indicating that speckle decorrelation is the dominant noise source in this regime. As Λ increases, the two curves gradually diverge, reflecting the increasing contribution of acquisition noise amplified by the synthetic wavelength.

The discussion above leads to the conclusion that, for rough surfaces, both speckle decorrelation noise and acquisition noise play a key role in determining height precision. Most existing studies characterize roughness using a single global parameter, whereas in practical measurements, surface roughness is often spatially varying and anisotropic, leading to locally varying scattering behavior within the speckle field. Extending the existing noise models to incorporate spatially varying or wavelength-dependent surface statistics would, therefore, provide a more realistic description of phase noise in practical scenarios. Recent studies [6, 8, 10, 11] further indicate that the speckle decorrelation and acquisition noise are intrinsically coupled, as decorrelation alters the local speckle intensity, which in turn modifies intensity-dependent detection noise, such as shot noise. A unified framework that explicitly accounts for this interplay would enable a more complete understanding

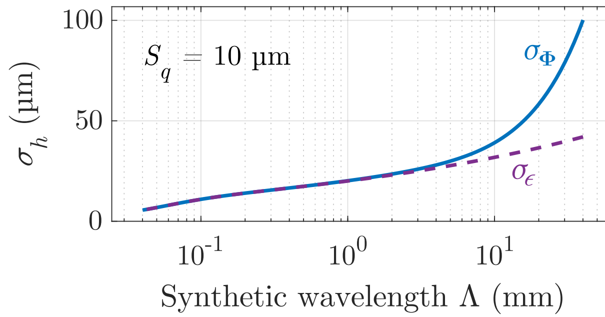

Figure 5.4: Height precision σ_h as a function of synthetic wavelength Λ considering combined phase noise. For small Λ, speckle decorrelation noise is shown as dominant; however, for larger Λ, the linear scaling of acquisition noise with Λ becomes the dominant factor.

5

of phase uncertainty on rough surfaces. Beyond single-interface measurements, additional challenges arise in multilayer or tomographic configurations, where multiple partially correlated scattering interfaces contribute to the measured field. Developing noise models for such situations is an important direction for future research.

5.4. MULTI-STEP PHASE UNWRAPPING DEPTH PRECISION ENHANCEMENT

In the previous chapters, it has been shown that multi-wavelength digital holography can substantially extend the unambiguous measurement range. However, this synthetic-wavelength mechanism simultaneously amplifies phase noise when phase is converted into height. By fitting phase measurements acquired at multiple wavenumbers, we demonstrated improved height precision, provided that phase noise between different wavelengths is independent and identically distributed. Nevertheless, this method places high demands on the wavenumber spacing and sampling density in k−domain, especially for the case of imaging large depth ranges. Acquiring additional wavelengths not only increases measurement time but also increases the computational load; both factors are particularly critical in industrial inspection. Many practical imaging targets, such as semiconductor wafers with multiple levels, precision-machined metal parts, or additively manufactured components, exhibit a combination of large height variations with fine surface details. Existing solutions often address these requirements separately, using low-coherence profilometry for the millimeter-scale range and interferometric techniques for sub-micrometer resolution, at the cost of system complexity and reduced throughput.

An emerging and effective strategy to overcome this limitation is hierarchical multi-step phase unwrapping [12–15], in which phase results associated with

different synthetic wavelengths are assigned distinct roles in a coarse-to-fine reconstruction process rather than being treated uniformly. In this framework, the largest synthetic wavelength is first used to obtain a globally unambiguous but relatively noisy estimate of the height map. This coarse estimate is then used to resolve the integer ambiguity of the height within the measurement range of the next synthetic wavelength. Subsequently, phase results retrieved from progressively shorter synthetic wavelengths are incorporated to refine the height estimate, yielding improved depth precision while preserving the large unambiguous range.

In the proposed hierarchical scheme, a sequence of synthetic wavelengths with progressively decreasing values $\{\Lambda_1, \Lambda_2, \dots, \Lambda_k\}$ is constructed as

$$\Lambda_k = \alpha^{k-1}\Lambda_1 \,, \tag{5.15}$$

where $k \geq 1$, $0 < \alpha < 1$ is a stepping factor, and Λ_1 is the largest synthetic wavelength. At each hierarchy level k, a wrapped height estimate $h_k^{(w)}$ is obtained from the corresponding beat phase. The absolute height is then recovered by determining the integer order m_k that minimizes the discrepancy with the previous coarser estimate h_{k-1}:

$$h_k = m_k \frac{\Lambda_k}{2} + h_k^{(w)} \,, \quad m_k = \mathrm{round}\left(\frac{h_{k-1} - h_k^{(w)}}{\Lambda_k/2}\right) \,, \tag{5.16}$$

This recursive procedure propagates the large unambiguous range of the longest synthetic wavelength while successively refining the height precision through progressively shorter synthetic wavelengths. Assuming additive phase noise with a standard deviation σ_ϕ, the height precision associated with Λ_1 is given by $\sigma_{h_1} = (\sqrt{2}\sigma_\phi/4\pi)\Lambda_1$. Consequently, at hierarchy level k, the corresponding height precision becomes

$$\sigma_{h_k} = \frac{\sqrt{2}\sigma_\phi}{4\pi}\Lambda_k = \frac{\sqrt{2}\sigma_\phi}{4\pi}\alpha^{k-1}\Lambda_1 \,, \tag{5.17}$$

indicating that the height precision decreases exponentially with the hierarchy level k. As a result, the final estimate of height achieves substantially reduced height noise without sacrificing measurement range, decoupling depth range and precision to enable enabling micrometer-scale surface precision over a centimeter-scale depth range.

To illustrate this method, Figure 5.5 shows a simulation of a stepped height sample using hierarchical phase unwrapping. In this example, $\Lambda_1 = 40.1\,\mathrm{mm}$, the stepping factor $\alpha = 0.5$, and the phase noise $\sigma_\phi = 0.06\,\mathrm{rad}$. The test object consists of three height steps, represented by the black dashed curve. The height reconstruction obtained using only Λ_1 (blue curve) corresponds to conventional dual-wavelength DH (DWDH) and shows pronounced fluctuations due to amplified phase noise, with a measured height precision of $\sigma_{h_1} = 0.289\,\mathrm{mm}$. In contrast, the result of the five-step hierarchical unwrapping (red curve) shows a substantial improvement in height precision and closely matches the ground truth, achieving a precision of $\sigma_{h_5} = 0.018\,\mathrm{mm}$. These results are consistent with the theoretical expectations and verify the feasibility of the proposed hierarchical approach.

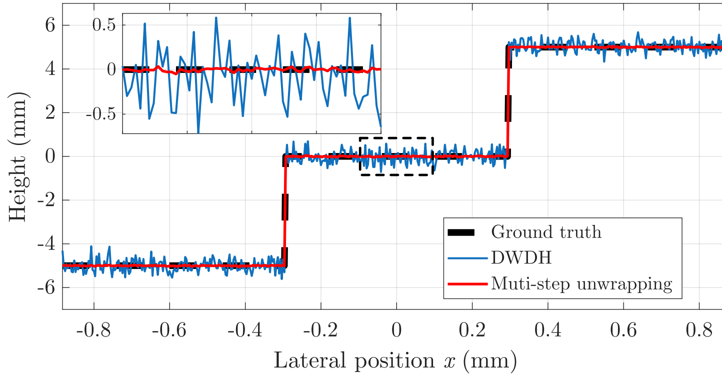

Figure 5.5: Simulation of five-step hierarchical phase unwrapping. The black dashed line denotes the ground-truth stepped height sample, the blue line shows the coarse height reconstruction obtained with only Λ_1, and the red line represents the result using the hierarchical method, demonstrating improved height precision without loss of depth range. The inset shows a zoom-in of the dashed box for better comparison.

5

The hierarchical multi-step phase unwrapping discussed here is different from the multi-wavelength fitting framework developed in Chapter 4. The fitting approach in multi-wavelength DH exhibits greater tolerance to imperfect knowledge of the working wavelengths; because height estimation is formulated as a regression problem in wavenumber space, in which wavelength uncertainty, non-uniform sampling, and slow spectral drift can be incorporated statistically through the fitting process. As a result, this framework is better suited to swept-source or current-tuned laser systems where precise and repeatable wavelength control is difficult to achieve.

Hierarchical phase unwrapping relies on the deterministic construction of synthetic wavelengths and on the accurate control of wavelength tuning. Because each step requires the previous coarser estimate to identify the correct integer cycle, any deviation in the wavelength will introduce cumulative error in the calculations. If this error causes the estimated height to shift by more than $\Lambda_k/4$, it results in an incorrect integer assignment m_k, leading to catastrophic $'2\pi'$ jumps in the reconstruction. Consequently, such methods are most effective in regimes where synthetic wavelengths can be engineered and stabilized with high fidelity, allowing ambiguity resolution to be treated as a deterministic rather than a statistical problem. This distinction clarifies that multi-wavelength fitting and hierarchical unwrapping are not competing strategies, but rather complementary tools suited to different operating conditions. It further suggests that future long-range digital holographic metrology systems may benefit from hybrid schemes in which deterministic hierarchical unwrapping is applied where wavelength control is reliable, while multi-wavelength fitting is employed to refine precision and maintain robustness under wavelength uncertainty.

REFERENCES

[1] M. C. Troparevsky, A. S. Sabau, A. R. Lupini and Z. Zhang. *Transfer-Matrix Formalism for the Calculation of Optical Response in Multilayer Systems: From Coherent to Incoherent Interference*. Optics Express **18**, 24715–24721 (2010).

[2] C. C. Katsidis and D. I. Siapkas. *General Transfer-Matrix Method for Optical Multilayer Systems with Coherent, Partially Coherent, and Incoherent Interference*. Applied Optics **41**, 3978–3987 (2002).

[3] B. Harbecke. *Coherent and Incoherent Reflection and Transmission of Multilayer Structures*. Applied Physics B **39**, 165–170 (1986).

[4] J. W. Goodman. *Speckle Phenomena in Optics: Theory and Applications*. Roberts and Company Publishers, 2007.

[5] V. Bianco, P. Memmolo, M. Leo, S. Montresor, C. Distante, M. Paturzo, P. Picart, B. Javidi and P. Ferraro. *Strategies for Reducing Speckle Noise in Digital Holography*. Light: Science & Applications **7**, 48 (2018).

[6] M. Piniard, B. Sorrente, G. Hug and P. Picart. *Theoretical Analysis of Surface-Shape-Induced Decorrelation Noise in Multi-Wavelength Digital Holography*. Optics Express **29**, 14720–14735 (2021).

[7] S. Montresor and P. Picart. *Quantitative Appraisal for Noise Reduction in Digital Holographic Phase Imaging*. Optics Express **24**, 14322–14343 (2016).

[8] H. Zhang, B. Qian and H. Yan. *Modeling the Measurement Precision of Rough Surfaces in Multi-Wavelength Digital Holography*. Optics Express **34**, 857–878 (2026).

[9] P. Picart, S. Montresor, O. Sakharuk and L. Muravsky. *Refocus Criterion Based on Maximization of the Coherence Factor in Digital Three-Wavelength Holographic Interferometry*. Optics Letters **42**, 275–278 (2017).

[10] E. Meteyer, C. Pezerat and P. Picart. *Decorrelation and Anti-Correlation from Defocus in Digital Holographic Interferometry*. JOSA A **40**, B33–B46 (2023).

[11] P. Yan, X. Liu, Y. Wang, T. Ren, H. Jiang and J. Li. *Quantitative Model and Experimental Validation of Speckle Decorrelation in Digital Speckle Pattern Interferometry*. Optics Express **34**, 4966–4981 (2026).

[12] M. K. Kim. *Phase Microscopy and Surface Profilometry by Digital Holography*. Light: Advanced Manufacturing **3**, 481–492 (2022).

[13] Q. Liu, L. Li, X. Huang, H. Zhang and X. Yue. *Hierarchical Phase Unwrapping for Dual-Wavelength Digital Holographic Microscopy*. Journal of Optics **22**, 045701 (2020).

[14] J. Xiong, L. Zhong, S. Liu, X. Qiu, Y. Zhou, J. Tian and X. Lu. *Improved Phase Retrieval Method of Dual-Wavelength Interferometry Based on a Shorter Synthetic-Wavelength*. Optics Express **25**, 7181–7191 (2017).

[15] Y. Li, W. Xiao and F. Pan. *Multiple-Wavelength-Scanning-Based Phase Unwrapping Method for Digital Holographic Microscopy*. Applied Optics **53**, 979–987 (2014).

ACKNOWLEDGEMENTS

Looking back on the past years of my PhD, I feel very fortunate to have met so many people who, in different ways, supported, encouraged, and accompanied me along the way. Beyond the papers and research outcomes, it is the people I met and the time we shared that I will remember most. I have chosen not to list every name here, partly because accidentally leaving someone out would trouble me far more than any typo in this thesis. I hope those whose names do not appear here will forgive me and still recognize themselves somewhere in these words. As this thesis comes to an end, I would like to express my sincere gratitude to all of you.

First and foremost, I would like to thank my supervisor, **Jeroen**, for your guidance and support throughout my PhD. You encouraged me, trusted me, and gave me reassurance when I doubted myself. You gave me the freedom to explore questions that truly interested me, while always offering thoughtful advice when I needed direction. Our conversations were open, honest, and enjoyable, and you often felt less like a supervisor and more like a friend. In this environment, I gradually learned to think more independently, make my own judgments, and take more responsibility for my research. **Paul**, although we did not meet often, I found every discussion with you valuable. The questions you raised often went straight to the main limitations of my work. You pushed me to think more carefully, reconsider my ideas, and strengthen my research.

My sincere thanks also go to **Raymond** from ITEC. I would also like to acknowledge the support of ITEC and the colleagues I had the pleasure of meeting throughout this collaboration. Thank you for providing the semiconductor samples used in this work. Through our discussions, I gained a broader industrial perspective on my research and a clearer understanding of the semiconductor inspection industry. You gave me the chance to look beyond the laboratory and see how research may connect with real-world problems.

I would also like to thank all the PhD students, postdocs, and colleagues in the department. Over the years, the conversations we had in the office and around the lunch table made each working day lighter. Just as important were the activities outside work, which made my PhD life more enjoyable. Thank you all for creating such an open, welcoming, and lively environment. I am also grateful to the technical and administrative staff. Your prompt and professional help with experiments, setups, and administrative matters made day-to-day research much easier.

My thanks also go to the friends I met in Delft and elsewhere. The trips and moments we shared are among the things I value most from these years. Together, we stood on Alpine peaks and looked out over endless snow-covered mountains, walked along quiet trails in the Austrian countryside, wandered through unfamiliar cities, and spent late evenings sharing stories, jokes, worries, and plans for the

future. These moments, ordinary at the time yet impossible to recreate, became truly precious to me. They brought balance and joy to the busy PhD life. Because of you, these years away from home became much richer and more memorable.

Finally, I would like to express my deepest gratitude to my family – my dad, mom, and sister. Thank you for your understanding, trust, and support throughout all these years. You never placed too many expectations or too much pressure on me. Instead, you respected my choices and stood by me. I am deeply grateful for your love and everything you have given me.

As I come to the end of my PhD, I realize that these years have given me far more than knowledge and research experience. I have also gained lasting friendships, a broader perspective, and become more confident about what lies ahead.

To everyone who has been part of this journey: thank you.

"Let us first of all and before all be kind, then honest, and then let us never forget one another."

— Alyosha Karamazov, *The Brothers Karamazov*

CURRICULUM VITæ

Huangcheng Shangguan

01-09-1996	Born in Quanzhou, China.

EDUCATION

2014–2018 Bachelor of Science in Microelectronics Science and Engineering
Shenzhen University, China

2018–2021 Master of Science in Optical and Electronic Engineering
Shenzhen University, China
Thesis: Research on the Sorting and Wavefront Reconstruction Technology for Optical Vortex
Supervisor: Prof. dr. S. Xu

2021–2025 Ph.D. in Applied Physics
Delft University of Technology
Thesis: High-Resolution Large-Depth-Range Digital holography for 3D Optical Metrology
Promotors: Dr. J. Kalkman and Em. prof. dr. H. P. Urbach

LIST OF PUBLICATIONS

2. **H. Shangguan**, H. P. Urbach and J. Kalkman. *Lensless Single-Shot Dual-Wavelength Digital Holography with Sub-Pixel Resolution and Centimeter Depth Range.* APL Photonics **10** (2025).

1. **H. Shangguan**, H. P. Urbach and J. Kalkman. *Lensless Single-Shot Dual-Wavelength Digital Holography for Industrial Metrology.* Applied Optics **63**, 4427-4434 (2024).